MECHANICS OF MACHINING ZIRCONIUM-BASED BULK METALLIC GLASS

by

Naresh Kumar Maroju

B.Tech., Kakatiya University, 2013

M.Tech., National Institute of Technology Warangal, 2015

A THESIS SUBMITTED IN PARTIAL FULFILLMENT OF

THE REQUIREMENTS FOR THE DEGREE OF

Doctor of Philosophy

in

THE FACULTY OF GRADUATE AND POSTDOCTORAL STUDIES

(Mechanical Engineering)

THE UNIVERSITY OF BRITISH COLUMBIA

(Vancouver)

June 2021

The following individuals certify that they have read, and recommend to the Faculty of Graduate and Postdoctoral Studies for acceptance, the dissertation entitled:

MECHANICS OF MACHINING ZIRCONIUM-BASED BULK METALLIC GLASS

submitted by **Naresh Kumar Maroju** in partial fulfillment of the requirements for the degree of

Doctor of Philosophy in **Mechanical Engineering**

Examining Committee:

Dr. Xiaoliang Jin, Mechanical Engineering, UBC
Supervisor

Dr. Yusuf Altintas, Mechanical Engineering, UBC
Supervisory Committee Member

Dr. A. Srikantha Phani, Mechanical Engineering, UBC
University Examiner

Dr. Reza Vaziri, Civil Engineering, UBC
University Examiner

Additional Supervisory Committee Members:

Dr. Warren Poole, Materials Engineering, UBC
Supervisory Committee Member

Dr. Mattia Bacca, Mechanical Engineering, UBC
Supervisory Committee Member

Abstract

Bulk Metallic Glasses (BMGs) are amorphous metal alloys with applications in biomedicine, electronics, sports equipment, and aerospace. In the machining of BMGs, inhomogeneous deformation and shear localization occur, which are influenced by the temperature and free volume in the deformation zone. Understanding the mechanics of machining BMGs is essential to improve the machining efficiency and surface quality.

In this thesis, a physics-based model of chip formation is developed for orthogonal cutting of Zirconium (Zr) - based BMG considering the process kinematics, material constitutive law, heat, and free volume evolution. The model predicts the segmented chip formation, oscillations of stress and temperature in the primary shear zone. The simulation results of chip segmentation are validated from experimental measurements of chip morphology. The model explains the material deformation mechanism in orthogonal cutting of Zr-BMG associated with the amorphous structure of the workpiece material.

Vibration-assisted machining has been used to improve the machining efficiency for high-strength metal alloys. This thesis presents a new mechanistic model of elliptical vibration-assisted machining (EVAM), which determines the shear angle with respect to the ratio between the original cutting speed and the amplitude of the horizontal vibration speed. The effects of intermittent tool-workpiece contact, speed ratio, and friction reversal on the chip formation mechanism in EVAM are investigated. A 2-D vibration assistance stage is developed to perform the experimental study of the EVAM process. The chip morphology in EVAM experiments of Zr-BMG is measured to validate the predicted chip formation from the mechanistic model.

In the milling process of Zr-BMG, light emission can occur, and result in oxidation and crystallization of the machined surface. The orthogonal cutting mechanics model is extended to oblique cutting, and the predicted temperature is used to determine the amorphous-crystalline transition of Zr-BMG. The predictions are validated by X-ray diffraction examinations on the machined surface. Furthermore, experimental studies are performed to investigate the effect of milling-induced stress on surface microstructure property. The proposed model and the experimental study are used to understand the chip formation mechanism, microstructure evolution, and surface quality in the milling of Zr-BMG.

Lay Summary

Bulk metallic glasses (BMGs) are metal alloys with unique microstructures which show improvement in certain mechanical properties compared to titanium and steel alloys. Machining of BMGs can result in rapid tool wear and poor surface quality due to their high strength. Understanding the physics behind the mechanism in machining BMGs is necessary to improve the production performance.

This thesis presents a comprehensive study on understanding the material deformation behaviour in machining of Zr-BMG, including modelling and experimental investigations. The key parameters including the stress and temperature in the machining processes are predicted with experimental validations. A 2-D vibration stage is developed to determine the effect of process parameters on the material deformation in vibration-assisted machining of Zr-BMG. The results can be used to select the proper machining parameters to improve the process performance.

Preface

This Ph.D. thesis proposes a physics-based model to predict the chip formation in the machining of Zr-Bulk Metallic Glass. The thesis is a combination of published papers and manuscripts under preparation for publication in peer-reviewed journals. The Ph.D. candidate carried out the research work in these publications under the supervision of Dr. Xiaoliang Jin. The relative contributions of authors in the publications are explained in this section.

The content of Chapter 3 is published in [Maroju, N. K.], Jin, X., 2019, Mechanism of chip segmentation in orthogonal cutting of Zr-based bulk metallic glass, ASME Journal of Manufacturing Science and Engineering, Vol. 14, No. 8, 081003. The candidate formulated the proposed thermomechanical model of chip segmentation. Orthogonal experiments were conducted to validate the model. The candidate wrote the first draft of the paper. Jin, X. is the corresponding author of the manuscript and is involved in concept development, research supervision, and paper editing.

The content of Chapter 4 consists of shear angle prediction in elliptical vibration-assisted machining, and the effect of vibration assistance on chip segmentation in elliptical vibration-assisted machining of Zr-BMG. The candidate contributes to the concept formulation and modelling. This work is under the supervision of Dr. Jin.

The content of Chapter 5 consists of two parts, 1) Development of 2-D vibration stage, and 2) Experimental validation and analysis of the mechanics model developed in Chapter 4. The candidate developed the vibration stage and conducted experiments to validate the mechanics model. Some experimental studies of vibration-assisted machining of BMG are published in [Maroju, N. K.], & Jin, X., 2018, Vibration-assisted dimple generation on the bulk metallic glass. Procedia Manufacturing, 26, 317–328. The work on the development of the 2-D vibration stage is published in Wan, S., [Maroju, N. K.], Jin, X., 2019, Development of a 2-D Vibration Stage for Vibration-Assisted Micro Milling, Instrumentation Journal, Vol. 6, No. (1), 98-108. Wan was involved in drafting the manuscript and developing the amplifier of the vibration stage. The candidate performed structural design and analyses of the vibration stage, dynamics testing of the vibration stage, and manuscript drafting. Jin, X. is the corresponding author of the manuscript and was involved in research supervision and paper editing.

A partial content of Chapter 6 is published in [Maroju, N. K.], Yan, D. P., Xie, B., Jin, X., 2018, Investigations on surface microstructure in high-speed milling of Zr-based bulk metallic glass. Journal of Manufacturing Processes. Vol. 35, pp. 40-50. The candidate contributed to the concept formulation, experiments, analyses on the crystallization phenomenon in milling, and paper drafting. Yan performed SEM examinations on the machined surface. Xie was involved in conducting the experiments. Jin X. is the corresponding author and was involved in concept development, research supervision, and paper editing.

Table of Contents

List of Tables

List of Figures

List of Abbreviations

BMG	Bulk metallic glass
CSM	Cooperative shear model
EDS	Energy-dispersive X-ray spectroscopy
EVAM	Elliptical vibration-assisted machining
FEM	Finite element model
HSR	Horizontal speed ratio
PCD	Poly crystalline diamond
PDF	Pair distribution function
PSZ	Primary shear zone
SCD	Single crystal diamond
SEM	Scanning electron microscopy
STZ	Shear transformation zone
VAM	Vibration-assisted machining
XRD	X-ray diffraction

Nomenclature

A_x	Amplitude of vibration in cutting direction
A_y	Amplitude of vibration in feed direction
b	Width of cut
C_s	Correction factor
D	Dilation parameter
D_f	Thermal diffusivity
E	Young's modulus
F_i	Inertial force
F_c	Cutting Force
F_t	Thrust Force
F_s	Shear Force
F_n	Normal Force
f	Frequency of applied vibration
f_s	Segmentation spacing
G	Shear modulus
h_{un}	Uncut chip thickness
Δh	The shear plane thickness
h_a	Average thickness of the segmented chip
h_1	Maximum thickness of the segmented chip
h_2	Minimum thickness of the segmented chip
h_c	Thickness of continuous chip
K_b	Boltzmann constant
k_d	Thermal diffusivity
k	Slope of normal stress to strain
L_c	Tool chip contact length
L_p	Average Pitch length
m	Ratio of shear plane thickness to uncut chip thickness
m_s	Strain rate sensitivity
n	Ratio of tool chip contact length to uncut chip thickness
S	Stiffness parameter

T	Temperature
T_0	Initial room temperature
T_r	Reference temperature
$\hat{T}$	Dimensionless temperature
T_g	Glass transition temperature
T_x	Crystallization temperature
t	Time
$\hat{t}$	Dimensionless time
V_c	Cutting velocity
v_F	Free volume outside
v_{Fo}	Free volume inside the shear band
v_s	Average shear velocity in the deformation zone
v_n	Normal velocity of material to shear plane
v_L	Localized shear velocity
W	Barrier energy required to activate STZ
Ω_s	Volume of STZs
α	Rake angle to the cutting tool
β_v	Instantaneous friction angle
γ_o	Critical shear strain to activate STZ
γ_c	Critical yield strain of Zr-BMG
$\dot{\gamma}_s$	Applied strain rate
$\dot{\gamma}_p$	Material flow strain rate
γ_v	Pre-exponential factor
$\widehat{\dot{\gamma}_p}$	Dimensionless material shear strain rate
$\dot{\gamma}_{sv}$	Applied strain rate in vibration-assisted machining (VAM)
$\widehat{\dot{\gamma}_{sv}}$	Dimensionless shear strain rate in EVAM
ζ	Free volume
μ	Coefficient of friction
ξ	Flow coefficient of free volume
$\hat{\xi}$	Dimensionless diffusion flow coefficient of free volume
ξ_{cr}	Critical flow coefficient of free volume

$\widehat{\xi_v}$	Dimensionless diffusion flow coefficient of free volume in VAM
τ_a	Average applied stress
$\hat{\tau}$	Dimensionless shear stress
τ_c	Critical shear resistance of Zr-BMG
τ_s	Shear stress
υ	Poisson’s ratio
φ	Phase difference
ϕ_a	Average shear angle of segmented chip
ϕ_{HSR}	Shear angle in elliptical vibration- assisted machining
χ	Flow coefficient of temperature
$\hat{\chi}$	Dimensionless diffusion flow coefficient of Temperature
$\widehat{\chi_v}$	Dimensionless diffusion flow coefficient of Temperature in VAM

Acknowledgments

I am grateful to Dr. Xiaoliang Jin, my research supervisor, for his persistent guidance and continuous support throughout this research work. Working with Dr. Jin has provided me exceptional insights into machining science. Above all else, he is a good mentor and always helped me during my research work. I am thankful for his patience and kindness towards me during difficult times in my research. I am thankful to Dr. Yusuf Altintas, and I am privileged to have his support in my research. Above all, he was always welcoming and kind to me.

I express my gratitude to my parents, Maroju Somaiah & Shilaja, brother Dr. M. Suresh, and sister M. Roja for their support, everlasting love, and encouragement. They were always there to help me during my research. I am indebted and thankful to my wife M. Nikitha, for her love, support, and motivation throughout my graduate studies. Her continuous efforts and patience were quite helpful in completing my thesis.

I want to thank the Manufacturing Automation Laboratory (MAL) and the outstanding research team for their support in completing my research experiments. I would like to thank my colleagues and research group of Advanced Manufacturing Processes Laboratory (AMP) for their insights and recommendations. I am thankful to the Natural Science and Engineering Research Council (NSERC) to sponsor this research.

I would like to thank my colleagues and research group at Oklahoma State University (2015-2017) and National Science Foundation (NSF) for sponsoring the research.

I want to thank Dr. L. Chen, Dr. P. Guy, Dr. P. Clarkson and VGH for their care and support.

Finally, I thank all my friends in Vancouver for pleasant and enjoyable memories during my Ph.D. study.

Dedication

Dedicated to:

My parents Maroju Somaiah and Shilaja;

My wife Nikitha

Chapter 1

Introduction

Most of the metallic materials are in crystalline form, of which the atoms are periodically arranged in a crystalline structure. On the other hand, metallic glasses are a unique series of metal alloys with an amorphous microstructure. Metallic glasses are produced by various methods without passing through the crystallization phase of the material [1]. Earlier experiments of developing metallic glasses started with coating a thin layer of metal alloys on cold substrates, limiting the thickness of metallic glass material to sub-micrometres [2]. The first metallic glass compound was synthesized through rapid solidification at a cooling rate of 10^6 K/s [3]. The primary constitutive elements of most metallic glasses include transition elements such as Zr, Ti, Fe, Co, Ni, La, alkaline elements Ca, Mg, and noble metals Cu, Au, Pd and Pt [1, 2]. Production of bulk metallic glass (BMG) alloys with thicknesses in the order of millimetres became available in the 1990s, with pioneering work from Inoue and Suryanarayana et al. [1], Miller et al. [2], Johnson et al. [3], etc. In 1992, Johnson and Peker produced BMG at the cooling rate of 1 K/s [4] with Zr as the primary constitutive element, known as model Vit-1.

BMGs show improvement in mechanical properties such as higher elastic limit, yield strength, hardness, and corrosion resistance compared to their crystalline counterparts. These improvements are attributed to their amorphous microstructure, which possesses much fewer microstructural defects compared to the crystalline structure. The development of various BMGs enhanced its application as structural and functional materials in many industries such as electronics, aerospace, optics, biomedical, and sports equipment [6-11]. BMGs can provide various combinations of electric, magnetic and mechanical properties that cannot be achieved by crystalline metallic alloys or metal matrix composites [6]. Some of the applications of BMG are shown in Figure 1.1. For instance, BMGs are used in gears and miniaturized motors to increase wear resistance. BMGs are used in gearboxes for space rovers to withstand a low temperature (-150 °C) environment without the requirement of heating or lubrication [7]. BMGs have been used as moulding materials because of their high fracture toughness, high specific strength and wear resistance. BMGs moulds are electric and magnetic permeable and are independent of environmental factors [1,2,8]. BMGs are used as the casing material for handheld electronic devices [8]. The Surface quality and geometrical accuracy are primary factors that influence the functionality of the optical moulds, and BMGs are suitable as an optical moulding material because of their high surface integrity and corrosion resistance. BMGs have been used to produce optical components, e.g., the Fresnel lens [12,13,14]. In the field of medicine, bio-compatible BMGs have been used as a replacement for existing Ti alloys in medical devices, dental implants, and replacement implants for human joints [15]. BAM-11 BMG is well known for its biocompatibility, and the strength and corrosion resistance are higher than Ti alloys. The high electric and magnetic conductivity of BMGs enable their applications in micro-electro-mechanical devices [9]. BMGs also have been used as a coating material that can replace chromium coatings to enhance the performance of products such as space rover wheels and as a coating for corrosive moulding surfaces. Furthermore, the high elastic strain limit of BMGs is suitable for automobile valve springs, micro actuators, sports equipment such as tennis racket frames and golf equipment, etc. The stiffness and wear resistance make them ideal for strings of musical instruments [8].

Zirconium (Zr) - based BMGs have higher manufacturing ability, dimensional accuracy, and surface finish compared with other types of BMGs [17]. Zr-BMGs can be produced with a maximum thickness of 70 mm and specific strength of 295 Nm/g. A comparison of the maximum diameter that can be manufactured, the yield strength, fracture toughness, hardness, and specific Young's modulus for various BMGs with respect to their base elements is presented in Figure 1.2 [18]. The most widely used Zr-BMG materials in industrial applications are Vit-1 ($Zr_{41.2}Cu_{12.5}Ni_{10}Ti_{13.8}Be_{22.5}$) and Vit-105 ($Zr_{52.5}Ti_{5}Cu_{17.9}Ni_{14.6}Al_{10}$). The Zr-BMGs have yield strength in the range of 1.40 GPa - 1.83 GPa, hardness of 50-58 HRC, and around a 2% elastic strain limit.

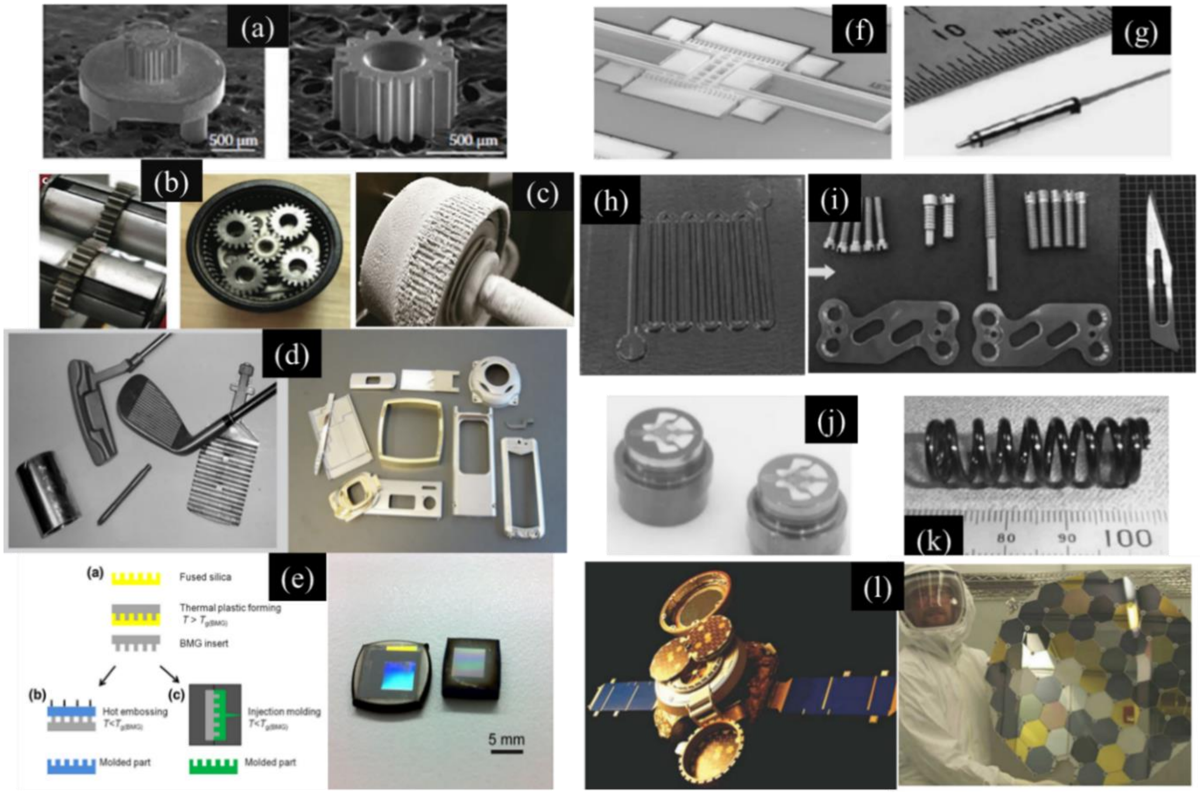

Figure 1.1 Examples of the BMG products in industry: (a) micro gears, (b) macro gears, (c) BMGs gears working at low temperatures, (d) sports equipment and casings, (e) micro-optical moulds, (f) MEMs, (g) micro motors, (h) fuel cell separators, (i) medical applications, (j) pressure sensors, (k) automobile spring (l) genesis spacecraft in collection mode, with one collector made of BMG [6-15].

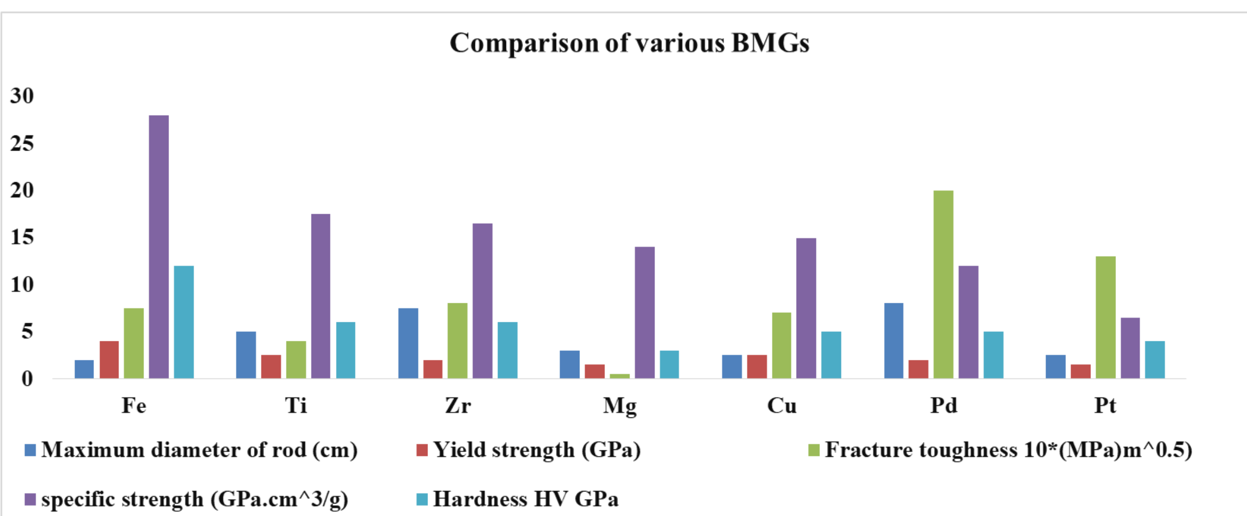

Figure 1.2 Comparison of maximum diameter achieved (cm), yield strength (MPa), fracture toughness (MPa$\sqrt{m}$), specific Young's modulus (GPa/(g/cm^3)) and hardness for BMGs based on the base element [1-2].

Machining operations such as turning, milling, and drilling are necessary to achieve the required geometric tolerance and surface quality of the Zr-BMG components. The machining processes cause plastic deformation of the workpiece material under large ranges of strains, strain rates and temperatures. Due to the unique amorphous structure, the material deformation mechanism of Zr-BMG in the machining processes is substantially different compared to the crystalline metal alloys or amorphous non-metallic materials. The deformation of BMGs is categorized into two major modes depending on the temperature, strain rate, and stress state. Inhomogeneous deformation mode occurs at high stress (close to the shear strength limit), low temperatures (in the range of 0.1 to 0.7 glass transition temperature (Tg)), and high strain rates. The inhomogeneous deformation of BMGs causes localized deformation, which involves periodic variations of the shear strains and stresses, resulting in shear band formation at the thicknesses of 10 -100 nm [19]. As a result, serrated chip formation occurs in the machining process and leads to rapid tool wear and reduced surface quality. The deformation changes to homogeneous mode at higher temperatures (above 0.7 Tg), lower stresses, and low strain rates [20]. Besides, when the temperature increases beyond the crystallization point, the originally amorphous microstructure of the BMGs becomes crystallized, which changes the machined surface's mechanical properties [4]. Overall, the material deformation and the surface generation mechanisms in machining BMG are highly dependent on the strain, strain rate, and temperature in the material deformation zone, which are influenced by the process parameters. Understanding the mechanisms of chip formation and surface generation in machining BMG is necessary to choose proper machining parameters and enhance the machining performance. Analyses of the material deformation and chip formation provide physical insight into the machining process. In previous studies from the literature, the chip formation analyses in the machining of BMGs were mainly based on experimental observations.

Other challenges in machining BMGs are fast tool wear or potential tool breakage due to the high strength and amorphous structure of BMGs. Vibration-assisted machining (VAM) has been implemented in machining hard and brittle materials to extend tool life and improve surface quality [21]. VAM is a methodology to impose controlled vibration to the existing motion of either tool or workpiece in the machining process, to facilitate periodic separation between the tool and the workpiece [21, 22]. The periodic separation of tool and workpiece changes the workpiece material's stress and temperature in the deformation zone, attributed to the modified kinematics of the tool or workpiece trajectory. However, to the author's knowledge, there has been no study of vibration assistance's effect on the deformation mechanism, chip formation, tool wear, and surface quality in machining BMGs.

The objective of this thesis is to understand the physics of the deformation process and chip formation mechanism in machining Zr-BMG. A new physics-based model is developed to predict the chip formation in orthogonal cutting of Zr-BMG. The model considers the machining kinematics, material constitutive property, heat generation and diffusion. The model is used to predict the chip segmentation mechanism due to the variations of the stress and temperature in the primary shear zone (PSZ). Based on the orthogonal cutting model of Zr-BMG, the mechanics of 2-D VAM of Zr-BMG is analyzed. In 2-D VAM, the assisted vibration motion is applied in both tangential and feed directions, which results in an elliptical trajectory at the tool tip. The effects of the vibration assistance parameters on chip formation, stress, and temperature variations in elliptical VAM (EVAM) of Zr-BMG are simulated. In addition, a 2-D vibration stage driven by piezo-electric actuators is developed and tested for EVAM machining experiments of Zr-BMG. The chip formation and the cutting forces obtained by the simulations from the mechanics model and the experimental results are compared and analyzed. In addition to the orthogonal cutting of Zr-BMG, the milling process of BMGs at higher cutting speeds is investigated in this thesis. Experimental analyses on the microstructure property of machined surfaces were performed to understand the amorphous-crystalline transition in the milling of Zr-BMG. The mechanics model of orthogonal cutting is extended to oblique cutting configuration, and the milling conditions corresponding to amorphous-crystalline transition are predicted and experimentally validated. Further experimental studies are performed to identify the effect of milling process parameters on microstructure properties in the generated chips and topography of machined surfaces.

The flow chart of the research content is shown in Figure 1.3. The Zr- BMG used in this thesis is commercially available material Vit-105. The mechanical properties of the Zr-BMG used in the study are presented in Table 1.1.

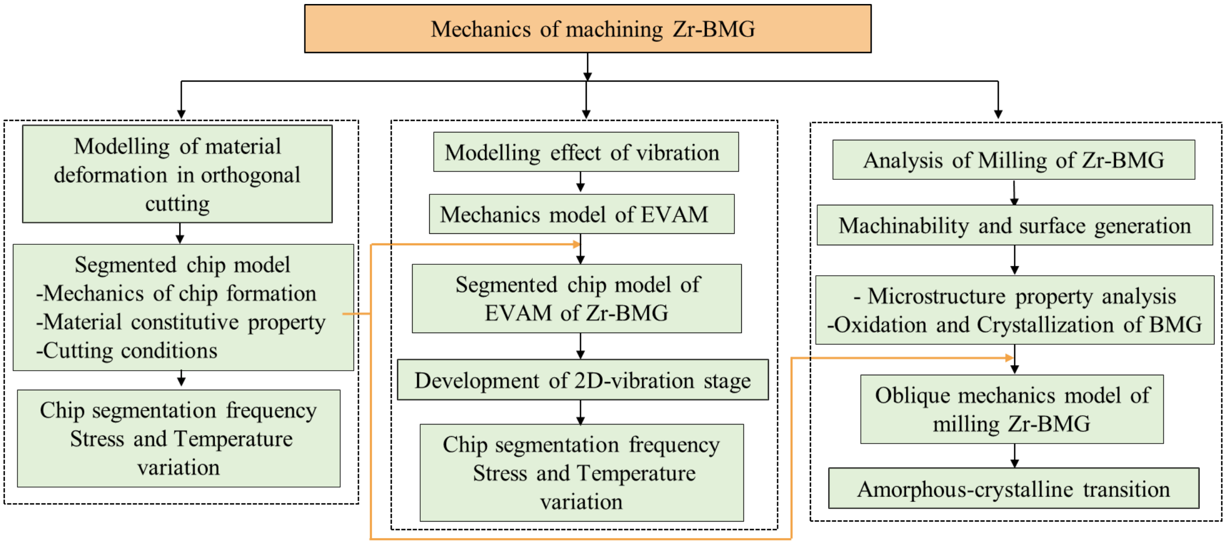

Figure 1.3 Overview of the research objective.

Table 1.1 Mechanical properties of Zr-BMG used in this thesis [1].

Material property	Value
Constituent elements (% wt)	Zr-65.7%, Ti-3.3%, Cu-15.6%, Ni-11.7% Al-13.7%
Density (kg/m^3)	6570
Hardness (HRC)	53 HRC
Poisson's ratio	0.38
Young's modulus (GPa)	92.7
Yield strength (MPa)	1524
Fracture toughness (MPa$\sqrt{m}$)	50
Glass transition temperature (°C)	400

The thesis structure is organized as follows: A detailed literature review on machining BMGs, chip segmentation in machining, and vibration-assisted machining is presented in chapter 2. Chapter 3 proposes the physics-based chip formation model for orthogonal cutting of Zr-BMG. The material flow stress and temperature in the PSZ are modelled based on the material constitutive property of BMG along with heat generation and diffusion. The simulated chip formation is validated by orthogonal cutting experiments in a range of cutting speeds and uncut chip thicknesses. Chapter 4 presents the mechanics model of EVAM of Zr-BMG. The effect of the elliptical trajectory on the shear angle, the chip formation, and stress variation in EVAM of Zr-BMG is determined. In Chapter 5, a piezo-driven 2-D vibration stage is developed to perform experimental studies on EVAM of Zr-BMG. The 2-D vibration stage's dynamic property is experimentally determined, and EVAM is conducted to validate the mechanics model by comparing the chip morphology. Chapter 6 presents the amorphous-crystallization phenomenon of workpiece material in milling of Zr-BMG. The light emission and its effect on the microstructure property of the machined surfaces and chips are determined. The physics-based model on the oblique cutting of Zr-BMG is used to identify the process parameters which result in the crystallization of the workpiece material. The simulated results are validated by experimental studies using X-ray diffraction examinations. The conclusions of the thesis and the future research directions are presented in Chapter 7.

Chapter 2

Literature Review

2.1 Overview

This chapter is focused on the literature review on state of the art in machining of BMGs. The mechanics of machining BMGs including chip formation, surface finish, and tool wear in various machining operations, are presented. The mechanisms of shear localization and chip segmentation in machining metallic materials and BMGs are discussed. In addition, a review of vibration-assisted machining technology and its effects on machining performance are discussed.

2.2 Experimental studies on machining of BMGs

The studies on machining of BMGs were first reported by Ueda and Manabe [25] in 1992. Experimental studies and FE simulations on chip formation in turning of Pb-BMG were presented. Segmented chip formation was observed at very low cutting speeds (less than 1 m/min). It was concluded that the segmentation spacing is proportional to the uncut chip thickness. Bakkal et al. [23] investigated the machining process of commercially available Zr-BMG model Vit-1. Experimental studies on various machining operations of Zr-BMG, including turning, drilling, and grinding, were reported subsequently [23-25, 27-31]. It was shown that machining of BMGs produces a strain-softening effect, as opposed to the strain hardening observed in crystalline metal alloys. Light emission occurs in the turning of Zr-BMG due to the machined chips' oxidation at an elevated temperature at high cutting speeds. The temperature rise associated with the light emission is approximately 2,700 K [26]. The increase in temperature due to oxidation results in the crystallization of chips, while the machined surface retains the original amorphous microstructure [24, 27]. Continuous chips with lamellar structures containing shear bands were formed in the machining process due to repeated shear localization [28]. The cutting forces are higher, and the tool wear occurs more rapidly in machining BMG compared to AISI 304 steel and aluminum 6061 alloy under the same machining conditions [23,24,28], which is due to the higher strength and lower thermal conductivity of Zr-BMG. The electron microscopic studies on the crystallized chip found that the crystalline phase on the chip's outer surface is Zr_2O, and inside the chip are Zr_2Cu, $ZrAl_2$, and Zr_2Ni [29].

Fujita et al. [30] performed turning experiments on Zr- and Pd- based BMGs, and studied the machinability in comparison with brass and steel. The BMGs showed better surface quality compared to crystalline metals. It was found the built-up edge did not occur due to lower uncut chip thicknesses and higher thermal conductivity of the diamond tool in cutting BMG. Flow-type chips with small spaced slips representing chip segmentation were observed. Han et al. [31] conducted turning experiments on Zr-BMG and observed that the surface roughness of BMG was lower at higher cutting speeds. The nano-scratch experiments showed that the chip formation is a result of inhomogeneous deformation. A molecular dynamics simulation conducted by Zhao et al. [32] showed that crystallization occurs in machining, which is dependent on the temperature and stress state in the primary shear zone.

Experimental investigations on the drilling of Zr-BMG were investigated by Bakkal et al. [28]. It was shown that tool chipping and wear occur even for a short machining length attributed to the high hardness of BMG (> 65 HRC). It was observed that the tool diameter, feed speed, and spindle speed influence the intensity of the light emission in the drilling process, whereas in turning, only cutting speed is the dominant factor for the light emission. Different chip shapes such as powder, spiral, ribbon, and tangled ribbon were formed at different drilling parameters. The drilling tool's material plays a prominent role in heat conduction and light emission in the drilling process. The magnitudes of the drilling forces decrease with the increase of light emission intensity. The light emission influences the surface quality of the holes in the drilling process. Zhu et al. [33] conducted micro-drilling experiments on Vit-1. It was observed that the increase in cutting speed and chip load resulted in a rapid increase in temperature. Crater wear on the rake face was dominant compared to the flank wear of the drilling tool.

The studies on the grinding of Zr-BMG found that the temperature can reach beyond the glass transition temperature [34]. In addition, lower cutting speeds result in the increase of temperatures due to extended contact time between the tool and workpiece, resulting in the crystallization of the machined surface. Yin et al. [35] conducted grinding experiments on Zr-BMG, and found that higher grinding speed results in brittle material removal. A larger quantity of BMG is loaded into the grinding area at a higher speed, resulting in rubbing and an increase in temperature. Small ribbon and fragmented chips were observed with larger grinder grits. Zhang et al. [36] studied the tool wear in grinding of Zr-BMG and SS304 with different grinder abrasives and bond strengths.

It was reported that Ni electroplated diamond and cubic boron nitride tools produce better surface quality and low tool wear rate due to low adhesion of BMG material compared to Cu-Sn-Ti brazed diamond tools. It was determined that machined surface crystallization did not occur when the grinding speed is below 315 m/min and uncut chip thickness smaller than 40 μm.

Few experimental studies in the literature are focused on the surface quality related to machining processes. Milling of Zr-BMG and its influence on the microstructure property of Zr-BMG is seldom reported. A comparative study of milling of Zr-BMG, Al 6061, and SS 304 stainless steel was conducted by Bakkal and Naksiler [37]. It was observed that the cutting force magnitudes in milling Zr-BMG are lower compared to SS304, which is attributed to the softening effect of the BMG at higher cutting speeds. Excessive burr formation was observed with the increase of cutting speed, leading to a poor surface finish with rollover burr formation. The effect of milling conditions on microstructure property, light emission and tool wear are not reported. Wang et al. [38] studied the surface roughness and top burr formation in micro-milling of Zr-BMG. The size effect at lower uncut thickness on specific cutting force and shearing-ploughing transition was investigated. A mathematical model was developed to predict the surface roughness and top burr formation in the micro-milling of Zr-BMG.

Zhang et al. [39] conducted a review on micro-machining of BMGs including diamond turning, laser processing and micro-electric discharge machining processes. The chip formation, surface generation, microstructure morphology, crystallization and oxidation of machined surfaces were investigated. Wessels et al. [40] compared the machinability of Zr- BMG in various machining methods such as laser machining, abrasive water jet cutting, electro discharge machining (EDM), and end milling for producing a BMG screw in a medical implant. XRD analyses revealed no crystallization in abrasive water jet cutting due to the heat extraction from the cutting zone by water. Surface melting and crystallization were observed in laser machining and EDM of BMG. The end milling process did not result in surface crystallization at lower speed, while crystallization occurred when the milling speed increases beyond a critical value. Parlar et al. [41] conducted sliding wear tests on Zr-BMG to understand the tribological properties of BMG, which can be used to model the tool-chip friction in the machining process. It was observed that the friction coefficient is approximately 0.45 and 0.7 at low speeds. A vein-like pattern was identified on the surface, attributed to the material melting at high temperature and adhesive wear.

The results in the literature on machining of BMGs show that the deformation of BMG in machining is highly sensitive to the strain rate, stress, and temperature variation in the deformation zone. The deformation process of BMGs in machining can be broadly classified into three major groups based on chip formation and temperature in the primary shear zone (PSZ), as shown in Figure 2.1. Segmented chip formation is the primary mode of deformation at low cutting speeds. It is an inhomogeneous deformation that occurs at low strain rates and temperatures. No crystallization of the machined surface is observed because most of the heat generated in the deformation zone is localized into the shear band, while the macroscopic temperature rise is low. The second category is a non-uniform continuous chip with crystallization at higher cutting speeds (generally greater than 100 m/min [23]) where the temperature rise is significant. Most of the heat is carried away by the machined chips, while the machined surface keeps an amorphous state. The temperature rise in the chip results in the crystallization of chip material, along with light emission in the machining process. When the temperature in the deformation region increases further, there is a possibility of crystallization of the amorphous microstructure of BMG on the machined surface, which potentially degrades the surface integrity. The third category is the formation of discrete and oxidized chips with no regular structure at very high cutting speeds (greater than 300 m/min) and feed rates in grinding, and in unconventional machining processes (laser machining and EDM). This category does not involve the strain localization or chip segmentation. However, the temperature rise in the PSZ is much higher than the glass transition temperature of Zr-BMG. Therefore, material crystallization or melting occurs in both chips and machined surfaces.

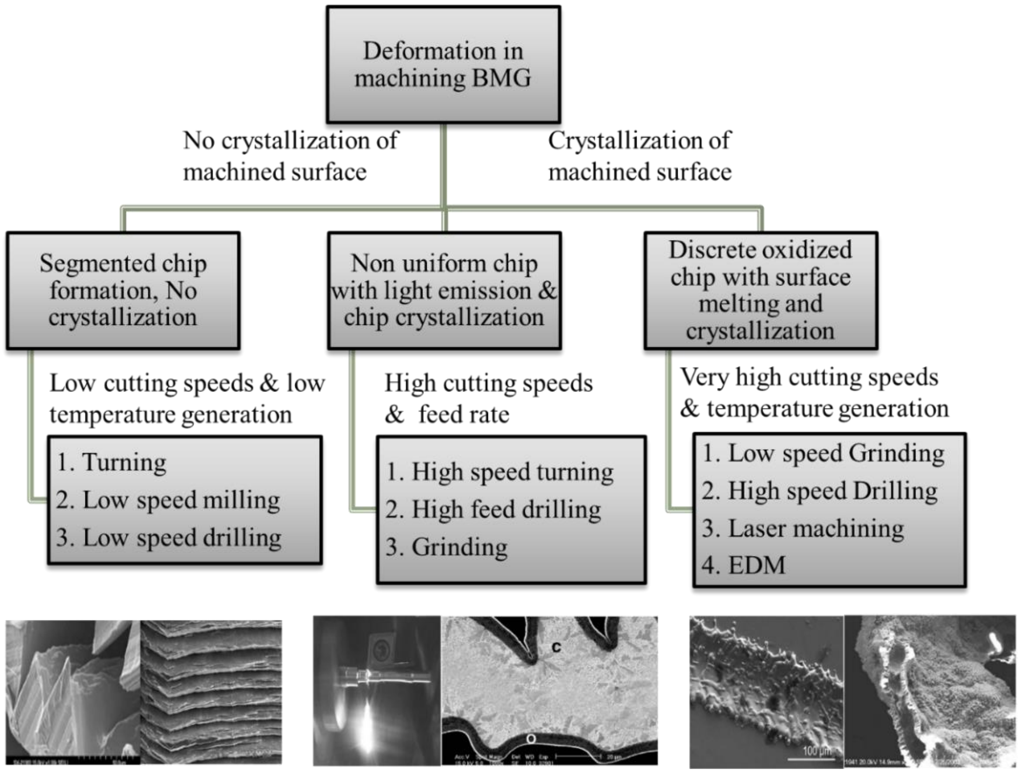

Figure 2.1 Classification of chip formation in machining of Zr-BMG.

Moreover, the literature work was primarily focused on experimental and qualitative observations of chip formation, crystallization, tool wear and surface roughness in various machining operations of BMGs [39, 40]. Very few studies were reported on modelling the mechanism of the deformation regarding the strain rates, temperature, and microstructure property in the deformation zone. The mechanism of the deformation of BMG in the machining process is still unclear. Hence, it is essential to understand the deformation mechanism of Zr-BMG in the machining process in order to optimize the process parameters and enhance the machinability.

2.3 Inhomogeneous deformation in machining

2.3.1 Chip segmentation in machining crystalline metal alloys and BMGs

In the machining process, the material deformation occurs at large strain, high strain rates, and high temperature in the PSZ. Understanding the material deformation mechanism of BMG in the machining process establishes the basis for evaluating the process performance. Microstructural features such as dislocation motion, defects (voids, porosity, and cavities) associated with grains and grain boundaries are the primary source of plastic deformation for crystalline metal alloys.

While these defects are absent in BMGs with an amorphous structure, the deformation occurs by the microscopic phenomenon of atomic jumps or molecular motion into the neighbouring free space, defined as free volume. The schematic representation of deformation in machining crystalline materials and BMGs is presented in Figure 2.2.

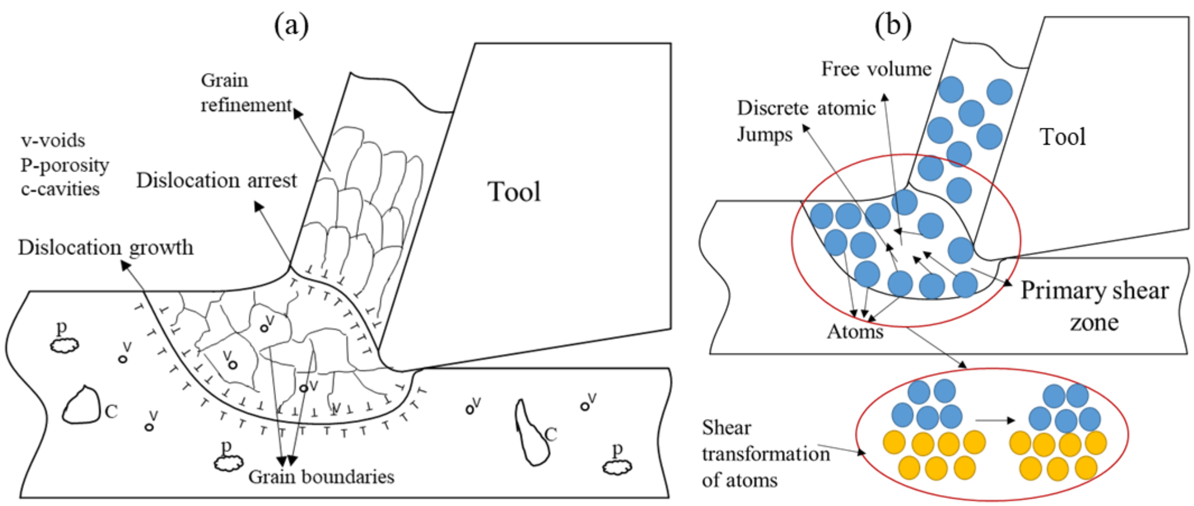

Figure 2.2 Schematic representation of cutting: (a) crystalline materials, and (b) BMGs.

Experimental examination of chip formation in machining BMGs [23] shows that when inhomogeneous deformation occurs in PSZ, the shear deformation is localized in a thin shear band of 10-100 nm thickness. The shear strain of the surrounding material is lower compared to the material inside the shear band. The segmented chip formation is caused by periodic variation of stress and temperature in the PSZ, which has a negative effect on the tool life [42]. Besides, segmented chip formation affects the surface finish and dimensional accuracy of the component [43]. Although the chip formation with periodic segmentations also occurs in machining crystalline metal alloys such as Ti6Al4V, Inconel, hardened steels, etc., the segmented chip formation mechanism in machining BMGs and crystalline metal alloys are substantially different. For crystalline materials, the segmented chip formation occurs only when the cutting speed exceeds a critical value, depending on the material property and uncut chip thickness. The critical cutting speed at which the segmentation occurs for an uncut chip thickness of 100 μm is around 60 m/min for Ti6Al4V, around 140 mm/min for Inconel 718, and at very high cutting speed of 700 m/min for aluminum 7075 [44]. The origin of the chip segmentation in machining crystalline metal alloys is explained by two mechanisms. One is the shear localization caused by thermal softening inside the shear band, and the other is periodic microcrack generation in the PSZ. Figure 2.3 shows two distinct regions in the segmented chips in machining Ti6Al4V [45]. One region contains a localized shear band with a thickness of 5 - 10 μm, while other regions in the segments have less or no deformation. It is assumed that around 80%-90% of the work in the machining process due to plastic deformation is converted to heat in the PSZ. When the cutting speed exceeds a critical value, the heat generation due to the deformation is not dissipated at the same rate. As a result, the thermal softening increases, and the shear stress decreases with the increase of shear strain, resulting in shear localization and segmented chip formation.

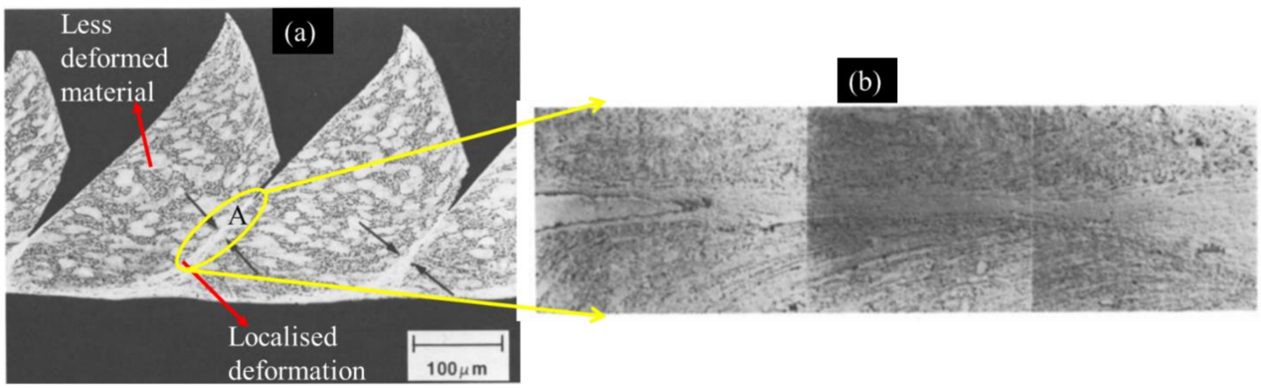

Figure 2.3 (a) Segmented chip formation in Ti6Al4V, and (b) enlarged view of localized flow in region A [45].

Recht [46] first proposed that thermal softening is the primary reason for the segmented chip formation in machining crystalline metal alloys such as Ti6Al4V and steels. Cooke and Rice [47] conducted pioneering experimental work to show that the inhomogeneous deformation occurs at higher cutting speeds, and concluded that the segmentation does not originate from microcrack generation. Turkovich et al. [48] concluded that the segmentation is due to the thermally activated strain-softening in crystalline materials. Later, Hou and Komanduri [49] conducted experimental analyses and developed an analytical model considering the thermal energy balance in the PSZ, to predict the critical cutting speed corresponding to the onset of chip segmentation. The model did not consider the material flow behaviour during deformation and cannot predict the segmentation frequency.

Later, Recht [50] proposed that the change in shear stress in PSZ is primarily due to the inertial force originating from large strain generated at very high cutting speeds (1,500 m/min). Following Recht, Dudzinski and Molinari [51] developed an analytical model considering the effects of inertial force, material constitutive flow law, and thermal energy balance to predict the spacing of chip segmentation at very high cutting speeds in machining crystalline materials. However, in machining BMGs, segmented chip formation also occurs at a low cutting speed range (e.g. lower than 1 m/min) [25]. Therefore, the shear localization due to thermal softening at high cutting speeds in machining crystalline metal alloys cannot be directly used to explain the inhomogeneous deformation and chip segmentation in machining BMGs. In addition to the thermal imbalance, it is necessary to understand the constitutive property of BMGs to study the chip segmentation mechanism in the machining process.

2.3.2 Material deformation mechanism of Zr-BMG

The physics of deformation and the material constitutive flow law for metallic glasses was first proposed by Spaepen [52]. Unlike crystalline materials, the deformation process in BMG is considered to originate from a microscopic phenomenon facilitated by atomic jumps. Although the exact nature of the atomic-scale rearrangements is not solved completely, it is assumed that the atoms squeeze into a neighbouring void space due to the applied stress, as shown in Figure 2.4. The rate at which the atomic jumps occur depends on the applied stress and the amount of void space available per atom. The neighbouring void space between the atoms in an amorphous structure is called free volume [53,54].

Compared to crystalline metal alloys, the amorphous microstructure has extra void space (free volume) due to the absence of short-range periodicity. It is assumed that the macroscopic deformation results from the combination of individual atomic jumps that occur within the available free volume. To facilitate an atomic jump, activation energy should be supplied to the atom. If there is no external stress applied, the atoms' diffusion may occur due to thermal activation. The number of atoms crossing the barrier is the same in both directions, and there is no net flow of atoms. However, when the external stress is applied, the number of atomic jumps in the direction of the stress (forward) is more than the atomic jumps in the reverse direction, facilitating an atomic flow biased in the direction of the applied stress.

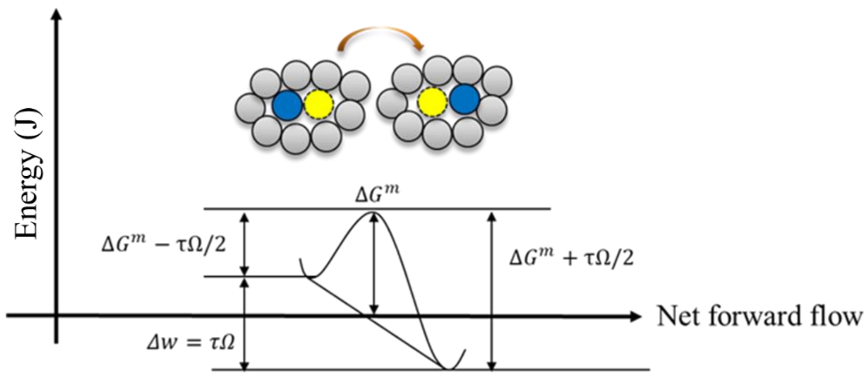

Figure 2.4 Schematic presentation of individual atomic jump responsible for deformation.

For BMG materials, the shear strain rate depends on the applied stress, free volume creation by the external stress, and free volume annihilation by diffusion, expressed as [52]

$$\dot{\gamma}_p = \text{(fraction of potential-jump sites)} \times \text{(net number of forward jumps per sec)}$$

$$= \Delta f \times 2\omega \exp\left(-\frac{1}{\zeta}\right) exp\left(\frac{-\Delta G_m}{K_b T}\right) sinh\left(\frac{\tau\Omega}{2K_b T}\right) \tag{2.1}$$

where Δf is the fraction of sample volume in which jump sites can be found. For inhomogeneous deformation which corresponds to $\Delta f \leq 1$, ω is the frequency of atomic vibration, $1/\zeta$ is the free volume parameter equal to xv^*/v_f, where x is the geometric factor between 1 and 0.5, v_f is the average free volume of an atom, v^* is the effective hard-sphere volume of an atom. ΔG^m is the activation energy required for an atom to overcome the barrier, K_b is Boltzmann constant, Ω is the atomic volume, T is the temperature, and τ is the applied stress.

Eq. (2.1) shows that the shear strain rate is a function of the applied stress τ, free volume ς, and temperature T. It should be noted that the flow and free volume is controlled by stress in inhomogeneous deformation (at low temperature and high-stress values), unlike the homogenous deformation where the temperature controls the flow regime [55].

Argon [56] proposed that the deformation of metallic glasses is due to local rearrangements of a group of atoms defined as the Shear transformation zone (STZ). The deformation is caused by local shear transformations originated by applied stress with thermal effect in the neighbouring free volume. The schematic representation of atomic rearrangement is presented in Figure 2.5. The explanation for the plastic flow is identical to that proposed by Spaepen. During homogenous flow at higher temperatures, the shear transformation is due to diffusive rearrangement of a local shear strain, which approximately occurs in a spherical region. At low temperatures, the deformation occurs in a narrow disc region and results in inhomogeneous deformation. Later, Argon and Shi [54] revealed that the activation energy required for a shear transformation in metallic glasses is given by

$$\Delta F_o = \left[\frac{7-5\upsilon}{30(1-\upsilon)} + \frac{2(1+\upsilon)}{9(1-\upsilon)}D^2 + \frac{1}{2\gamma_o\mu(T)}\tau_{at}\right]\gamma_o{}^2\Omega_o\mu(T) \tag{2.2}$$

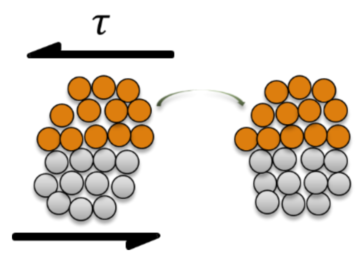

Figure 2.5 Shear transformation of STZ.

where $\mu(T)$ and υ are temperature-dependent shear modulus and Poisson's ratio of the glass respectively, D is the dilation parameter of STZ, which approximately equals unity in BMGs. Ω_o is the volume of STZ, τ_{at} is the athermal shear stress required to activate the shear transformation, equivalent to the ideal shear strength. The resultant shear strain rate is given by [57]

$$\dot{\gamma_p} = \alpha_o\gamma_o\omega_o\, exp\left(\frac{-\Delta F_o}{K_bT}\right) sinh\left(\frac{\tau\Omega}{2K_bT}\right) \tag{2.3}$$

where α_o is the fraction of material undergoing shear transformation (related to free volume), ω_o is the frequency of an individual STZ, and τ is the applied stress. It should be noted that the shear strain rate in Eq. (2.3) is derived for homogenous flow [55, 56], assuming the shear transformation occurs in approximately a spherical region. Argon proposed that the activation energies are the same at all temperatures. The theory of microscopic deformation by Spaepen [52] and Argon [56] were recognized as the fundamental theories to characterize the deformation of BMG.

In addition, Bulatov and Argon [58] developed a mesoscale model for the deformation of metallic glasses. The fundamental difference in this model compared to Spaepen [52] and Argon models [56] is that the material flow is assumed to result from a sequence of STZ transformations. Each STZ is considered as an element of weakness that undergoes inelastic deformations. After one transformation, the stress field is redistributed, and new STZ transformations occur. Following

Bulatov and Argon's work, Homer and Schuh [59] established a 2-D finite element model to simulate the inelastic behaviour of BMGs. It is observed that the shear localization does not entirely depend on the thermal effect. The model could predict plastic behaviour for homogenous flow, but failed to simulate shear localization in BMGs due to the lack of free volume parameter in the model. Therefore, it is necessary to include free volume and material constitutive flow law to understand the mechanism of segmented chip formation in the machining of Zr-BMG.

A few physics-based models of chip formation in machining BMGs are available in the literature. Zhao et al. [60] developed an analytical model to predict the cutting force and temperature based on the Mohr-Coulomb criterion for cutting metallic glasses. The model considered the effect of pressure and temperature on the stress at the shear plane. However, the shear band formation and chip segmentation were not analyzed. Ding et al. [61] investigated the chip deformation in orthogonal cutting of Zr-BMG at cutting speeds varying from 1.8 m/min to 10.2 m/min. It was reported that the cyclic variation of the cutting forces occurs due to segmented chip formation. The presence of secondary shear bands was reported without explaining the related mechanism. The reduction in shear stress during chip segmentation was attributed to the thermal softening effect. However, a systematic study of chip formation considering the effect of material flow and free volume was not reported.

Jiang et al. [62] investigated the chip segmentation in turning of Zr-BMG considering the effect of material constitutive property, strain rate, free volume, and temperature in the PSZ. A thermo-mechanical model based on the microscopic deformation model by Spaepen [52] was established to explain the segmentation phenomenon and temperature variation in the deformation zone. It is concluded that shear instability was not initiated by temperature, as the temperature variation in the deformation zone was insignificant compared to free volume. In contrast, recent studies showed that the average temperature rise of BMG at low strain rates in the shear band is about 200 K [63]. Besides, the predicted results such as chip segmentation frequency and temperature from the model do not match with the experimental results. Therefore, further studies are necessary to investigate the chip segmentation mechanism in machining of BMG.

To address this gap, in this thesis, a physics-based model is developed for machining Zr-BMG including the material constitutive flow law, the thermal energy balance, and the microstructure property of Zr-BMG. The objective of this model is to understand the chip formation mechanism, and predict the segmentation frequency, variation of cutting stress, and temperature in the PSZ, in the orthogonal cutting of Zr-BMG.

2.4 Vibration-assisted machining technology

Rapid tool wear is a primary limiting factor in machining Zr-BMG, affecting machinability, cutting temperatures, and machined surface quality [64]. Vibration-assisted machining (VAM) was proposed to overcome these challenges in machining high-strength materials such as titanium alloys, nickel alloys, metal matrix composites, and brittle materials, including glasses and ceramics [65]. VAM is a method of imposing controlled vibration with an amplitude ranging from 2-40 μm and frequency between 2-40 kHz on the cutting tool or workpiece in addition to the existing relative motion between the tool and workpiece [22]. The assisted vibration motion is generated by the piezoelectric or magnetic actuators, and is mechanically transmitted either to the tool or workpiece. The advantages of VAM include reduced cutting forces and stresses, reduced cutting temperature, extended tool life, and improved surface quality [21,22,65,66]. VAM has also been used for drilling operations in industries to reduce the chip load, produce short chips, and facilitate chip evacuation [22,65].

The primary feature of VAM is the intermittent contact between the cutting tool and the workpiece. The tool-workpiece separation occurs at periodic intervals determined by the frequency and the amplitude of vibration assistance. As the tool-workpiece contact is intermittent, the force varies continuously, and the average force required is lower compared to conventional machining [21]. The kinematics of the VAM and tool-workpiece separation is presented in Figure 2.6 [21,22]. In 1-D VAM, the harmonic displacement due to vibration assistance is applied in the cutting direction. In 2-D VAM, the vibration motions are applied simultaneously in tangential and thrust directions with a phase difference, to form a circular or elliptical trajectory at the tool tip.

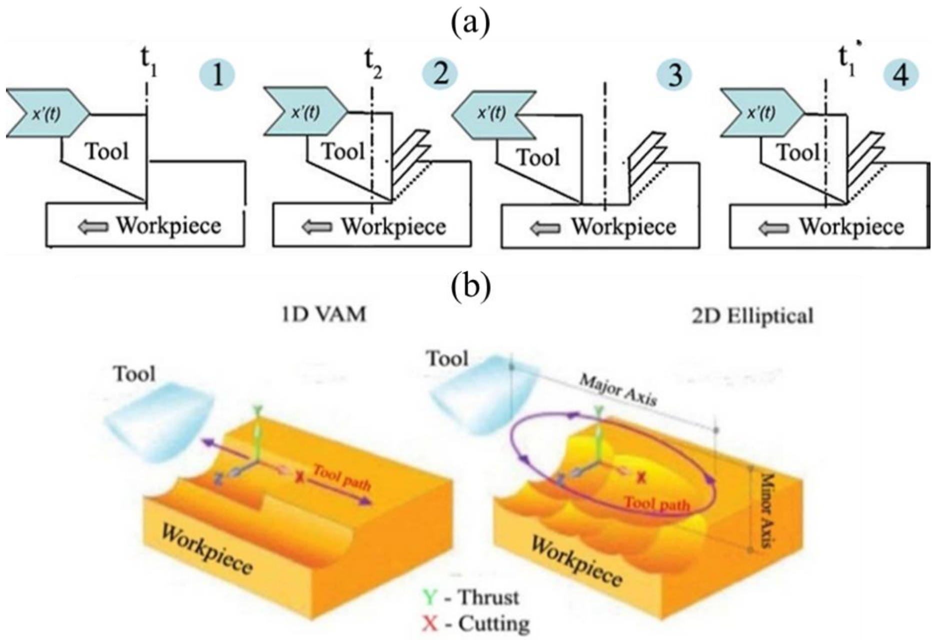

Figure 2.6 (a) Kinematic of 1-D VAM, and (b) comparison of 1-D and 2-D VAM [21,22].

The typical chip formation process in 2-D elliptical VAM is categorized into three types, as shown in Figure 2.7 [67,68]. In type 1, discrete chip formation is observed when the uncut chip thickness is lower than the amplitude of vibration assistance in the y-direction (A_y). In type 2, when the uncut chip thickness is below $2A_y$, a continuous chip with periodic segments is observed, while the uncut chip thickness changes continuously due to the tool tip trajectory with vibration assistance. The transient uncut chip thickness results in cyclic segments, as shown in Figure 2.7 (type 2), which is due to the chip's uplifting effect [68,69]. VAM resulting in types 1 and 2 of chip formation are mainly used in machining brittle materials such as glass and ceramics. In VAM of brittle materials, the critical uncut chip thickness is limited by the deformation mode transitioning from ductile damage to brittle fracture [68]. For type 3, a continuous chip is generated when the uncut chip thickness is greater than $2A_y$. VAM, which generates chip formation of type 3, has been commonly used in machining ductile metallic alloys [62-64].

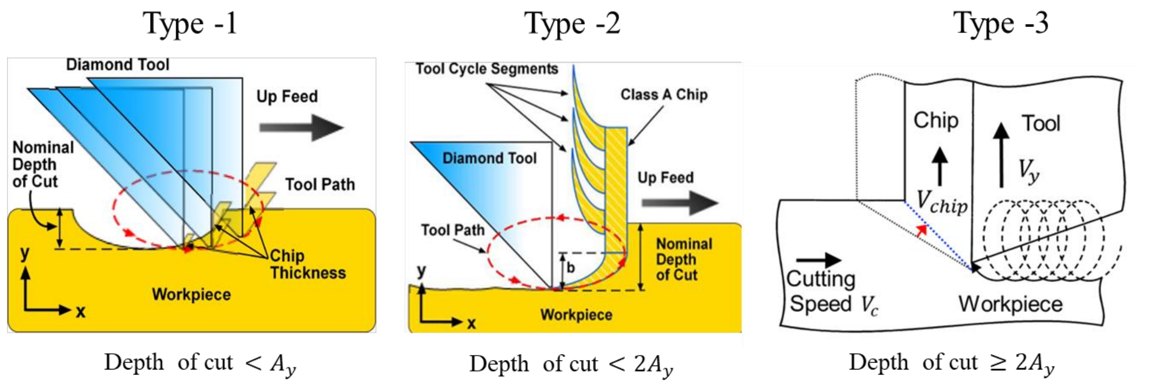

Figure 2.7 Classification of chip formation in 2-D elliptical VAM [54,55].

In each VAM vibration cycle, the tool-workpiece contact time is usually less than half of the whole vibration period. When the tool and the workpiece are separate, there is no plastic deformation or heat generation in PSZ, and heat dissipation and stress relaxation occur. However, no study has been reported on quantifying the effect of vibration assistance on machining BMGs. Hence, the questions that whether vibration assistance can improve the machinability of Zr-BMG, and how the vibration parameters influence the chip formation, stress, temperature, and potential crystallization remain unanswered. In this thesis, a mechanics model of 2-D VAM is developed to include the effect of periodic tool-workpiece separation on the deformation mechanism and stress variation in PSZ in machining Zr-BMG. Moreover, a 2-D vibration stage driven by piezo-electric actuators is developed to experimentally analyze the effect of VAM on machining Zr-BMG and validate the mechanics model.

Chapter 3

Modelling of Segmented Chip Formation in Orthogonal Cutting of Zr-BMG[1]

3.1 Overview

Analysis of chip formation is essential to understand the deformation mechanism of Zr-BMG in the cutting process. Chip segmentation occurs due to inhomogeneous deformation and shear localization in cutting Zr-BMG [23]. The segmented chips result from periodic variations of stress and temperature in the primary shear zone (PSZ), and is detrimental to the tool life, machined surface quality, and dimensional accuracy of the machined component [39,40]. The literature studies show that the mechanism of chip segmentation in machining Zr-BMG differs from crystalline metal alloys. BMGs show segmented chip formation even at low cutting speeds of 1 m/min [25]. At such low cutting speeds, the effect of heat generation and thermal softening is lower compared to the chip segmentation mechanism in machining crystalline metal alloys. To understand the chip formation in machining BMGs, the material deformation in PSZ should be evaluated with respect to the cutting parameters.

This chapter proposes a physics-based model to predict the chip formation, stress, and temperature variation in PSZ in orthogonal cutting of Zr-BMG. Segmented chip formation in Zr-BMG is a thermomechanical problem that includes applied stress by cutting tool, material microstructure property, and temperature. A mesoscale material constitutive model along with free volume parameter is included in the model to predict the inhomogeneous deformation in machining Zr-BMG. A flow chart to solve the thermomechanical problem is presented in Figure 3.1. The critical steps to analyze the deformation behaviour require modelling chip kinematics, material constitutive flow law, free volume evolution, and thermal energy balance in machining Zr-BMG. The inputs to the model are cutting condition parameters such as cutting velocity, uncut

---

1. The content of the chapter 3 has been published in a Journal article: Maroju, N. K., & Jin, X. (2019). Mechanism of Chip Segmentation in Orthogonal Cutting of Zr-Based Bulk Metallic Glass. ASME Journal of Manufacturing Science and Engineering, 141(8), 081003.

chip thickness, measured process parameters such as shear angle, coefficient of friction, assumed process parameters including shear plane thickness, chip tool contact length and workpiece material properties such as shear modulus, Young's modulus, Poisson's ratio, critical shear stress, critical shear strain etc. The modelling process starts with the kinematic model of chip formation, which provides the evolution of the shear stress (governing equation of shear stress) in the PSZ as explained in detail in Section 3.2. The material constitutive law (governing equation of material flow) including free volume evolution (free volume generation and diffusion) and temperature evolution (temperature generation and dissipation) in PSZ are from literature, and their governing equations are explained in detail in Sections 3.2 - 3.4 respectively. Solving these four fundamental governing equations, the oscillations of the shear stress, temperature, and free volume in PSZ responsible for the chip segmentation are predicted. The simulated chip segmentation frequency is validated by orthogonal cutting experiments of Zr-BMG in a range of cutting speeds and uncut chip thickness values.

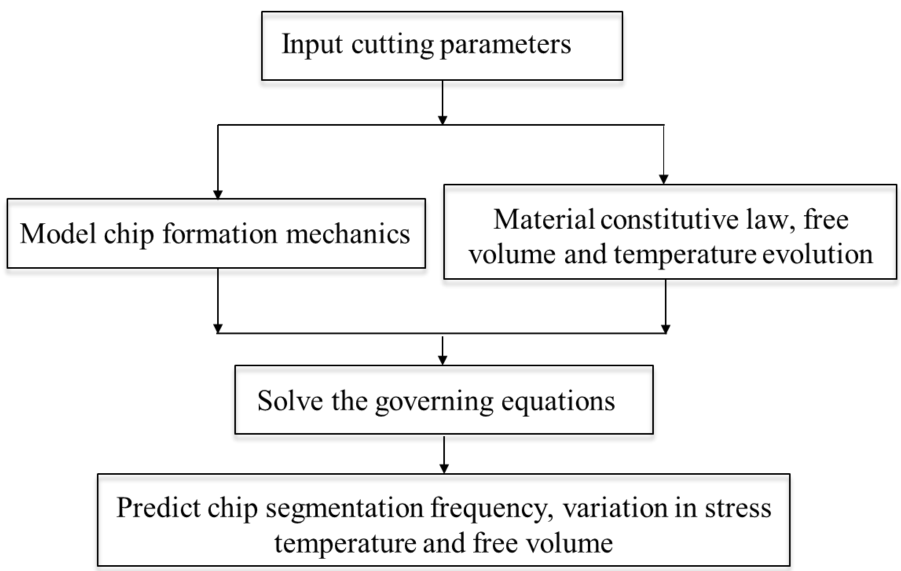

Figure 3.1 Flow chart to model the chip segmentation in machining BMG.

3.2 Modelling of shear stress variation

The schematic of the chip formation in orthogonal cutting of Zr–BMG is shown in Figure 3.2. When the workpiece material with uncut chip thickness of h_{un} enters the PSZ, the cutting velocity V_c changes to the chip velocity V_f due to the shearing effect. The shear stress τ in the PSZ increases, causing plastic deformation of the workpiece material. As a result, the plastic deformation energy creates the free volume and increases the temperature in PSZ. The increase in temperature and free volume has a softening effect on shear stress. When the material softening is more dominant than the free volume and thermal diffusion, shear localization occurs, and the shear stress in PSZ decreases until new material enters and initiates a new cycle of stress variation. The variations of shear stress, temperature, and free volume in PSZ due to the coupled thermo-free volume-mechanical effect result in the variation of shear strain, and therefore the chip segmentation. In this study, the shear stress variation in PSZ related to the material kinematics, the constitutive model of Zr-BMG, the generation and dissipation of the temperature and free volume concentration was modelled.

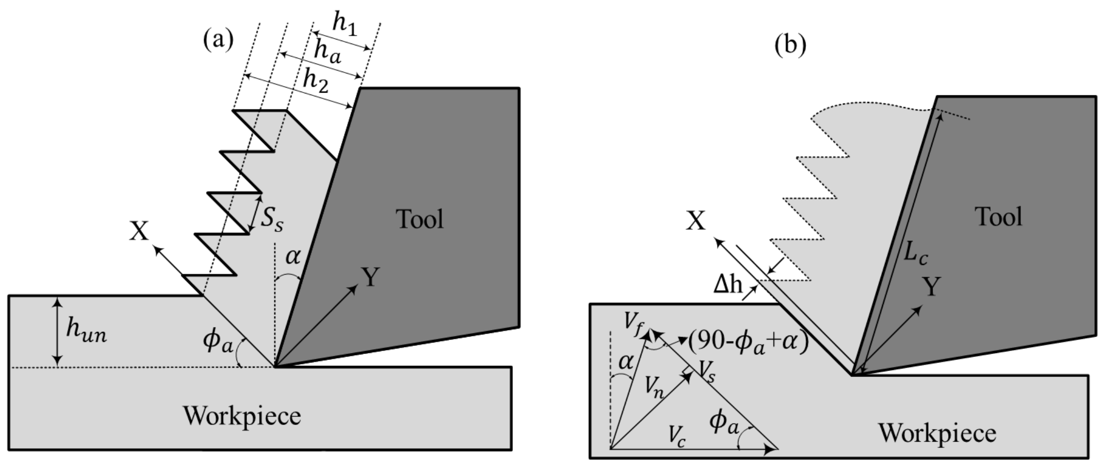

Figure 3.2 Schematic representation of (a) segmented chip formation, and (b) PSZ and velocity diagram.

As shown in Figure 3.2, the measured average thickness of the segmented chip is $h_a = (h_1 + h_2)/2$, where h_1 is the minimum and h_2 is the maximum chip thickness due to segmentation. 2-D plane strain condition is applied in modelling the material deformation. The shearing is assumed to occur in the PSZ with the thickness of Δh (assumed to be constant value) at an experimentally identified shear angle of ϕ_a . The area of material shearing is $A_s = h_{un}b/sin\phi_a$, and the tool-chip contact area is $A = L_c b$, where L_c is tool chip contact length (assumed to be constant value) and b is the width of cut. The coordinate *x*-axis is along the shear plane, and *y* is normal to the shear plane. The average shear velocity in PSZ is $V_s = V_c \cos\alpha \,/\, \cos(\phi_a - \alpha)$, and the average strain rate is $\dot{\gamma}_s = V_s/\Delta h$. When the strain rate increases beyond the average strain rate value due to shear localization, chip segmentation occurs. V_L represents the instantaneous shear velocity associated with chip segmentation, and the corresponding instantaneous strain rate ($\dot{\gamma_p}$) is expressed as $\dot{\gamma_p} = V_L/\Delta h$.

The forces applied to the machined chip is shown in Figure 3.3. In the model, the momentum equilibrium condition is applied on the machined chip, and it is assumed that the resultant force (R) on the shear plane is equal in magnitude and opposite in direction with the resultant force (R') on the tool-chip interface. Therefore, the inertial force of the machined chip is neglected. Quantitative analysis on the effect of inertial force on the model will be discussed in Section 3.6.2. As shown in Figure 3.3, the angle between the normal force on the rake face (N) and the shear plane is $(\phi_a - \alpha)$. The shear force F_s is derived by projecting the normal force (N) and frictional force (F) along the shear plane direction, expressed as

$$F_s = N\cos(\phi_a - \alpha)[1 - \mu tan(\phi_a - \alpha)] \tag{3.1}$$

where μ is the average friction coefficient at the tool rake face (measured from cutting experiments). Therefore, based on the relationship between the stress and force in the shear plane ($F_s = \tau_s A_s$) and tool rake face ($N = \sigma_n A$), the shear stress in PSZ is expressed as

$$\tau_s = \sigma_n sin\phi_a n\cos(\phi_a - \alpha)[1 - \mu tan(\phi_a - \alpha)] \tag{3.2}$$

n is the ratio of tool chip contact length to uncut chip thickness, defined as $n = L_c/h_{un}$. When chip segmentation occurs, the chip material moves along the positive x-direction when the chip thickness increases to h_2, causing unloading on the tool rake face. As a result, the normal stress on the rake face (σ_n) decreases. From Eq. (3.2), the shear stress (τ_s) in PSZ also reduces based on the equilibrium condition. When new workpiece material enters PSZ, both the shear stress (τ_s) and normal stress (σ_n) increase, causing loading on the tool rake face. Therefore, the relationship between the variation of the shear stress and normal stress with respect to time is given by

$$\frac{d(\tau_s)}{dt} = \left[\frac{d(\sigma_n)}{dt} sin\phi_a n\right]\cos(\phi_a - \alpha)[1 - \mu tan(\phi_a - \alpha)] \tag{3.3}$$

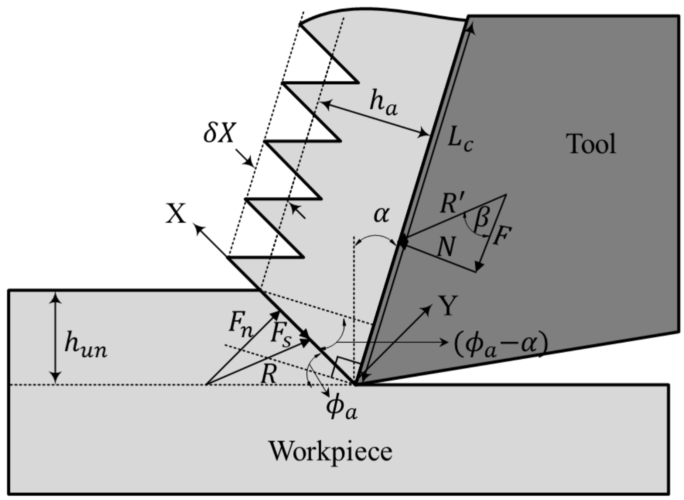

Figure 3.3 Kinematics of segmented chip formation.

For the chip material on the tool rake face, the change of normal stress is due to change of normal strain of the chip. Therefore, the normal stress-strain relationship is related to the material property, expressed as

$$\Delta\sigma_n = -(d\sigma/d\varepsilon)\Delta\varepsilon \tag{3.4}$$

where $d\sigma/d\varepsilon$ is the slope of normal stress to the normal strain determined by the material property. The change in normal strain $\Delta\varepsilon$ is due to the increase of chip thickness in chip segmentation, and $\Delta\varepsilon$ is in the direction perpendicular to the rake face. Therefore, the relationship between $\Delta\varepsilon$ and the chip displacement in the *x*-direction is expressed as

$$\Delta\varepsilon = \Delta X cos(\phi_a - \alpha)/h_a \tag{3.5}$$

ΔX is the displacement of workpiece material along the shear plane in addition to the average chip thickness due to chip segmentation. Assuming that the workpiece displacement ΔX occurs at the time interval of Δt, it is expressed by the shear velocity as

$$\Delta X = (V_L - V_s)\Delta t \tag{3.6}$$

For chip formation in the cutting process, the material's strain is generally in the range of 1-10 [70,71], and the strain with chip segmentation increases even further. Therefore, the infinitesimal strain assumption in characterizing the stress-strain relationship of the material can not be used. For large strain deformation, the change of σ with respect to ε ($d\sigma/d\varepsilon$ in Eq. (3.7)) is based on the large strain condition proposed by Rice [72], to characterize the loading-unloading on the tool rake face due to chip segmentation, expressed as

$$d\sigma/d\varepsilon = k = E(1+\upsilon)(D-\mu_m)^2/9(1-\upsilon) \tag{3.7}$$

where E is the young's modulus, υ is the Poisson's ratio, and D is the dilation parameter, which is the ratio of increment in free volume over the hard-sphere volume of STZ to the increment in normal strain [56,57]. Hence, from Eqs. (3.4) – (3.7), the change in normal stress for an infinitesimal time is given as

$$\frac{d\sigma_n}{dt} = -k(v_L - v_s)cos(\phi_a - \alpha)/h_a \tag{3.8}$$

Given the relationship between the shear velocity and the shear strain that $\dot{\gamma_s} = v_s/\Delta h$ and $\dot{\gamma_p} = v_L/\Delta h$, Eq. (3.8) is expressed by the shear strain rate as

$$\frac{d\sigma_n}{dt} = -msin(\phi_a)k(\dot{\gamma_p} - \dot{\gamma_s}) \tag{3.9}$$

where $m = \Delta h/h_{un}$ is the ratio between the thickness of PSZ to the uncut chip thickness. Therefore, from Eq. (3.9), the variation of shear stress τ_s is expressed as a function of shear strain rate as

$$\frac{d\tau_s}{dt} = mnksin^2\phi_a\cos(\phi_a - \alpha)\big(1 - \mu tan(\phi_a - \alpha)\big)(\dot{\gamma_s} - \dot{\gamma_p}) \tag{3.10}$$

From the kinematics of chip segmentation, it is concluded that the shear stress varies as a function of instantaneous shear strain rate $\dot{\gamma_p}$ of PSZ in segmented chip formation. It also should be noted that the shear strain rate is governed by the shear stress (τ_s), temperature (T) and free volume (ς), which is determined by the material constitutive property.

3.3 Material constitutive flow law of Zr-BMG

The mesoscale model based on sequential STZs transformations has been widely accepted as the fundamental mechanism for the plastic deformation of BMGs. The models have been validated using molecular dynamics simulations and FEA [59]. Johnson and Samwer [73] proposed a new mesoscale cooperative shear model (CSM) to predict the temperature and stress-dependent inelastic behaviour of metallic glasses. In the model, the macroscopic deformation is assumed to result from a cluster of local shear transformations. The model is based on the potential energy and inherent states developed by Stillinger [74] and Wales [75]. Each STZ has different potential energies depending on various atomic configurations. The atomic configurations of the potential energy landscapes can be divided into basins (states with local minima, which are stable), saddle points (acts as the separation point between local minimums), and peaks (states with local maxima) in multi-dimensional space. Based on the topological position of STZ, the barrier energy required to activate the inelastic flow can be estimated.

The plastic deformation occurs when the applied stress reduces the potential energy barrier close to zero. The macroscopic yielding occurs globally when a critical fraction of unstable STZs is activated. The CSM model correlates material flow strain rate, yield strength, applied stress, and temperature. The CSM is widely accepted to describe the plasticity of BMG materials [76,77]. The model is validated experimentally over a wide range of strain rates and temperatures for various BMG materials [77]. According to the CSM model, the material flow rate in BMGs is given by [73]

$$\dot{\gamma}_{stz} = \gamma_e exp\left(-\frac{W(\tau_s)}{K_b T}\right) \tag{3.11}$$

where K_b is Boltzmann constant, γ_e is a pre-exponential factor, T is the temperature of the material. $W(\tau_s)$ is the barrier energy required to initiate shear transformation, given by

$$W(\tau_s) = C_s \gamma_c \tau_c \Omega_s (1 - \tau_s/\tau_c)^{3/2} \tag{3.12}$$

where $\tau_c = \gamma_c G$ is the critical shear resistance of the material at 0 K, determined by the shear modulus G and the yield strain γ_c at 0 K. Ω_s is the volume of the STZs, C_s is the correction factor, and τ_s is the applied shear stress. Strictly speaking, the activation energy weekly depends on the temperature, in order to simplify the analysis, the dependence of temperature is neglected.

Most of the analyses related to the plasticity of metallic glasses are based on elevated temperatures in tension, compression, and bending. However, in the machining of BMGs, segmented chip formation occurs at low cutting speeds, and the temperature generated is lower than the glass transition temperature. At this condition, the free volume diffusion rate is stress-driven. In all the BMG deformations theories, it is generally accepted that the free volume plays a crucial role as a carrier for plasticity in metallic glasses. It is assumed that when the BMGs are subjected to external stress in machining, it initiates an STZ at the location of maximum free volume. As the stress increases, multiple STZs originate around the neighbourhood of primary STZ due to free volume availability. When the stress increases further, a series of STZs occur, resulting in shear band nucleation. When the stress reaches above a critical value, shear band propagation occurs, resulting in shear localization as the macroscopic plastic behaviour. Free volume generation depends on the atomic rearrangements that occur during deformation due to applied stress and temperature. Huang et al. [78] presented that for an isothermal deformation process in BMGs, the imbalance between the generation and diffusion of the free volume is the primary source of inhomogeneous deformation. However, clear conclusions on the effect of thermal softening, which is the imbalance between generation and dissipation of temperature in the PSZ of machining are not reported. Therefore, to determine the material deformation in the machining of BMGs, the free volume generation and heat generation resulting from the tool-workpiece interaction have to be considered. An activation factor related to free volume is included in the constitutive Eq. (3.12) following [79-81]. The activation factor for free volume is expressed as $\exp(-1/\zeta)$, Therefore, the constitutive equation of Zr-BMG characterizes the shear strain rate as a function of the shear stress, temperature, and free volume of the material in the PSZ is presented as

$$\dot{\gamma_p} = \gamma_v \exp\left(-\frac{1}{\zeta}\right) exp\left(-\frac{W(\tau_s)}{K_b T}\right) \tag{3.13}$$

where $\zeta = v_F/v^*$, v_F is the free volume available per STZ in the PDZ, and v^* is the critical volume of STZ beyond which free volume formation occurs, and γ_v is vibration period of STZ. The generation and diffusion of the free volume following Huang et al. [78] and Jiang et al. [62] is given by

$$\frac{d\varsigma}{dt} = F(\tau_s, T, \zeta) + \xi(\zeta_o - \zeta) \tag{3.14}$$

where ζ_o is the assumed initial free volume and $F(\tau_s, T, \zeta)$ represents the generation and annihilation of the free volume. Eq. (3.14) is a summation of generation and diffusion of free volume per unit time. The generation of the free volume is influenced by the state of stress, temperature and free volume state, given by [81]

$$F(\tau_s, T, \zeta) = \exp\left(\frac{-1}{\zeta}\right) exp\left(\frac{-W(\tau_s)}{K_b T}\right)\frac{2KT}{\zeta S}\left[cosh\left(\frac{\tau_s \gamma_o \Omega_s}{2K_b T}\right) - 1\right] \quad (3.15)$$

where S is a stiffness parameter given by $S = 2G(1+\upsilon)/3(1-\upsilon)$, γ_o is the critical shear strain required to activate an STZ, ξ is the coefficient for free volume diffusion of the material, given as $\xi = (V_n + 4D_f/\Delta h)/\Delta h$, where D_f is diffusivity coefficient. To be precise, the material parameters, such as diffusivity and shear modulus weekly depend on the temperature, in order to simplify the analysis, the dependence of temperature is neglected.

3.4 Heat generation and dissipation

The plastic deformation of the material in PSZ increases the temperature and free volume density. At the same time, the temperature is influenced by heat dissipation, including conduction and advection. The variation of temperature in the PSZ is modelled by one-dimensional heat transfer equation, expressed as [82]

$$\frac{dT}{dt} = q_{Tq}\tau_s\dot{\gamma_p} + \chi(T_0 - T) \quad (3.16)$$

where q_{Tq} = $\beta_{tq}/\rho C_v$. β_{tq} represents the portion of plastic deformation energy converted to heat. C_v is the specific heat. $\chi = (V_n + 4k_d/\Delta h)/\Delta h$ is the coefficient for temperature due to heat dissipation. k_d is the thermal diffusivity and ρ is the density of the material. T is the temperature of the material in the PSZ, and T_0 is the initial temperature, which is assumed to be the room temperature. The material parameters, such as thermal conductivity and specific heat weekly depend on the temperature in BMGs, in order to simplify the analysis, the dependence of temperature is neglected.

3.5 Solution of the governing equations

The governing equations for modelling the variations of shear stress, shear strain rate, temperature, and free volume of the materials in PSZ are given by the coupled Eqs. (3.13), (3.14), (3.15) and (3.16). The input cutting parameters, including measured and assumed cutting parameters as well as input material parameters used to simulate the chip segmentation phenomenon are presented in Section 3.6.2. One critical material parameter which drives the deformation by the shear transformation in metallic glasses is the volume of STZs (Ω_s). Initially, the assessment of volume of STZs was conducted using molecular dynamics simulations. Later on, Pan et al. [83] revealed that the volume of STZs depends on the applied stress and strain rate, and the activation volume of STZs based on strain rate sensitivity is calibrated from nano-indentation experiments conducted at various strain rates. It is concluded that Ω_s is sensitive to the process conditions, and the volume of STZ is given by

$$\Omega_{stz} = \frac{2K_b T_r \tau_c}{3m_s G \gamma_c^2 C_s \tau_a \left[1 - \frac{\tau_a}{\tau_c}\right]^{0.5}} \tag{3.17}$$

where m_s is the strain rate sensitivity defined by $m_s = \partial \ln \tau / \partial \ln \dot{\gamma}_s$, T_r is the room temperature, and τ_a is the average shear stress in the deformation zone. In this study, the STZ volume is calibrated from orthogonal cutting experiments using the average shear stress calculated from the measured average cutting force.

To better analyze the dynamics of the chip formation process, dimensionless parameters are introduced in the governing equations, defined as temperature $\hat{T} = T/T_o$, shear stress $\hat{\tau} = \frac{\tau}{\tau_o}$, $\zeta = \hat{\zeta}$ (as the ζ is a dimensionless parameter), where $\tau_o = 2K_b T_o/\gamma_o \Omega_{stz}$ and $\hat{t} = t/t_o$ with $t_o = e^N/\gamma_v$ and $N = C_s \gamma_c \tau_c \Omega_{stz}/K_b T_o$. The governing equations in dimensionless form are

$$\frac{d\hat{\tau}}{d\hat{t}} = A\left(\hat{\dot{\gamma}}_s - \hat{\dot{\gamma}}_p\right) \tag{3.18}$$

$$\hat{\dot{\gamma}}_p = exp\left(N\left\{1 - \frac{(1 - P\hat{\tau})^{1.5}}{\hat{T}}\right\} - \frac{1}{\hat{\zeta}}\right) \tag{3.19}$$

$$\frac{d(\hat{\zeta})}{d(\hat{t})} = \hat{\xi}\left(\zeta_o - \hat{\zeta}\right) + \hat{\dot{\gamma}}_p\left\{\frac{\hat{T}}{\hat{\zeta}\Psi}\left[cosh\left(\frac{\hat{\tau}}{\hat{T}}\right) - 1\right]\right\} \tag{3.20}$$

$$\frac{d\hat{T}}{d\hat{t}} = \hat{\chi}\left(1 - \hat{T}\right) + Q\tau\hat{\dot{\gamma}}_p \tag{3.21}$$

where $A = mnk\Theta/\tau_o$, $\Theta = sin^2\phi_a(1 - \mu\tan(\phi_a - \alpha))$, $\hat{\dot{\gamma}}_p$ is the dimensionless activation shear strain rate, $P = \tau_o/\tau_c$ is a constant, dimensionless shear strain rate $\hat{\dot{\gamma}}_s = \dot{\gamma}_s t_o$, $\hat{\xi} = (V_n + 4D_f/\Delta h)t_o/\Delta h$, $\Psi = v^* S/\tau_o \Omega_{stz}$, $\hat{\chi} = (V_n + 4k_d/\Delta h)t_o/\Delta h$ and $Q = q_{Tq}\tau_o/T_o$.

To improve the understanding, the caps ('∧') of the dimensionless parameters are not presented in further analysis. The governing equations of shear deformation inside the PSZ are coupled nonlinear differential equations. In order to study the influence of the free volume softening compared to the thermal softening in machining BMGs, the critical parameter resulting in periodic solution should be identified. In this study, linearization of the governing equations and numerical method were used to identify the bifurcation phenomenon where the solution is periodic. The linearization of the governing equations is performed at the equilibrium point of (τ_e, T_e, ζ_e), where the change of shear stress, free volume and temperature is equal to zero. The approximate linearization point is (τ_e, T_e, ζ_e) is derived as

$$\tau_e \approx \frac{1}{P}\left(1 - \left(1 - \frac{\zeta_e \ln \dot{\gamma}_s + 1}{N\zeta_e}\right)^{2/3}\right) \tag{3.22}$$

$$T_e \approx 1 + \frac{Q\tau_e\dot{\gamma}_s}{\chi} \tag{3.23}$$

$$\zeta_e \approx \frac{\zeta_o}{2} + \left[\left(\frac{\zeta_o}{2}\right)^2 + \frac{\dot{\gamma}_s \exp(\frac{2}{3p})}{2\xi\Psi}\right]^{0.5} \tag{3.24}$$

The procedure in deriving the linearization point is provided in Appendix 1. Using linear stability analysis, the Jacobian matrix of the governing equations at the homogenous solution is calculated as

$$J = \begin{bmatrix} \dot{\tau}_\tau & \dot{\tau}_\zeta & \dot{\tau}_T \\ \dot{\zeta}_\tau & \dot{\zeta}_\zeta & \dot{\zeta}_T \\ \dot{T}_\tau & \dot{T}_\zeta & \dot{T}_T \end{bmatrix}$$

where $\dot{\tau}_\tau$ represents the partial derivate of the Eq. (3.18) with respect to the shear stress τ. Similarly, Eqs. (3.19), (3.20) and (3.21) and their partial derivatives with respect to shear stress, free volume and temperature are identified at the equilibrium condition. The system has bifurcation or limit cycle instability if and only if the trace is equal to zero, and the determinant is greater than zero. That is, the sum of Eigenvalues of the Jacobean matrix is equal to zero, and their product is greater than zero. Therefore, the conditions to obtain the periodic solution are

$$(\dot{\tau}_\tau + \dot{\zeta}_\zeta + \dot{T}_T)_{\tau_e,\zeta_e,T_e} = 0 \text{ and } (\det[J])_{\tau_e,\zeta_e,T_e} > 0 \tag{3.25}$$

From the conditions above, an approximate analytical solution of the critical parameter which results in a periodic solution is given by

$$\xi_{cr} = \dot{\gamma}_s \left[\frac{(1-\zeta_e)}{2\Psi{\zeta_e}^3}(exp\tau_e) - 3A \cdot N \cdot P\sqrt{(1-P\tau_e)} \right] - \chi \qquad (3.26)$$

It is observed that the process stability is influenced by both the temperature diffusion coefficient χ and the free volume diffusion coefficient ξ. For an identified coefficient of temperature χ, the instability occurs based on the condition presented in Eq. (3.25), and the critical diffusion coefficient of free volume ξ_{cr} is calculated from (3.26). It should be noted that the expression of the critical value of ξ is based on the approximation of linearization around the equilibrium point. The accuracy of the solution (3.26) is analyzed through the numerical method. The flow chart to identify the critical parameter resulting periodic solution using numerical method is shown in Figure 3.4. The comparison of the numerically identified ξ_{cr} and analytical solution using equation (3.26) is presented in Figure 3.5 for a range of cutting speeds. It is found that the difference between the solutions is within 12%. After the identification of ξ_{cr} which results in a periodic solution, the oscillations in shear stress (τ), free volume (ζ) and temperature (T) can be predicted.

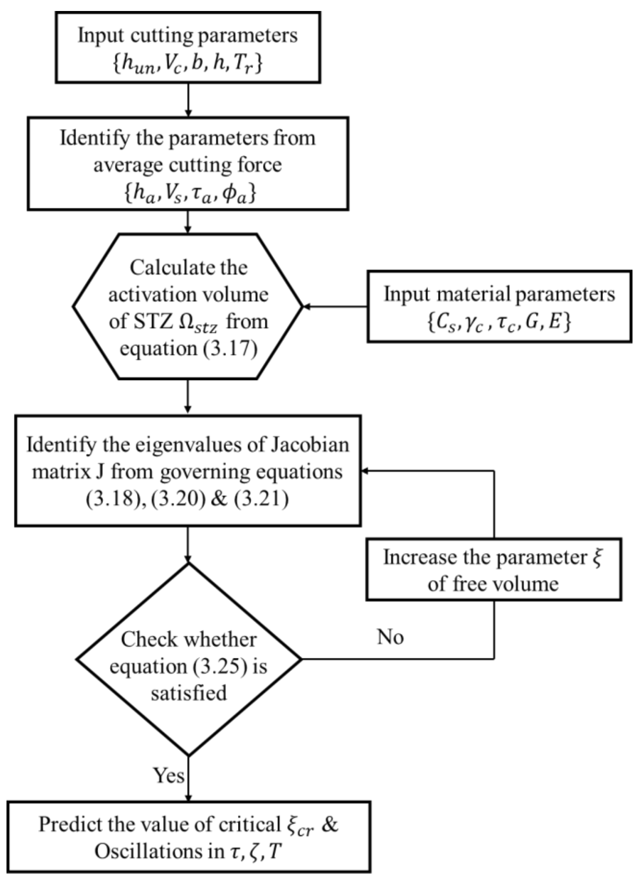

Figure 3.4 Numerical method to identify the stability of system.

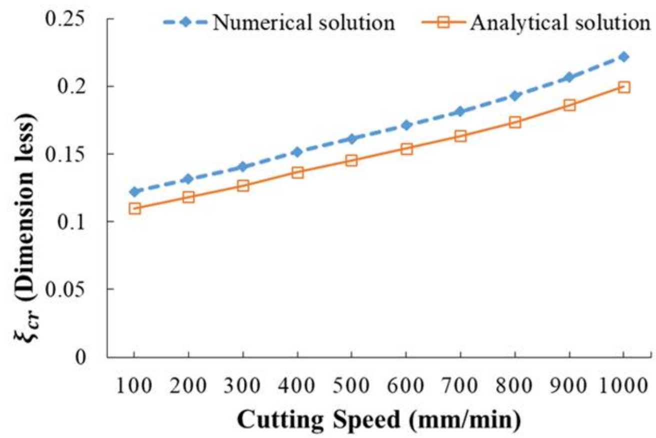

Figure 3.5 Comparison of critical free volume parameter value through approximate analytical solution based on linearization and numerical method.

3.6 Simulations and experimental results

In this Section, orthogonal machining experiments on Zr-BMG are performed. The activation volume of Zr-BMG is calibrated by measuring the average cutting force. The model simulates the frequency of the chip segmentation based on the cutting condition, and the simulation results are compared with the experimental results at different cutting speeds and uncut chip thickness values. The mechanisms of the stress oscillations and the chip segmentation are further discussed.

3.6.1 Experimental setup and procedure

Orthogonal cutting experiments were carried on a 3-axis precision machining center (Mikrotools-DT110). An uncoated carbide tool with zero rake angle was used to cut Zr- BMG workpiece (VIT 105). The glass transition temperature (T_g) is 673 K, and the crystallization temperature (T_x) is 743 K. The schematic of the experimental setup is shown in Figure 3.6. The cutting length is approximately 30 mm, and conditions are presented in Table 3.1. Hitachi SU 3500 Scanning electron microscope (SEM) was used to measure the segmentation length of the machined chip.

Figure 3.6 Schematic representation of experimental setup.

Table 3.1 Experimental conditions.

Process Parameters		**Cutting Tool Property**	
Cutting speed	100-1000 mm/min	Tool material	Carbide
Uncut chip thickness	20-50 μm	Rake angle	0°
Width of cut	2 mm	Clearance angle	7°

Orthogonal cutting experiments were conducted to identify the minimum activation volume and other process parameters used for the simulations. It should be noted that only average cutting forces and average chip thickness are used to identify the material-related constants, including the shear angle, friction angle, and the activation volume of the material. The information used in the identification is different from the instantaneous output results of the model, such as the frequency and amplitude of the time-varying shear stress, strain rate and temperature, which are used to characterize the chip segmentation. The average cutting forces were measured with respect to uncut chip thickness from 20 μm to 50 μm at 10 μm intervals, shown in Figure 3.7. The average chip thickness was measured under the same cutting condition, and the shear angle was calibrated by the average chip thickness ratio based on $\phi_a = tan^{-1}((h_a/h_{un} - sin\alpha)/cos\alpha)$, with the result of $27°$. The slopes of fitted lines in Figure 3.7 represent the cutting force coefficients in tangential (K_{tc}) and thrust (K_{fc}) directions. The friction angle is calculated as $\beta = \alpha + tan^{-1}\left(K_{fc}/K_{tc}\right) = 30^{\circ}$, then the coefficient of friction is $\mu = \tan\beta$=0.577. The average shear stress τ_a was identified from the cutting force coefficients given by $\tau_a = K_{tc} sin\phi_a \cos(\phi_a + \beta - \alpha)/b\cos(\beta - \alpha)$, with the result of 540 MPa. Cutting experiments were also conducted at various cutting speeds, and the sensitivity of the shear stress with respect to the shear strain rate ($\ln\tau - \ln\dot{\gamma_s}$) is obtained and shown in Figure 3.8. Then the strain rate sensitivity $\partial \ln\tau / \partial \ln\dot{\gamma_p}$ represents the slope of the fitted line as m_s=0.092. Other parameters for the identification of the activation volume are material constants of Zr-BMG, given as E = 92.7 GPa, G =33.5 GPa, υ =0.38, $\tau_c = \gamma_c G$, $\gamma_c = 0.03, T_r = 300\ K$, K_b=1.3810^{-23} J/K. Therefore, the activation volume Ω_{stz} is evaluated from Eq. (3.17), with the result of 6.48×10^{-28} m^3.

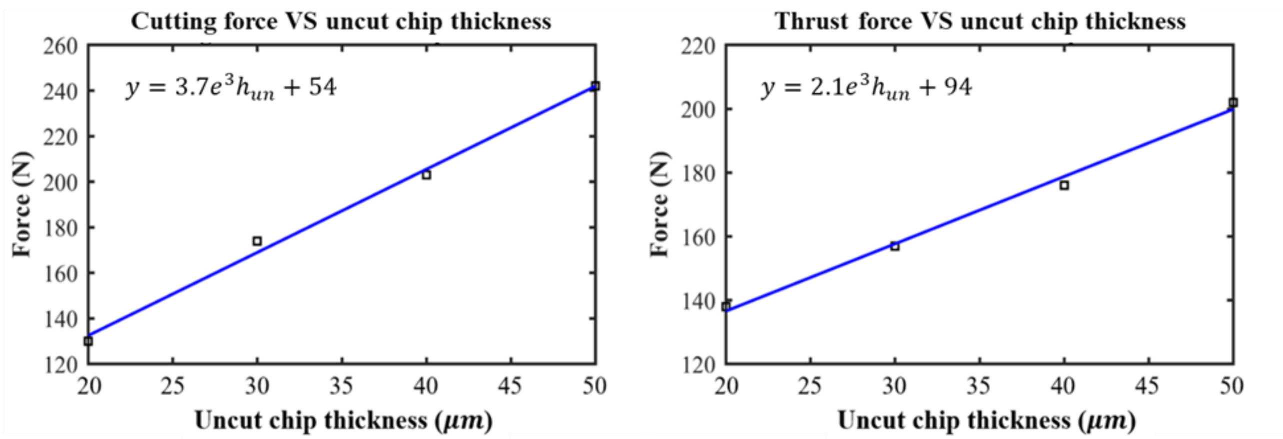

Figure 3.7 Variation of cutting force and thrust force with respect to uncut chip thickness.

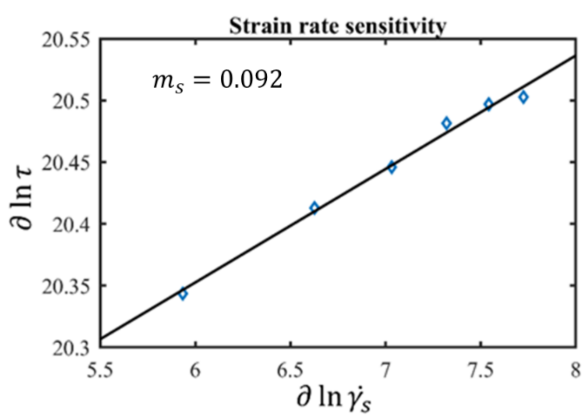

Figure 3.8 Strain rate sensitivity in orthogonal cutting of Zr-BMG.

The oscillations of shear stress, temperature, and free volume associated with the chip segmentation are simulated from the developed model. The cutting conditions, the material properties of Zr-BMG, and the identified parameters used in the simulations are listed in Table

3.2. It is assumed that the thickness of the PSZ is 0.15 of the average shear plane length, and the ratio between the tool-chip contact length and the uncut chip thickness is 2, which were also assumed in general orthogonal cutting simulations [84].

Table 3.2 Cutting conditions and material parameters in the simulation.

Cutting condition	Uncut chip thickness - μm	30, 40, 50
	Cutting speeds – mm/min	100, 400, 700, 1000
Mechanical properties of Zr-BMG	Density (ρ) - kg/m^3 [18]	6570
	Poisson's ratio υ [18]	0.38
	Specific heat (C_v) - J/kg/K [18]	380
	Thermal diffusivity (k_d) - m^2/s [18]	2×10^{-6}
	Diffusion coefficient (D_f) - m^2/s [62]	10^{-16}
	Pre-exponential factor (γ_v) - Hz [62]	10^{13}
	Critical shear strain (γ_o) [59]	0.1
	Initial free volume (ζ_o) [62]	0.05
Identified material property	Activation volume (Ω_{stz}) – m^3	6.48×10^{-28}
Parameters influenced by Cutting Condition	$m = \Delta h / h_{un}$ [84]	0.3
	$n = L_c / h_{un}$ [84]	2
Constants used for dimensionless analysis	T_o - K	300
	t_o - s	2×10^{-5}
	τ_o - MPa	140

Figure 3.9 shows the simulation results when the cutting speeds range from 100 mm/min to 1000 mm/min at 50 μm uncut cut chip thickness. The oscillations of shear stress τ_s, temperature T and free volume ζ with respect to time are predicted. The results explain the mechanism of the cutting process of Zr-BMG. When the material enters the PSZ, the shear stress gradually increases, while the temperature and free volume do not change significantly. When the shear stress is above a critical value, the temperature and free volume increase rapidly, due to the fact that softening effect is more dominant compared to the dissipation. The shear stress decreases as a result, and

increases again when new material enters the PSZ, resulting in the stress oscillations. It was found that the oscillation frequency decreases from 323 Hz at 1000 mm/min to 48 Hz at 100 mm/min cutting speed. Based on the simulated frequencies at the four cutting conditions, it was found that the oscillation frequency is proportional to the cutting speed. The maximum shear stress at 1000 mm/min is 658 MPa and decreases to 540 MPa at 100 mm/min, which shows the strain-rate effect. The maximum temperature at 1000 mm/min is 480 K and decreases to 330 K at 100 mm/min, because there is more heat dissipation at lower cutting speed.

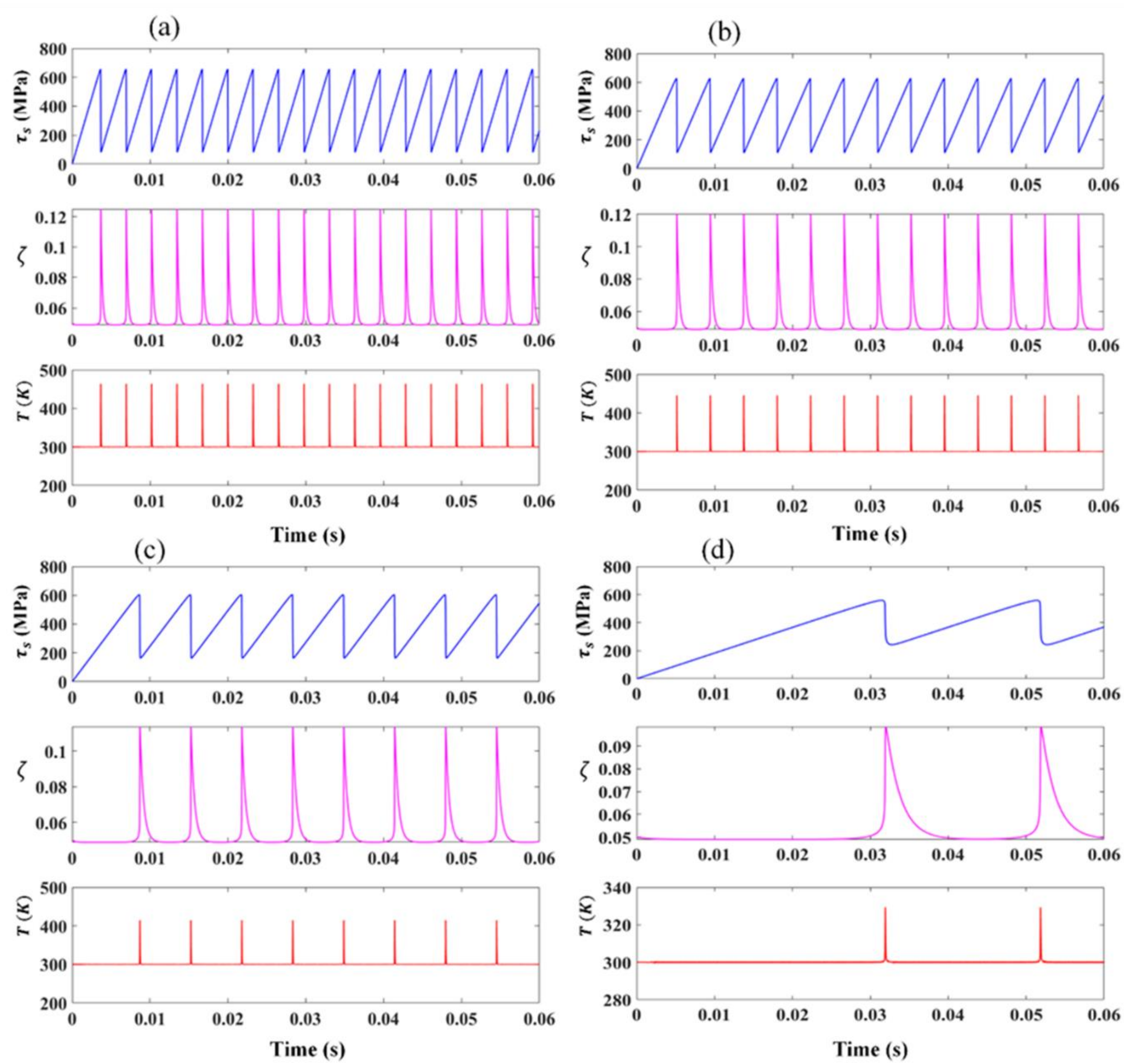

Figure 3.9 The predicted shear stress (τ_s), free volume (ζ) and temperature (T) with respect to cutting time for cutting speeds (a) 1000 mm/min, (b) 700 mm/min, (c) 400 mm/min, and (d) 100 mm/min at 50 μm uncut chip thickness.

The simulation results for varying uncut chip thicknesses from 30 μm to 50 μm at 100 mm/min cutting speed are presented in Figure 3.10. It was observed that the maximum shear stress does not vary significantly with uncut chip thickness (538 MPa at 30 μm and 540 MPa at 50 μm). Similarly, there is no significant change in temperature with uncut chip thickness. The maximum temperature is 330 K at 30 μm, and 340 K at 50 μm. There is an increase in oscillation frequency with the decrease of uncut chip thickness, with 60 Hz at 30 μm uncut chip thickness, and 48 Hz at 50 μm uncut chip thickness. The segmentation spacing is proportional to the uncut chip thickness. Therefore, the decrease of uncut chip thickness results in the increase of oscillation frequency at the same cutting speed. The average shear stress predicted from the simulation is compared with the calculated stress value from the experimentally measured cutting force at different cutting speeds. It was found that the simulated increase of shear stress is 118 MPa when the cutting speed increases from 100 mm/min to 1000 mm/min due to the strain rate effect, and the increase of shear stress from the experiment is 150 MPa.

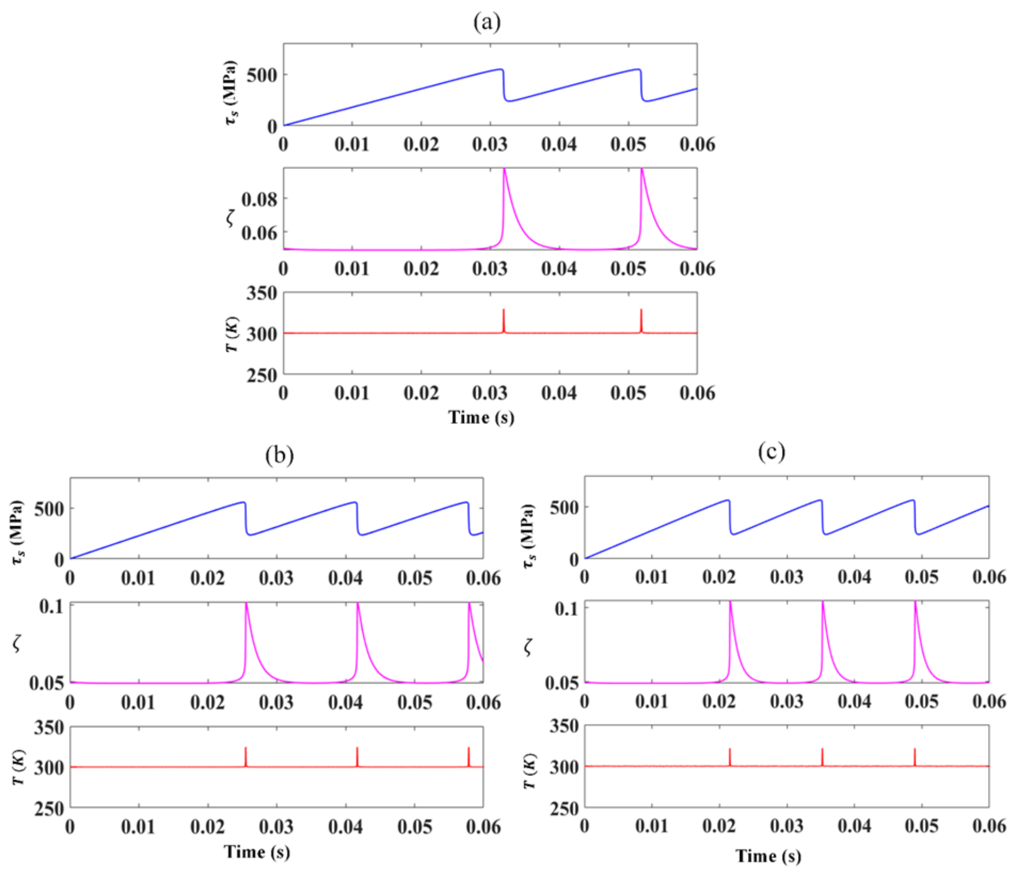

Figure 3.10 The predicted shear stress (τ_s), free volume (ζ) and temperature (T) with cutting time for uncut chip thickness (a) 50 µm, (b) 40 µm, and (c) 30 µm at 100 mm/min.

The predicted frequencies of the shear stress resulting in the chip segmentation are compared with the segmentation frequency obtained by measuring the chip morphology using SEM. Figures 3.11 and 3.12 show the machined chips' SEM images at the same cutting conditions with the simulations at varying cutting speeds and uncut chip thicknesses, respectively. The length of five segments are measured, and the average pitch length ($L_p \cos(\phi_a - \alpha)$) of the segments is calculated, in which L_p is the average pitch length along the rake face. The chip segmentation frequency is calculated by the material speed (V_n) and the projected pitch length along the chip flow direction, calculated as $f_s = V_n / L_p \cos(\phi_a - \alpha)$. Table 3.3 shows the comparison of the chip segmentation frequencies from the simulations and the experimental measurements at different cutting speeds and uncut chip thickness values. In the measurement, for each cutting condition, the chip segmentation spacing is measured at five locations along the entire length of the chip. The length values shown in Figures 3.11 and 3.12 represent one of the five measurements. The calculated segmentation frequencies from the average values and the variations of the spacing measurement are given in Table 3.3. It was found that the difference between the predicted chip segmentation frequencies from the simulations and the experimental results is in the range of 15%-30%. The difference may be due to the assumptions of the PSZ thickness and the ratio between the tool-chip contact length and the uncut chip thickness. Furthermore, the thermal diffusivity and the specific heat may vary with temperature, but are assumed constants to simplify the model.

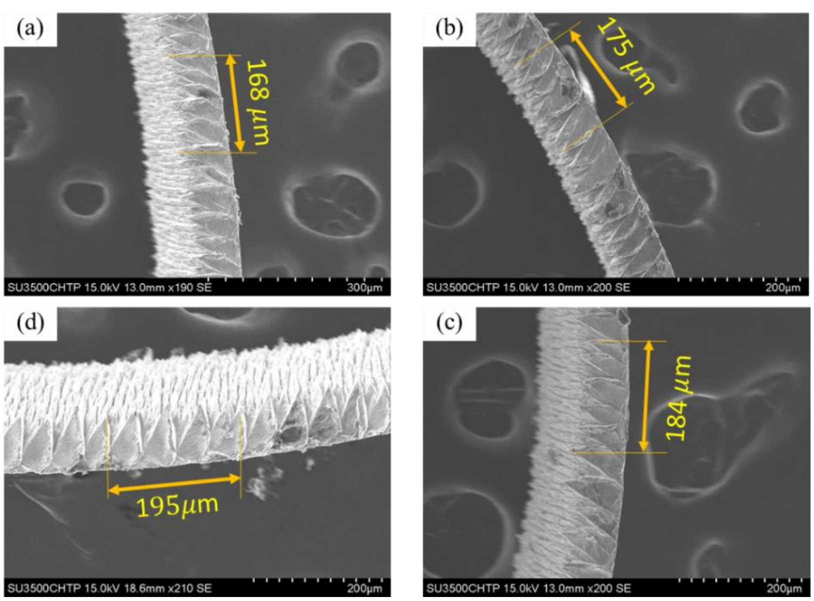

Figure 3.11 Segmented chip formation at 50 μm uncut chip thickness: (a) 100 mm/min (b) 400 mm/min (c) 700 mm/min, and (d) 1000 mm/min.

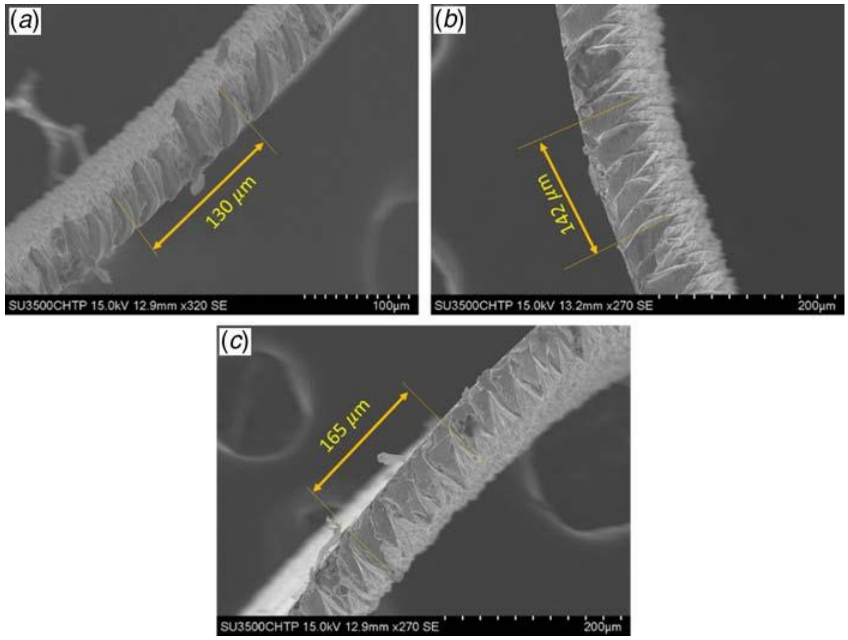

Figure 3.12 Segmented chip formation at uncut chip thickness (a) 30 μm, (b) 40 μm, and (c) 50 μm at 100 mm/min.

Table 3.3 Comparison of chip segmentation frequencies.

Cutting condition		**Frequency from simulations (Hz)**	**Frequency from experiments (Hz)**
Uncut chip thickness (μm)	Cutting speed (mm/min)		
50	100	48	34±6
	400	140	120±10
	700	234	204±12
	1000	323	283±15
Cutting speed (mm/min)	Uncut chip thickness (μm)		
100	30	60	45±5
	40	54	38±5
	50	48	34±6

3.6.2 Analyses of the model

In modelling the kinematics of chip formation described in Section 3.2, the inertial force of the machined chip is included in [50], and the inertial force (F_i) is expressed as

$$F_i = \rho h_{un} b V_c^2 cos\alpha / \cos(\phi_a - \alpha) \quad (3.27)$$

However, based on the given cutting conditions shown in Table 3.2, the inertia force's simulated value is smaller than 2% compared to the shear force in PSZ. Therefore, in this model, the inertial force of the machined chip is neglected without losing the accuracy of the predicted results.

From the simulation results, it was observed that the shear stress oscillation associated with the chip segmentation is a result of both free volume and thermal instability. In order to evaluate which effect plays a more dominant role in the process instability, the free volume and temperature with respect to time at the increasing period are shown in Figure 3.13. To make the two parameters comparable, only dimensionless values are presented to show the rate at which the parameters change (instability index) with respect to the dimensionless time. It was observed that the increase in free volume occurs earlier than the increase in temperature. When the dimensionless free volume increases by 20%, the change of temperature is still negligible. At later stage, when the free volume increases above a critical value, it triggers a rapid increase in temperature. Therefore, it is concluded that the instability of the system is initiated mainly by free volume compared to temperature. However, it was observed that the temperature diffusion has a significant effect on the frequency of segmentation and amplitude of the shear stress. To understand the effect of temperature diffusion, the shear stress and free volume are simulated with and without the temperature effect, as shown in Figure 3.14. The cutting speed is 1000 mm/min, and the uncut chip thickness is 50 µm. When the temperature is assumed constant, the difference between the predicted frequency of segmentation and experimental results becomes 70%, which shows a large discrepancy. The amplitude of the shear stress is 20% lower compared to the results including the thermal effect. Therefore, even though chip segmentation initiates from free volume instability, temperature plays a significant role in determining the segmented chip formation frequency and amplitude.

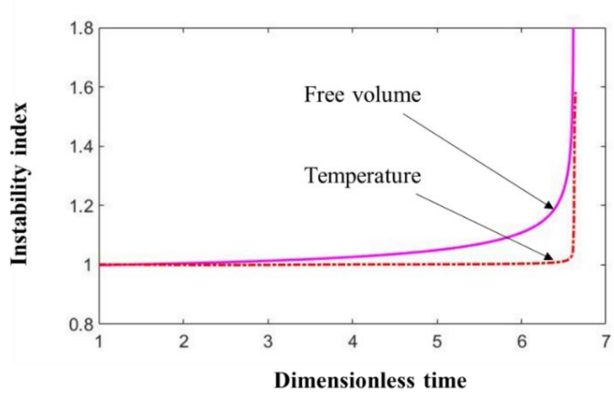

Figure 3.13 Instability index of dimensionless free volume and temperature with dimensionless time.

Measurement of the instantaneous variations of temperature in PSZ is challenging due to the small area of the deformation zone and high-frequency oscillations. There is no experimental result available in the literature for the temperature in cutting Zr-BMG. The predicted maximum localized temperature in the shear band at 1000 mm/min cutting speed and 50 μm uncut chip thickness is 480 K, which is less than the glass transition temperature (Tg) of Zr-BMG. Therefore, it is expected that the chip remains in the amorphous phase. X-ray diffraction (XRD) analysis is conducted for the original BMG material and the machined chip, with the results shown in Figure 3.15. No crystallization peaks were observed from the XRD spectra, so it is demonstrated that no crystallization occurs in the chip formation for the cutting conditions included in this chapter.

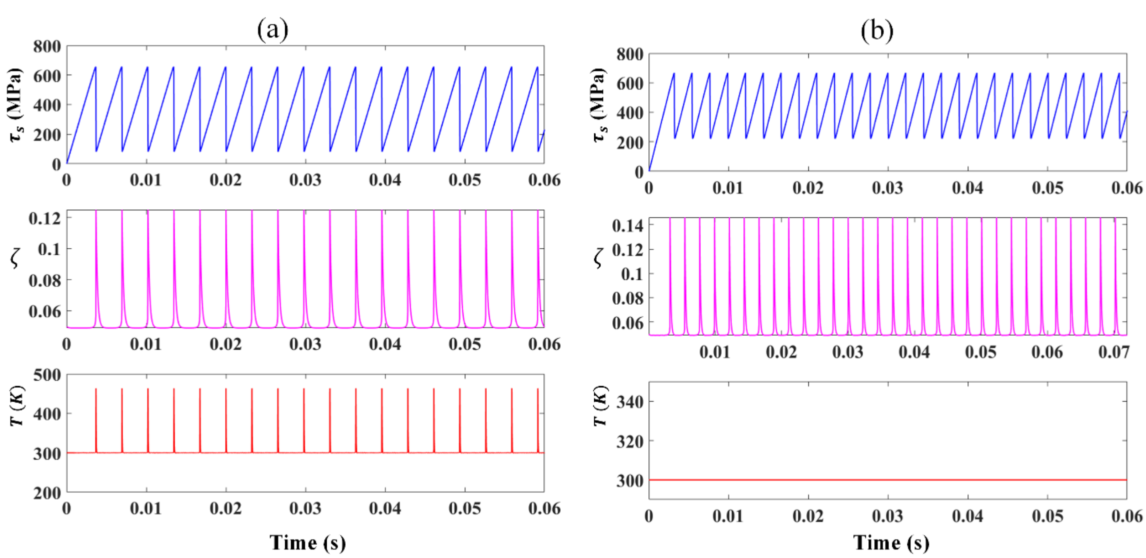

Figure 3.14 Variation of shear stress (τ_s), free volume (ζ) and temperature (T): (a) including the thermal effect, and (b) assume constant temperature.

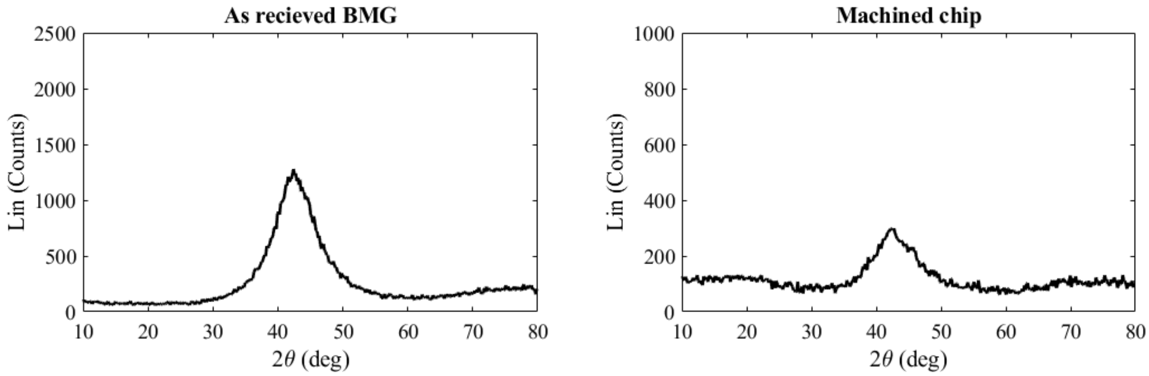

Figure 3.15 Comparison of XRD spectrums of the as-received BMG and machined chip at 1000mm/min cutting speed and 50 μm uncut chip thickness.

Lewandowski et al. [63] and Wright et al. [85] conducted bending and compression tests on BMG material, respectively. The measured average increase of temperature is around 200 K in the shear bands, demonstrating the importance of temperature in shear flow instability. Bruck et al. [86] estimated the temperature rise of 500 K in the dynamic compression test of Zr-BMG at a strain rate of 10^3 s^{-1}. Zhao et al. [87] developed a finite element model considering material flow law, free volume and heat generation in the shear band to predict the localized temperature rise. The estimated temperature rise in Zr-BMG at a strain rate of 10^3 s^{-1} is around 420 K. The strain rate of the material is comparable with the value in orthogonal cutting in this study, in which the maximum cutting speed is 1000 mm/min. In addition, the temperature rise in the shear band based on Fick's law of thin-film heat generation and diffusion as proposed by Lewandowski et al. [63] is compared with the predicted temperature in the current study. The temperature rise in the shear band is estimated based on [59] is given by

$$\Delta T = \frac{H}{2\rho C_v \sqrt{\pi k_d}} \frac{1}{\sqrt{t}} \exp\left(\frac{-x^2}{4k_d t}\right) \tag{3.28}$$

where x is the spatial distance from the center of the shear band, t is the time of shear band formation, and H is the heat generated per unit area. For the cutting speed of 1000 mm/min in orthogonal cutting, the shear band spacing is 10 nm, and the time for shear band formation t is calculated as 1.35 μs. The heat capacity is estimated by work done by shear stress in generating shear displacement, expressed as $H = \varphi \tau_a \delta$, where φ is a dimensionless constant estimated as 0.3±0.05 [88]. The shear displacement of the chip from SEM observation is 18 μm, which gives the value of H=3240 J/m^2. The estimated rise in temperature (ΔT) using Eq. (3.28) for a distance of 1 μm from the center of the shear band is 198 K, which is close to the predicted value of 180 K. Therefore, the predicted temperature is close to the estimated result in the literature with comparable strain and strain rate. However, it should be noted that the predicted temperature is localized in the shear band, while global temperature rise during deformation in BMGs is approximately 2-3 K, as reported by Yang et al. [89]. Furthermore, the predicted maximum stress is compared with the stress values calculated from the measured cutting force in the experiment at different cutting speeds at 50 μm uncut chip thickness, shown in Figure 3.16. Since the stress is a function of the strain rate, temperature, and free volume, it is demonstrated that the predicted temperature and free volume are reasonable based on the literature and experimental results. The proposed model demonstrates the effect of temperature on the shear instability in the orthogonal cutting of Zr-BMG, associated with the chip segmentation.

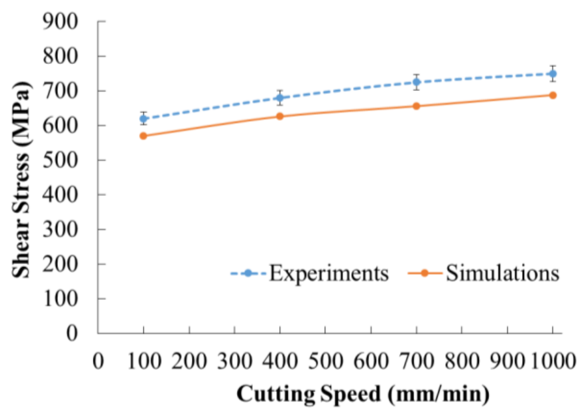

Figure 3.16 Comparison of shear stresses for various cutting speeds at 50 μm uncut chip thickness.

3.7 Conclusions

In this chapter, a new physics-based model is developed to investigate the fundamental mechanism of segmented chip formation in orthogonal cutting of Zr-BMG. The shear stress variation in the primary shear zone is modelled considering the large-strain deformation of the workpiece material. The material flow law is modelled through cooperative shear from STZs considering the inhomogeneous deformation that occurs below the glass transition temperature to characterize the strain rate. The activation volume of the Zr-BMG material is dependent on the cutting condition, and plays a significant role in determining the variation of the shear stress. The oscillations of the shear stress, temperature, and free volume are predicted based on the cutting conditions, and the oscillation frequencies are compared with the measured chip segmentations from orthogonal cutting experiments.

The simulation results show that the shear flow instability in cutting Zr-BMG is governed by the combined effects of both temperature and free volume, which result in inhomogeneous deformation. The shear stress oscillations in the primary shear zone are initiated by the increase of free volume. The temperature in the PSZ plays a significant role in the estimation of the frequency of chip segmentation. Based on the cutting conditions in this research, the temperature rise is below the crystallization temperature of Zr-BMG, therefore, the machined chip remains in an amorphous state. The developed model determines the mechanism of chip segmentation in cutting of Zr-BMG, and the results can provide guidance in chip formation control and process planning for improving the cutting efficiency.

Chapter 4

Mechanics Model of Vibration Assisted Machining of Zr-BMG

4.1 Overview

The machining of BMG results in rapid tool wear due to the high strength of the material [23,65]. Although VAM has shown advantages of achieving better surface quality and improving tool life in machining crystalline metal alloys and composites [21, 22], no report has been found on how vibration assistance influences the cutting mechanics of BMGs. As explained in Section 2.4, the periodic contact between the tool and the workpiece influences the stress and temperature variations in the deformation zones. The change of strain rate, stress, and temperature influences the deformation mechanism of BMG in the cutting process. In this study, a physics-based model is developed to analyze the effect of 2-D vibration on the deformation mechanism in orthogonal cutting of Zr-BMG. The process kinematics of VAM, the chip segmentation, and the stress and temperature variations are predicted based on the proposed model.

The organization of this chapter is presented in the flow chart shown in Figure 4.1. A kinematic model of tool trajectory is necessary to develop the mechanics model of EVAM to predict shear angle and cutting forces. Instantaneous cutting force and thrust force are required to validate the mechanics model. However, experimental measurement of the forces in VAM is limited by the dynamometer bandwidth (3 kHz), which is less than the vibration assistance frequency (7.5 kHz) in this thesis. Therefore, the mechanics model is validated using finite element (FE) simulations by comparing the predicted analytical forces and simulated forces in EVAM of Al 6061. The mechanics model is used to develop the physics-based model to analyze the effect of vibration assistance on chip formation in EVAM of Zr-BMG. The model is used to predict the variations of the shear stress and temperature in PSZ responsible for the chip segmentation in EVAM of Zr-BMG. Furthermore, the effect of vibration assistance on chip segmentation frequency, free volume and temperature are discussed.

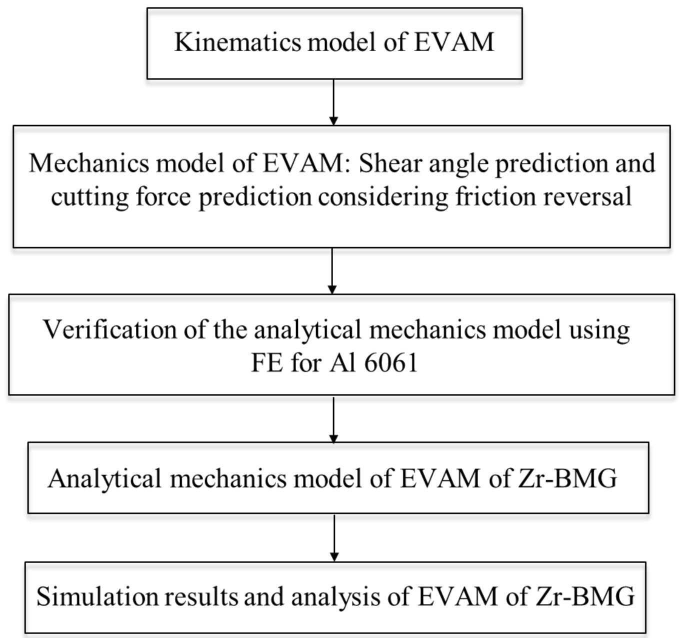

Figure 4.1 Flow chart representing the organization of Chapter 4.

4.2 Kinematics of 2-D VAM

The fundamental principle of 2-D VAM kinematics is illustrated in Figure 4.2. Let the frequency of the applied vibration be f, and the amplitudes of vibrations in cutting (*x*) and feed (*y*) directions are A_x and A_y respectively. The chip formation mechanism changes with the uncut chip thickness in 2-D VAM [67,90,91]. Discontinuous chip formation occurs when the uncut chip thickness is lower than the amplitude of the vibration in the *y*-direction (A_y), while continuous chip formation occurs when the uncut chip thickness is greater than or equal to $2A_y$. In this thesis, the mechanics of deformation for BMGs using 2-D VAM are developed when uncut chip thickness is greater than $2A_y$. The trajectory of the cutting tool is represented as a function of time (*t*):

$$\begin{cases} P_x(t) = v_c t + A_x \sin(\omega t) \\ P_y(t) = -A_y \sin(\omega t + \varphi) \end{cases} \tag{4.1}$$

where $P_x(t)$ and $P_y(t)$ are the cutting tool location in the coordinate system shown in Figure 4.2 (b). ω is the circular frequency (i.e., $\omega = 2\pi f$) and φ is the phase difference between the applied vibration in *x*- and *y*- directions. The shape of the cutting tool trajectory depends on the magnitude of the vibration amplitudes and the phase difference of the applied vibrations in the two directions. The tool with the vibration assistance moves in an elliptical trajectory when the amplitude in the cutting direction (A_x) is at least 1.5 times the amplitude in the normal direction (A_y), with a phase difference of 90°, defined as elliptical vibration-assisted machining (EVAM).

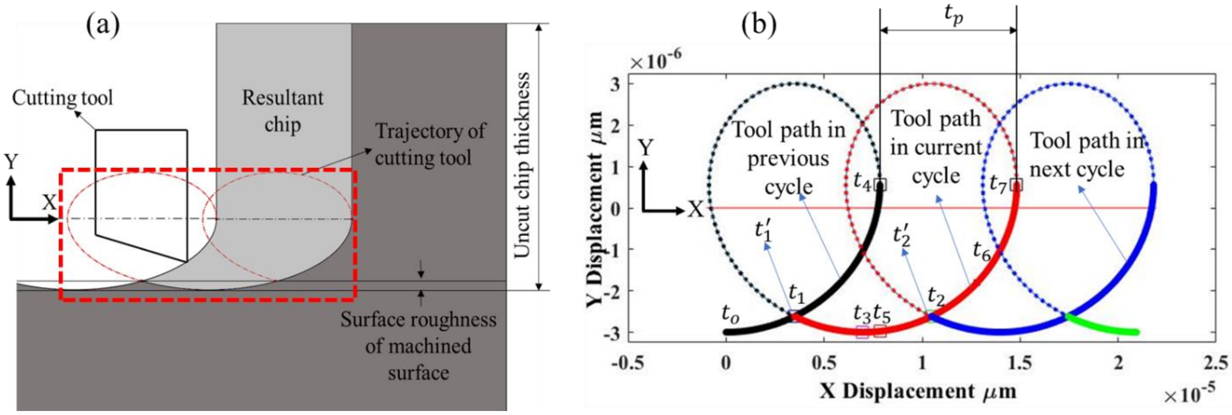

Figure 4.2 (a) Schematic of EVAM, and (b) Elliptical trajectory of the tool tip.

The relative cutting tool velocities with respect to the workpiece are expressed as

$$\begin{cases} v_x(t) = v_c + A_x \omega \cos(\omega t) \\ v_y(t) = -A_y \omega \cos(\omega t + \varphi) \end{cases} \tag{4.2}$$

The instantaneous angle (θ) of the resultant velocity of the tool with respect to the *x*-axis is then given by

$$\theta(t) = tan^{-1}\left(\frac{-v_y(t)}{v_x(t)}\right) \tag{4.3}$$

The initial reference time t_o is defined corresponding to the tool location with zero velocity in *y*-direction when the tool tip is at the bottom of its locus, as shown in Figure 4.2-(b). Three vibration cycles are presented in Figure 4.2-(b), including the previous vibration cycle (black colour), current vibration cycle (red colour), and next vibration cycle (blue colour). The time instance t_1 represents the beginning of the current cutting vibration cycle.

For the current cutting cycle, the cutting tool is in contact with the workpiece starting from t_1 to t_7 (solid red line in Figure 4.2 (b)). t_7 is the time instance of the tool leaving the workpiece, until it is in touch with the workpiece material in the next vibration cycle at the time instance of t_2. Similarly, t_4 is the time instance of the tool leaving the workpiece in the previous cutting cycle. t_1' is the time instance in the previous cycle when the tool is moving upwards, where the coordinates of the tool in *x*- and *y*- directions coincide with the tool coordinates at the time instance

t_1. The trajectory of the tool path in the previous cutting cycle from t_1' to t_4 represents the left side of the uncut chip material in the current cycle, and decides the geometry of the uncut chip material in EVAM. Therefore, $t_2 = t_1 + T_p$ and $t_7 = t_4 + T_p$, where T_p is the time period for one cycle of the assisted vibration, given by $1/f$. t_6 is defined by the time instance that the magnitude of the cutting tool velocity in y-direction exceeds the chip velocity, so the friction force at the tool-chip interface reverses its direction. The time range from t_1 to t_7 (solid red line) represents the total time when the cutting tool is in contact with the workpiece in the current vibration cycle. The time range from t_7 to t_2 (dotted red line) is the tool-workpiece separation period.

In Figure 4.2-(b), t_1 and t_1' represent the time instances where the values of tool coordinates in *x*- and *y*- directions are the same. Hence, t_1 and t_1' are obtained by solving the following Eqs. (4.4) and (4.5) numerically

$$v_c t_1 + A_x \sin(\omega t_1) = v_c t_1' + A_x \sin(\omega t_1'), \qquad 0 < t_1' < t_1 < T_p \quad (4.4)$$

$$-A_y \sin(\omega t_1 + \varphi) = -A_y \sin(\omega t_1' + \varphi), \qquad 0 < t_1' < t_1 < T_p \quad (4.5)$$

The time instance t_3 corresponds to the bottom point of the tool trajectory, where the velocity in y-direction is zero, and is obtained based on the condition $\theta(t) = 0$, given by

$$t_3 = \frac{3\pi - 2\varphi}{4\pi f} \quad (4.6)$$

The time instance t_4 is determined by making the relative velocity of the tool in cutting direction equal to zero, expressed as

$$t_4 = \frac{1}{\omega} cos^{-1}\left(\frac{-V_c}{A_x \omega}\right) \quad (4.7)$$

The time instance t_5 corresponds to the tool position when its *x* coordinate is the same as that of t_4. It is numerically obtained by solving the Eq. (4.8)

$$v_c t_4 + A_x \sin(\omega t_4) = v_c t_5 + A_x \sin(\omega t_5) \quad (4.8)$$

As a result, all the time instances in the current vibration cycle corresponding to the critical tool positions for the mechanics analyses are obtained.

The periods of cutting and separation depend on the ratio of the original cutting velocity (v_c) to the maximum vibration velocity of the tool in the cutting direction, which is defined as the horizontal speed ratio (HSR) as

$$HSR = \frac{v_c}{\max(v_x)} = \frac{v_c}{2\pi f A_x} \tag{4.9}$$

There is no separation between the tool and workpiece when HSR is greater than or equal to 1. The percentage of the time period spent in cutting for each vibration cycle (duty cycle) with respect to the HSR is presented in Figure 4.3. HSR plays a significant role in analyzing the mechanics of EVAM. Zhang et al. [92] assumed that the shear angle varies within each vibration cycle, which is due to the direction reversal of tool-chip friction force. Besides, the shear angle value is independent of HSR in the model. On the other hand, the experimental studies by Shamoto et al. [90, 93] proved that the shear angle changes with HSR in the EVAM process, but it can be assumed as a constant within the individual vibration cutting cycle. It was also found that the shear angle increases when the HSR values decrease, and vice versa. Shamoto et al. [93] predicted the shear angle based on the minimum cutting energy principle in EVAM. However, the shear velocity of workpiece material in PSZ and the chip velocity are assumed to be always in the same direction, which does not apply to the actual cutting situation. There is a need to further analyze the effect of HSR on the change of shear angle in the mechanics model of EVAM. In this thesis, to understand the chip formation mechanism in EVAM, a new mechanics model is developed to determine the variation of the shear angle with respect to HSR.

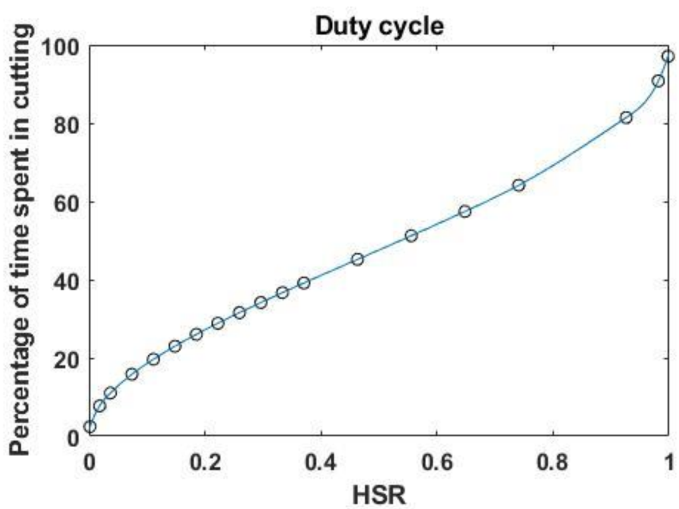

Figure 4.3 Percentage of cutting time in one vibration cycle with respect to HSR.

4.3 Mechanics model of EVAM

4.3.1 Prediction of shear angle with HSR in EVAM

In the machining process without vibration assistance, as the chip formation starts to occur, the strain of the workpiece material increases in the PSZ until it reaches a constant value. In the EVAM process, intermittent tool-chip contact occurs, with the contacting period depending on the HSR value. At lower HSR values, the net tool displacement causing shearing during the tool-workpiece contact is in the order of micrometres. The strain of the workpiece material in the PSZ with this tool displacement is lower compared to the strain in steady-state machining [94-96]. Assuming plane strain deformation, and based on constant shear angle condition [68,90,93], the shear strain generated in the PSZ is expressed as a function of tool velocity in EVAM:

$$\gamma = \int \dot{\gamma}\, dt = \int \frac{V_s(t)}{\Delta h} dt \tag{4.10}$$

where γ is the shear strain of the workpiece material in PSZ in the whole vibration cycle, $\dot{\gamma}$ is the instantaneous strain rate, V_s is the shear velocity, and Δh is the thickness of the PSZ. Let ϕ be the shear angle for a given HSR, the shear strain in terms of the cutting velocity is derived as

$$\gamma = \int \frac{V_c(t)\cos(\alpha) sin\phi}{mh_{un} * \cos(\phi - \alpha)} dt \tag{4.11}$$

where h_{un} is the uncut chip thickness, m is the ratio between the thickness of PSZ to the uncut chip thickness. The time period from $t_1 to\ t_5$ is neglected in the chip formation analyses because it mainly involves the ploughing of the workpiece material, when the uncut chip thickness is less than the amplitude of vibration assistance in the y-direction. Therefore, the total accumulated shear strain induced by the tool on the workpiece material in PSZ is obtained for the time period of t_5 to t_7 as

$$\gamma \approx \int_{t5}^{t7} \frac{V_c(t)\cos(\alpha) sin\phi}{mh_{un} * \cos(\phi - \alpha)} dt \tag{4.12}$$

Based on the tool displacement for the time period from t_5 to t_7, the strain in terms of HSR is derived as

$$\gamma = \frac{2\pi A_x * \mathrm{HSR} * \cos(\alpha) sin\phi}{m * h_{un} * \cos(\phi - \alpha)} \tag{4.13}$$

Since this model is applied when the uncut chip thickness is much larger than the vibration amplitude in the y-direction, the variation in h_{un} due to the vibration assistance can be neglected as the magnitude of the variation is equal to the amplitude of vibration A_y. Based on Shaw et al. [70,71], the shear stress of the workpiece material is modelled as a linear function of strain:

$$\tau = A_o + B_o\,\gamma \tag{4.14}$$

where A_o is the initial yield shear stress, and B_o is the strain hardening coefficient of the workpiece material. The effects of strain rate and temperature on the shear stress are neglected for the machining process with a low cutting speed, which is smaller than the maximum vibration speed (17 m/min). Then, the maximum cutting force in each vibration cycle is expressed as

$$F_c = \left[A_o + B_o * \frac{2\pi A_x * \mathrm{HSR} * \cos(\alpha) sin\phi}{m h_{un} * \cos(\phi - \alpha)}\right]\left(\frac{b h_{un}}{sin\phi}\right)\frac{\cos(\beta - \alpha)}{\cos(\phi + \beta - \alpha)} \tag{4.15}$$

The energy spent during the tool chip contact period varies with time, as the cutting velocity is time-dependent. The cutting power is given by

$$E_v(t) = \left[A_o + B_o * \frac{2\pi A_x * \mathrm{HSR} * \cos(\alpha) sin\phi}{m h_{un} * \cos(\phi - \alpha)}\right]\left(\frac{b h_{un}}{sin\phi}\right)\frac{\cos(\beta - \alpha)}{\cos(\phi + \beta - \alpha)} V_c(t) \tag{4.16}$$

The energy reduces from a maximum value when the velocity in the y-direction is zero (t_3) to a minimum value at t_7 as the cutting velocity reduces. However, it is assumed that shear angle is time-invariant in EVAM, and the cutting velocity does not depend on the shear angle. Therefore, the variation in energy with time is neglected. The shear angle in EVAM is identified by minimizing the energy consumed in the chip formation process, expressed as:

$$\frac{dE_v}{d\phi} = 0 \tag{4.17}$$

As Eq. (4.16) is influenced by the HSR value, the shear angle ϕ_{HSR} depends on the HSR value, and is determined based on the minimum energy principle. The proposed model is used to determine the effect of HSR on the shear angle in EVAM. Since the effect of vibration assistance kinematics on the change in shear angle applies to general metal alloys, aluminum alloy Al6061 with well-known mechanical properties is first used to evaluate the effect of HSR on the shear angle from the proposed model. The shear yield strength and the strain hardening coefficient for Al 6061 are A_o= 207 MPa and B_o =55 MPa [71,97]. The predicted shear angles with varying HSR values (corresponding to the cutting speed range of 0.85 m/min -16.5 m/min) at an uncut chip thickness of 20 μm are presented in Figure 4.4. It is observed that the shear angle reduces from 33.5° to 18° with an increase of HSR from 0.05 to 0.975. This is due to the material hardening effect included in the kinematic model. The experimental validation of the shear angle with HSR is presented in Chapter 5.

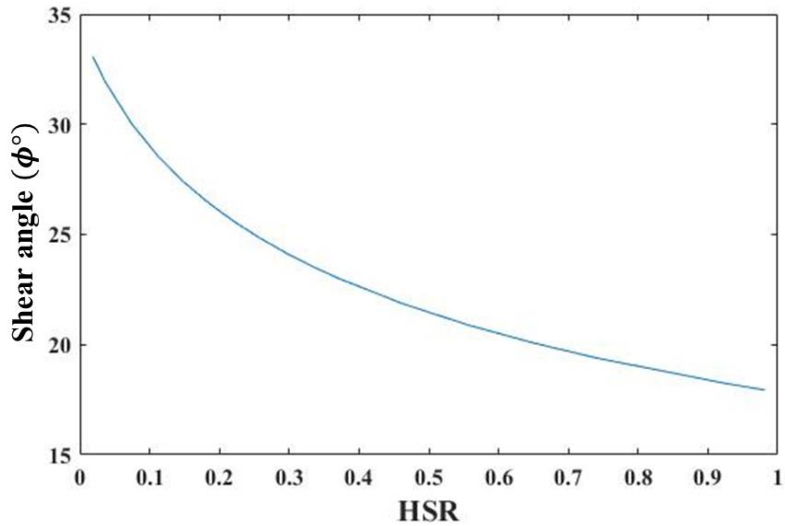

Figure 4.4 Variation of shear angle with the HSR in EVAM of Al 6061.

4.3.2 Prediction of cutting force in EVAM

The shear angle predicted in the developed mechanics model is used to analyze the effect of EVAM on the cutting forces. Due to the elliptical trajectory with vibration assistance, friction reversal occurs when the cutting tool's vertical velocity exceeds the chip velocity [90,93]. In order to capture the time instance of friction reversal, instantaneous cutting forces are required. Due to the limitation of the experimental setup, FE simulations are performed to analyze the force in EVAM. In order to have a more accurate comparison with FE simulation results, the change of instantaneous uncut chip thickness due to vibration assistance in y-direction is considered in the mechanics model.

The uncut chip thickness depends on the trajectory of the tool from the previous cutting cycle from the time t_1 to t_5. Let r be the ratio of time spent by the tool in the previous cutting cycle ($t_4 - t_1'$) to the time spent by the tool in the current cutting cycle ($t_5 - t_1$), and is expressed as

$$r = \frac{t_4 - t_1'}{t_5 - t_1} = \frac{t_4 - (T_p - t_1)}{t_5 - t_1} \tag{4.18}$$

Let P_y be the tool position in *Y* coordinate in the previous cutting cycle with respect to the instantaneous time *t* in the current cutting cycle. $P_y(t)$ is calculated as

$$P_y(t) = -A_y \sin\big(\omega\big(r * (t - t_1) + (T_p - t_1\big) + \varphi\big) \tag{4.19}$$

Then the uncut chip thickness for time $(t_1 - t_5)$ is obtained by

$$h_p(t) = P_y(\mathrm{t}) - (-A_y \sin(\omega t + \varphi)) \tag{4.20}$$

The uncut chip thickness from t_5 to t_7 can be calculated by $h_m - P_y(t)$, where h_m is the given nominal uncut chip thickness. Therefore, the instantaneous uncut chip thickness ($h_{un}(t)$) at any time *t* is given by

$$h_{un}(t) = \begin{cases} 0, \;\; t < t_1, t \geq t_7 \\ P_y\big(r * (t - t_1) + (T_p - t_1)\big) - P_y(t), t_1 \leq t < t_5 \\ h_m - P_y(t), t_5 \leq t < t_7 \end{cases} \tag{4.21}$$

Figure 4.5 shows the instantaneous uncut chip thickness variation for a nominal uncut chip thickness value of 20 μm with an HSR of 0.3. The deformation process during time $(t_5 - t_1)$ corresponds to ploughing rather than shearing, as the uncut chip thickness is close to the edge radius of the cutting tool. The uncut chip thickness from time $(t_7 - t_5)$ corresponds to shearing-dominant deformation. The ploughing region is relatively lower compared to the shearing region, as shown in Figure 4.5. It should be noted that the time spent in ploughing and shearing regions depends on the HSR value. As the HSR value increases, the ploughing region reduces and can be neglected when the nominal uncut thickness is much larger than the tool's displacement amplitude in the *y*-direction.

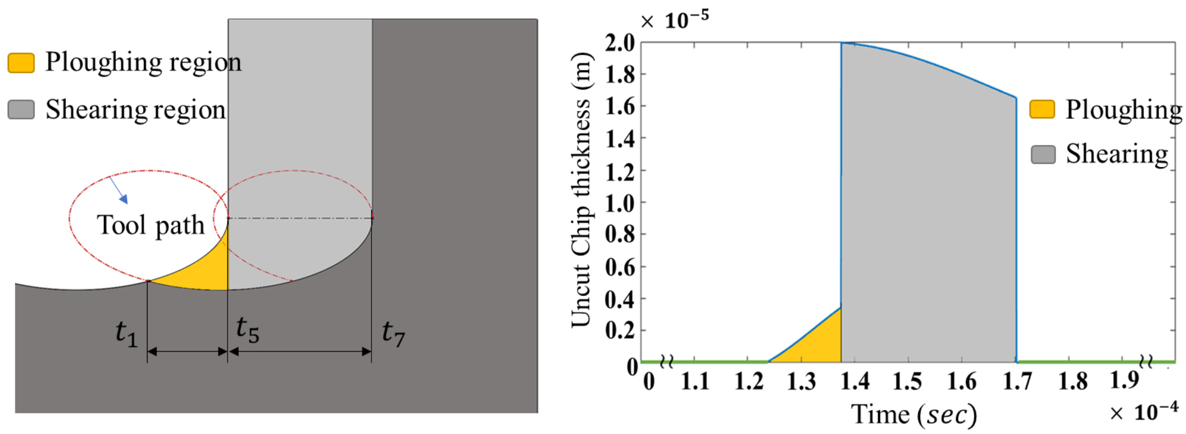

Figure 4.5 (a) Schematic representation of EVAM showing ploughing and shearing regions, and (b) Instantaneous uncut chip thickness with time in EVAM.

Based on a given HSR value, the time instance t_6 which corresponds to the direction reversal of the tool-chip friction in Figure 4.2 (b) is obtained by solving the velocity diagram. Let V_s be the shear velocity of the workpiece material at the shear angle ϕ. The shear velocity is obtained as

$$v_s = \frac{v_x(t)\cos(\alpha)}{\cos(\phi - \alpha)} \tag{4.22}$$

where α is the tool rake angle, and $V_x(t)$ is the horizontal component of the instantaneous resultant velocity. The velocity hodograph of the chip formation is presented in Figure 4.6.

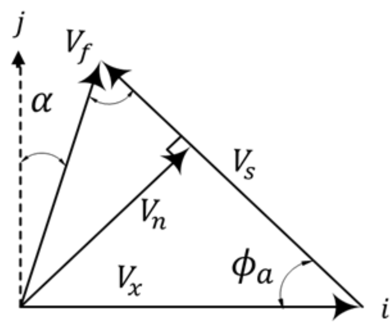

Figure 4.6 Velocity hodograph of chip formation

The instantaneous chip velocity V_f is determined as

$$\vec{V_f} = \vec{V_s} - \vec{V_x} \tag{4.23}$$

$$\vec{V_f} = (V_s\cos(\phi) - V_x).\hat{\imath} + \frac{V_s\sin(\phi)}{\cos(\alpha)}.\hat{\jmath} \tag{4.24}$$

The time instance t_6 is obtained based on the condition that the workpiece and cutting tool velocities in the direction of chip flow are the same, thus t_6 is obtained by solving Eq. (4.27)

$$\left|\left(V_s \cos(\phi) - v_x(t_6)\right).\hat{\imath} + \frac{V_s \sin(\phi)}{\cos(\alpha)}.\hat{\jmath}\right| = \left|-A_y \omega \cos(\omega t_6 + \varphi)\right| \tag{4.25}$$

where $\hat{\imath}$ and $\hat{\jmath}$ are the unit vectors in cutting and feed directions, respectively.

The cutting forces are predicted considering the instantaneous uncut chip thickness, shear angle, and friction reversal at the tool-chip interface. Figure 4.7 shows the configuration of the friction and normal forces before and after the friction reversal. The force symbols after the friction reversal are labelled by " $'$ ". It is assumed that the value of the friction coefficient remains the same, with only change of the friction force direction. As shown in Figure 4.7 (b), the resultant force R' changes the direction compared to R due to the friction reversal. From the force equilibrium condition, the shear force (F_s) and normal force perpendicular to the shear plane (F_n) before friction reversal is expressed in terms of the friction and normal forces on rake face, given by

$$F_s = N_{ps} - F_{ps} = N\cos(\phi_{HSR} - \alpha) - Fsin(\phi_{HSR} - \alpha) \tag{4.26}$$

$$F_n = N_{ns} + F_{ns} = Nsin(\phi_{HSR} - \alpha) + F\cos(\phi_{HSR} - \alpha) \tag{4.27}$$

After the friction reversal, the shear force and normal force perpendicular to the shear plane is

$$F_s' = N_{ps} + F_{ps} = N'\cos(\phi_{HSR} - \alpha) + F'sin(\phi_{HSR} - \alpha) \tag{4.28}$$

$$F_n' = N_{ps} - F_{ps} = N'\sin(\phi_{HSR} - \alpha) - F'cos(\phi_{HSR} - \alpha) \tag{4.29}$$

From the vector summation of forces along the normal direction to the shear plane, the normal force F_n' on the shear plane is less than F_n. Assuming the shear strength of material remains constant, the ratio of resultant force before and after the friction reversal is given by

$$\frac{R'}{R} = \frac{\cos(\phi + \beta - \alpha)}{\cos(\phi - \beta - \alpha)} \tag{4.30}$$

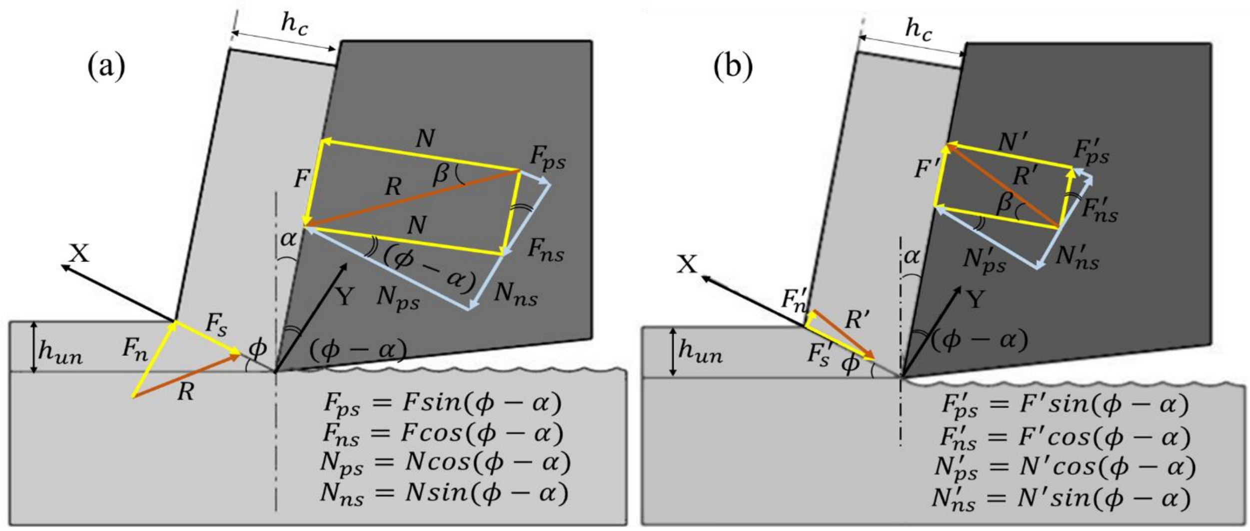

Figure 4.7 The configuration of forces: (a) before friction reversal, and (b) after friction reversal.

The ratio is less than one for any values of shear and friction angles. The normal force on the tool rake face (N') after the friction reversal is given by

$$N' = N\frac{\cos(\phi + \beta - \alpha)}{\cos(\phi - \beta - \alpha)} \tag{4.31}$$

It is assumed that the friction coefficient before and after friction reversal is the same, that is $\mu = F/N = F'/N'$. Therefore, the friction angle in EVAM can be defined as $\beta_v(t) = \beta sign(V_r(t))$, where β_v is the updated friction angle, which determines the direction of the friction force related to the relative tool-chip velocity $V_r(t) = V_f(t) - V_y(t)$. Hence, the instantaneous cutting force and thrust force with respect to time, including friction reversal, is obtained by

$$F_c(t) = \tau_m w h_{un}(t)\frac{cos(\beta_v(t) - \alpha)}{sin(\phi_{HSR})cos(\phi_{HSR} + \beta_v(t) - \alpha)} \tag{4.32}$$

w is the width of cut, τ_m is the shear strength of the material measured from machining experiments and ϕ_{HSR} is the predicted shear angle with respect to HSR. Similarly, the thrust force is predicted as

$$F_t(t) = \tau_m w h_{un}(t)\frac{sin(\beta_v(t) - \alpha)}{(sin(\phi_{HSR})cos(\phi_{HSR} + \beta_v(t) - \alpha)} \tag{4.33}$$

4.4 Validation of force prediction in EVAM using finite element simulations

Instantaneous cutting force measurement is required to validate the kinematic model and force prediction in the proposed analytical mechanics model for EVAM. However, the frequency of vibration assistance of EVAM in this study is 7.5 kHz, which is higher than the bandwidth limit of the dynamometer (typically below 3 kHz) used for force measurement in experiments. Therefore, finite element (FE) simulations of EVAM are conducted to validate the analytical mechanics model for force prediction considering friction reversal. Al6061 is chosen as the workpiece material to include the effect of HSR on the shear angle variation. Experimental studies on EVAM of Zr-BMG are presented in detail in Chapter 5.

For the FE modelling of the EVAM process, a 2-D FE model under plane strain condition is developed using the ABAQUS/Explicit platform. The workpiece material is an isotropic plastic material, and the cutting tool is assumed to be a rigid part to reduce the calculation time. The specifications of the cutting tool and workpiece in the FE model are listed in Table 4.1. A convergence study is performed to assign proper meshing density to ensure the FE model's prediction accuracy. It is observed that the meshing density with 46980 elements shows that the variation in cutting force and stress is less than 5% compared to simulations with finer mesh. The size of each element is less than 1 μm^2, which ensures adequate simulation accuracy. Cutting velocity is applied to the tool, and vibration assistance is applied along the cutting direction and feed direction. The workpiece is fixed, as shown in Figure 4.8. The coulomb's friction law is used to define the friction at the tool chip interface considering the sticking and sliding phenomenon. The sticking region is dependent on the shear stress of the material with the plastic flow. The friction coefficient used in the simulation is 0.38, and it was obtained from measured cutting forces at varying uncut chip thickness (10 μm to 50 μm) without vibration assistance. The details of the calibration for the friction coefficient are listed in Appendix 2.

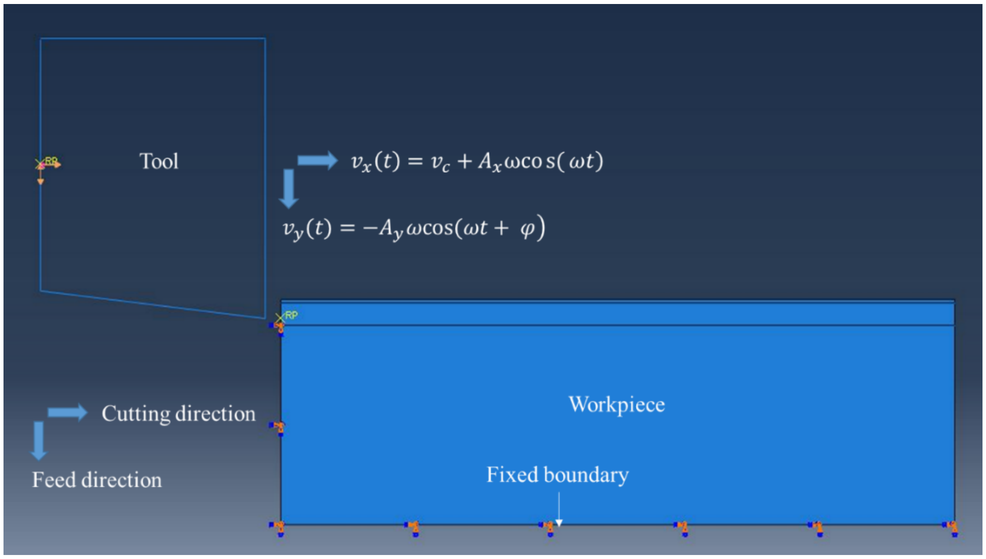

Figure 4.8 2-D FE model showing boundary conditions.

The workpiece's material constitutive model plays a vital role in the chip formation and cutting force generation in the simulation process. Johnson-Cook (JC) model is used to model the workpiece material's constitutive property, expressed as [98,99].

$$\sigma_{eq} = [A + B(\varepsilon)^n]\left[1 + C.ln\left(\frac{\dot{\varepsilon}}{\dot{\varepsilon}_o}\right)\right]\left[1 - \left(\frac{T - T_{room}}{T_{Melt} - T_{room}}\right)^m\right] \quad (4.34)$$

where σ_{eq} is the equivalent stress, ε is the equivalent plastic strain, $\dot{\varepsilon}/\dot{\varepsilon}_o$ is the reference strain rate, T_{melt} is the melting temperature, and T_{room} is room temperature. *A*, *B*, *C*, *n*, and *m* are material constants, where *A* is initial yield strength, *B* is hardening modulus, *C* is strain rate dependent coefficient, *n* is work hardening exponent, *m* is the thermal softening coefficient. The parameters used in modelling the workpiece are listed in Table 4.2. Johnson-Cook failure model is employed to simulate the material deformation and chip formation, and the damage parameters used in this simulation are listed in Table 4.2. The dynamic explicit solver is used, neglecting the effect of temperature to increase the computational speed. Besides, as the cutting speeds in EVAM are lower than 17 m/min in the simulations, the effect of change of strain rate and temperature with cutting speed on the material constitutive property can be neglected.

Table 4.1 Properties of tool and workpiece, and simulation parameters.

Materials and dimension in simulation	Workpiece: Al 6061 (0.5 × 0.25 mm^2) Cutting Tool: Rigid (0.25 × 0.25mm^2)
Machining conditions and dimensions	Simulation: HSR: 0.1, 0.25, 0.5, 0.75 Uncut chip thickness: 20 μm Tool angles: Rake angle 0° and clearance angle 7°
Element type	CPE4R
Element distortion Control	Length ratio 0.1
Interactions	General contact: Tool- master surface, workpiece- slave surface
Interface friction	Tangential behavior: penalty contact: coefficient of friction: 0.38
Element deletion	Yes
Boundary Condition	Tool moving with cutting velocity and vibrating along cutting direction and feed direction. Frequency of applied vibration: 7.5 kHz Amplitude in cutting direction: 6 μm Amplitude in feed direction: 3 μm Workpiece fixed

Table 4.2 Mechanical properties of Al-6061 used in the FE simulations.

Density				2700 Kg/m^3	
Young’s modulus				68.9 GPa	
JC model parameters [98]					
A (MPa)	B (MPa)	C	n	m	Reference strain rate s^{-1}
324.1	153.8	0.002	0.42	1.3	1
JC damage parameters [99]					
d1	d2	d3	d4	d5	
-0.77	1.45	-0.47	0	1.6	

The comparison of chip formation with and without vibration assistance at the uncut chip thickness of 20 μm and 1.7 m/min is shown in Figure 4.9. The accumulated equivalent plastic strain values (PEEQ) in the chip in EVAM at 0.1 HSR are approximately half compared to the equivalent plastic strain values in cutting without vibration assistance. The reduction in effective plastic strain is due to the low strain induced by the tool at a low HSR value (0.1) in EVAM, as mentioned in Section 4.3.1. The predicted forces from the analytical mechanics model and the FE simulations are compared and shown in Figure 4.10. It is observed that the cutting and thrust force profiles in each vibration cycle from the analytical model and the FE simulations are in agreement. The predicted time instance corresponding to the friction reversal is compared between these two models with respect to HSR values of 0.1, 0.25, 0.5, and 0.75, shown in Figure 4.10. The time instances corresponding to the friction reversal predicted by the analytical model and the FE simulations are closer at lower HSR values of 0.1 and 0.25, and slightly deviate when HSR values increase to 0.5 and 0.75. A maximum error of 13% was observed when HSR is 0.75. The cutting forces from the analytical mechanics model and the FE model are compared, and a maximum error of 12% in cutting force and 20% in thrust force before friction reversal is observed. This is due to the neglected ploughing effect by the tool edge while modelling the cutting forces in the analytical model [69, 90]. The change in the predicted forces from the analytical model is instantaneous, as the friction is assumed to change the direction instantaneously, while the change in the simulated forces from the FE model is gradual at the time instance of friction reversal. This is due to the sticking-slipping phenomenon at the tool-chip contact in the FE simulations, which is neglected in the analytical mechanics model.

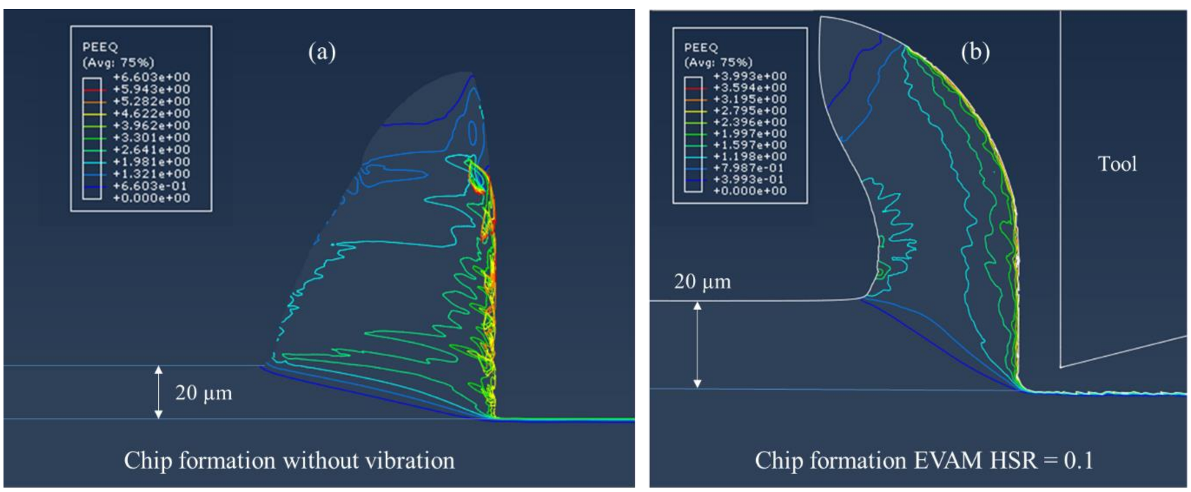

Figure 4.9 Comparison of chip formation and effective strain: (a) no vibration assistance at 1.7 m/min, and (b) EVAM with HSR 0.1 (1.7 m/min).

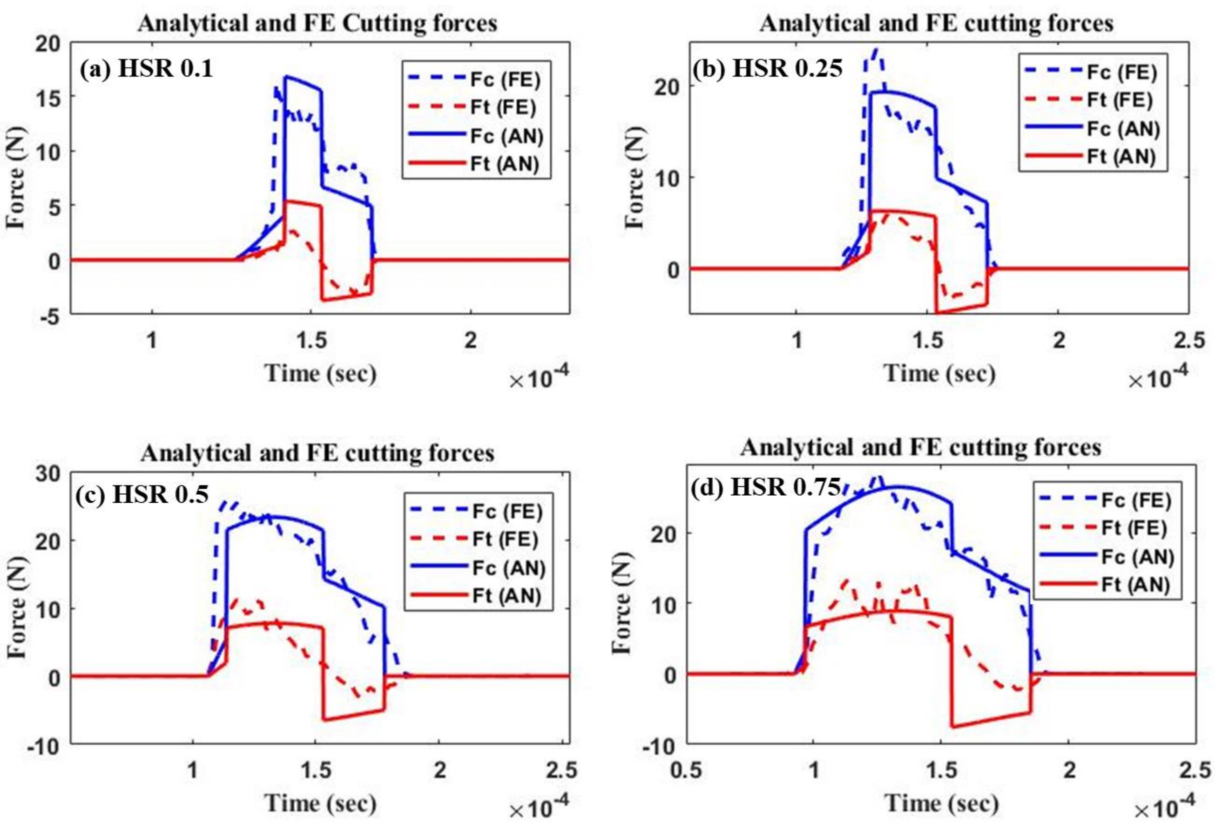

Figure 4.10 Comparison of force predictions from analytical and FE model with different HSR values: (a) 0.1, (b) 0.25, (c) 0.5, and (d) 0.75.

4.5 Modelling segmented chip formation in EVAM of Zr-BMG

The developed kinematics and mechanics model are applied to Zr-BMG material in order to determine the effect of intermittent tool-workpiece contact and the friction reversal on the shear angle, temperature, free volume and shear stress variation in EVAM of Zr-BMG. It is demonstrated in Section 4.3 that the strain hardening of the material is the primary reason for the change of shear angle with vibration assistance. However, BMG materials do not show a noticeable strain hardening effect [100, 101]. For the stress-strain hardening equation:

$$\tau = A_o + B_o \gamma^n \tag{4.35}$$

the corresponding mechanical parameters for Zr-BMG are: A_o= 651 MPa, B_o =95 MPa, and n = 0.05 based on Wang et al. [102] and Joo et al. [103]. The parameter A_o is selected from [103], and it is lower than the yield strength of the Zr-BMG at room temperature, which is due to the effect of machining-induced softening [23-25]. Assuming the hardening exponent is the same as that proposed by Wang et al. [102], the parameter B_o is calculated based on the maximum shear strength of the material from orthogonal cutting experiments. The relationship between the shear angle and the HSR values at an uncut chip thickness of 40 μm for Zr-BMG is shown in Figure 4.11. It is observed that there is no significant change in shear angles with HSR values for Zr-BMG compared to Al-6061. Therefore, the change of shear angle values with HSR in EVAM of Zr-BMG can be neglected.

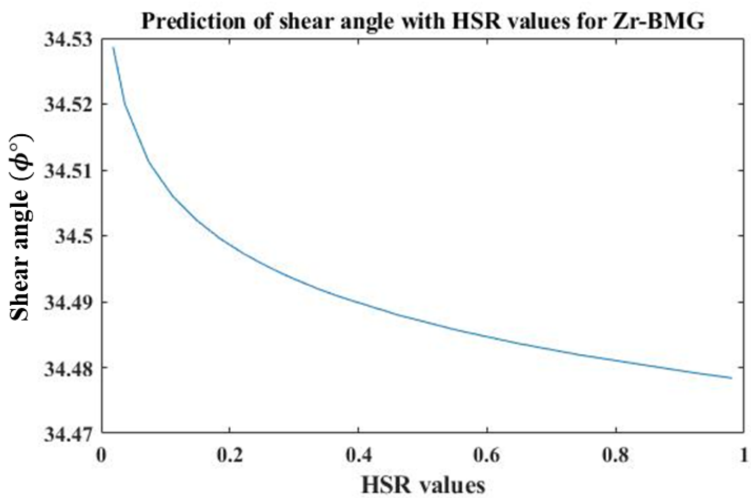

Figure 4.11 Predicted shear angle variation with HSR value in EVAM of Zr-BMG.

Although the vibration assistance does not show an obvious effect on the change of shear angle, the variations of the temperature, free volume, and stress in the PSZ associated with the shear band formation and chip segmentation are expected to be influenced by the intermittent tool-workpiece contact and the friction reversal enabled by the vibration assistance. Therefore, the developed kinematic model of chip formation is developed to determine the quantitative relationship between the vibration assistance parameters and the chip segmentation mechanism in EVAM of Zr-BMG. A window function $U(t)$ is used to determine the time of contact for ploughing, shearing, and tool-workpiece separation, expressed as:

$$U(t) = \begin{cases} 0: \rightarrow iT_p \leq t < (i + r_p)T_p \\ 1: \rightarrow (i + r_p)T_p \leq t < (i + r_c)T_p \\ 0: \rightarrow (i + r_c)T_p \leq t < (i + 1)T_p \end{cases} \quad (i = 0,1, \ldots \ldots) \tag{4.36}$$

where r_p is the ratio of time spent in ploughing to the vibration period given by $r_p = (t_5 - t_1)/T_p$, r_s is the ratio of time spent in shearing to the vibration period expressed as $r_s = (t_7 - t_5)/T_p$, and r_c is the summation of r_p and r_s, where i represents the number of vibration cycles, counting the initial cycle as zero. In the tool-workpiece contact period, from force equilibrium conditions expressed by Eqs. (4.26) and (4.28), the change of shear stress on the shear plane with respect to time, including tool chip contact, separation, and friction reversal, is presented as

$$\frac{d\tau_s}{dt} = m[nU(t)]ksin^2\phi_{HSR}U_f(t)(\dot{\gamma}_{sv} - \dot{\gamma}_p) \tag{4.37}$$

where n, m and k are the same as the parameters presented in Section 3.2, ϕ_{HSR} is the average shear angle in EVAM. $U_f(t)$ is the window function to determine the effect of friction reversal, given by

$$U_f(t) = \begin{cases} c_b: \rightarrow iT_p \leq t < \left(i + r_f\right)T_p \\ c_a: (i + r_f)T_p \leq t < (i + r_{tc})T_p \\ 0: \rightarrow (i + r_{tc})T_p \leq t < (i + 1)T_p \end{cases} \quad (i = 0,1, \dots \dots) \tag{4.38}$$

where c_b is defined as $\left(1 - \mu tan(\phi_a - \alpha)\right)$ and c_a is defined as $\cos(\phi + \beta - \alpha) / \cos(\phi - \beta - \alpha)[1 + \mu \tan(\phi - \alpha)]$ based on the shear force from Eqs. (4.26) and (4.28). r_f is the ratio of time from t_6 to t_1 to the vibration period given by $r_f = (t_6 - t_1)/T_p$. $\dot{\gamma}_{sv}$ is the shear strain rate, expressed as

$$\dot{\gamma}_{sv} = \frac{v_s}{\Delta h} = \frac{v_x(t)\cos(\alpha)}{\cos(\phi_{HSR} - \alpha)\,\Delta h} = \frac{[v_c + A_x\omega\cos(\omega t)]\cos(\alpha)}{\cos(\phi_{HSR} - \alpha)\,\Delta h} \tag{4.39}$$

Δh is the shear plane thickness, given by

$$\Delta h \approx msin\phi_{HSR} * (h_{un}) \tag{4.40}$$

$\dot{\gamma}_p$ is the material shear strain rate expressed by the flow law. In the tool-workpiece separation stage, the shear stress decreases due to the stress relaxation during the unloading from the cutting tool. According to Guiu and Pratt [104,105], for metallic metal alloys, the shear stresses reach a steady value after the stress relaxation period, governed by the velocity of dislocations in the material. For BMG materials, the stress relaxation is governed by activation energy, free volume, temperature, and type of loading or strain rate. In the EVAM process, the tool-workpiece separation period is in the range of 0.01 ms – 0.1 ms. It is much smaller than the experimentally identified stress relaxation time for BMG, which ranges from few seconds to minutes [106, 107]. Therefore, the change of shear stress due to stress relaxation during tool-chip separation is neglected compared to the stress variation caused by shear localization. As a result, in the tool-workpiece separation period, the change in shear stress with time is assumed to be zero, expressed as

$$\frac{d\tau_s}{dt} = 0 \tag{4.41}$$

The constitutive model of Zr-BMG, which relates the shear stress with the strain rate, free volume, and temperature, is the same as that in Section 3.3 [108], expressed as

$$(\dot{\gamma_p}\ ) = \dot{\gamma}_{stz}\ = \gamma_v exp\left(-\frac{1}{\zeta}\right) exp\left(-\frac{W(\tau_s)}{K_b T}\right) \tag{4.42}$$

where γ_v is pre-exponential constant, ζ is the free volume available per STZ, $W(\tau_s)$ is the activation energy required K_b is Boltzmann constant, and T is temperature.

The evolution of temperature and free volume is necessary to estimate the material flow behaviour in the PSZ in the EVAM process. The primary source of heat generation is the plastic deformation of the material in PSZ. The generated heat is also extracted from the PSZ simultaneously through convection and advection. In addition, the tool-workpiece separation in EVAM only involves heat diffusion without heat generation. The temperature variation in the PSZ is modelled as a 1-D heat equation, expressed as

$$\frac{dT}{dt} = \ U(t) q_{Tq} \tau_s \dot{\gamma_p} + \chi_v (T_0 - T) \tag{4.43}$$

where $\chi_v = (v_x(t)\sin(\phi)\ U(t) + 4k_d/h_a)/h_a$ is the coefficient of thermal dissipation in EVAM. There is no material flow during the tool-workpiece separation stage. Therefore, the coefficient is expressed as $\chi_v = (4k_d/h_a)/h_a$ when the tool and workpiece separation occurs.

Similarly, the generation and diffusion of the free volume is expressed as

$$\frac{d\varsigma}{dt} = \xi_v(\zeta_o - \zeta) + U(t)\mathrm{exp}\left(\frac{-1}{\zeta}\right) exp\left(\frac{-\mathrm{W}}{K_b T}\right)\frac{2KT}{\zeta S}\left[cosh\left(\frac{\tau_s \gamma_o \Omega_s}{2K_b T}\right) - 1\right] \tag{4.44}$$

where $\xi_v = (v_x(t)\sin(\phi)\ U(t) + 4D_f/h_a)/h_a$ is the coefficient of free-volume diffusion in EVAM. During the tool-workpiece separation period, the coefficient is expressed as $\chi_v = (4D_f/h_a)/h_a$

Based on the coupled governing Eqs. (4.37), (4.42), (4.43), and (4.44), dimensionless parameters are introduced and defined as temperature $\hat{T} = T/T_o$, shear stress $\hat{\tau} = \tau/\tau_o$, where $\tau_o = 2K_bT_o/\gamma_o\Omega_{stz}$ and $\hat{t} = t/t_o$ with $t_o = e^N/\gamma_v$ and $N = C_s\gamma_c\tau_c\Omega_{stz}/K_bT_o$. The system of governing equations in the dimensionless form is modified as

$$\frac{d\hat{\tau}}{d\hat{t}} = \left\{\left[A_vU_f(t)\right]U(t)\left(\widehat{\gamma_{sv}} - \widehat{\gamma_p}\right)\right\} \tag{4.45}$$

$$\widehat{\gamma_p} = exp\left(N\left\{1 - \frac{(1-P\hat{\tau})^{1.5}}{\hat{T}}\right\} - \frac{1}{\hat{\zeta}}\right) \tag{4.46}$$

$$\frac{d\hat{\zeta}}{d\hat{t}} = \widehat{\xi_v}\left(\zeta_o - \hat{\zeta}\right) + U(t)\,\widehat{\gamma_p}\left\{\frac{\hat{T}}{\hat{\zeta}\Psi}\left[cosh\left(\frac{\hat{\tau}}{\hat{T}}\right) - 1\right]\right\} \tag{4.47}$$

$$\frac{d\hat{T}}{d\hat{t}} = \widehat{\chi_v}\left(1 - \hat{T}\right) + U(t)Q\tau\widehat{\gamma_p} \tag{4.48}$$

where $A_v = mnksin^2\phi_a/\tau_o$, $\widehat{\gamma_p}$ is the dimensionless activation shear strain rate presented in Eq. (4.58), $P = \tau_o/\tau_c$ is a constant, $\widehat{\gamma_{sv}} = [v_c + A_x\omega\cos(\omega t_o\hat{t})]t_o\cos(\alpha)/\cos(\phi - \alpha)\,h_a$, $\widehat{\xi_v} = (V_nU(t) + 4D_f/h_a)t_o/h_a$, $\Psi = v^*S/\tau_o\Omega_{stz}$, $\widehat{\chi_v} = (V_nU(t) + 4k_d/h_a)t_o/h_a$ and $Q = q_{Tq}\tau_o/T_o$. The window functions $U(t)$ and $U_f(t)$ govern the effects of tool-workpiece separation and friction reversal in the EVAM process.

There is no explicit solution for the coupled and nonlinear differential governing equations. Therefore, numerical analysis is performed to predict the periodic variations of the shear stress, temperature, and free volume based on the cutting conditions and the assisted vibration frequencies and amplitudes in EVAM of Zr-BMG.

4.6 Simulation results and analyses

Orthogonal cutting experiments of Zr-BMG were carried to identify the process parameters used in the simulation following the same procedure mentioned in Section 3.6.1. The average chip thickness and cutting forces were measured for an uncut chip thickness ranging from 20 µm to 50 µm at a cutting speed of 8 m/min. The average shear measured without vibration assistance is 37°. The cutting force was used to calculate the coefficient of the friction, $\mu = \tan\beta$=0.466. The material properties used for the simulation are the same as those presented in Table 3.2. The cutting conditions used for the simulations are presented in Table 4.3.

Table 4.3 Process parameters and material parameters used in the simulation.

Cutting condition	Uncut chip thickness - μm	40
	Cutting speeds – mm/min	1-14
Vibration parameters	Frequency kHz	7.5
	Amplitude in cutting direction−μm	6
	Amplitude in feed direction−μm	3
	HSR	0.1, 0.3,0.5,0.7

The variations of shear stress, temperature, and free volume associated with shear band formation in EVAM are predicted by numerically solving the governing Eqs. (4.45), (4.46), (4.47), and (4.48). It is assumed that the thickness of PSZ is 0.15 times the average shear plane length, and tool-chip contact length is assumed to be a constant value of 2 [84]. Figure 4.12 shows the simulation results with HSR values of 0.1, 0.3, 0.5, and 0.7, at an uncut chip thickness of 40 μm. The results illustrate the mechanism of shear localization in EVAM of Zr-BMG. Based on the process parameters, the frequency of shear location ranges from 560 Hz to 3.97 kHz when the HSR increases from 0.1 to 0.7, which is lower than the vibration assistance frequency of 7.5 kHz. In each cycle of shear localization, as the workpiece material moves in to the PSZ, the shear stress increases until the tool-workpiece separation occurs. The shear stress in the PSZ remains constant during the tool-workpiece separation, and then increases further when the tool is in contact with the workpiece. This process repeats in the next vibration cycle, until the shear localization occurs, which results in the drop of shear stress due to the softening effect by free volume aided by temperature increase [108].

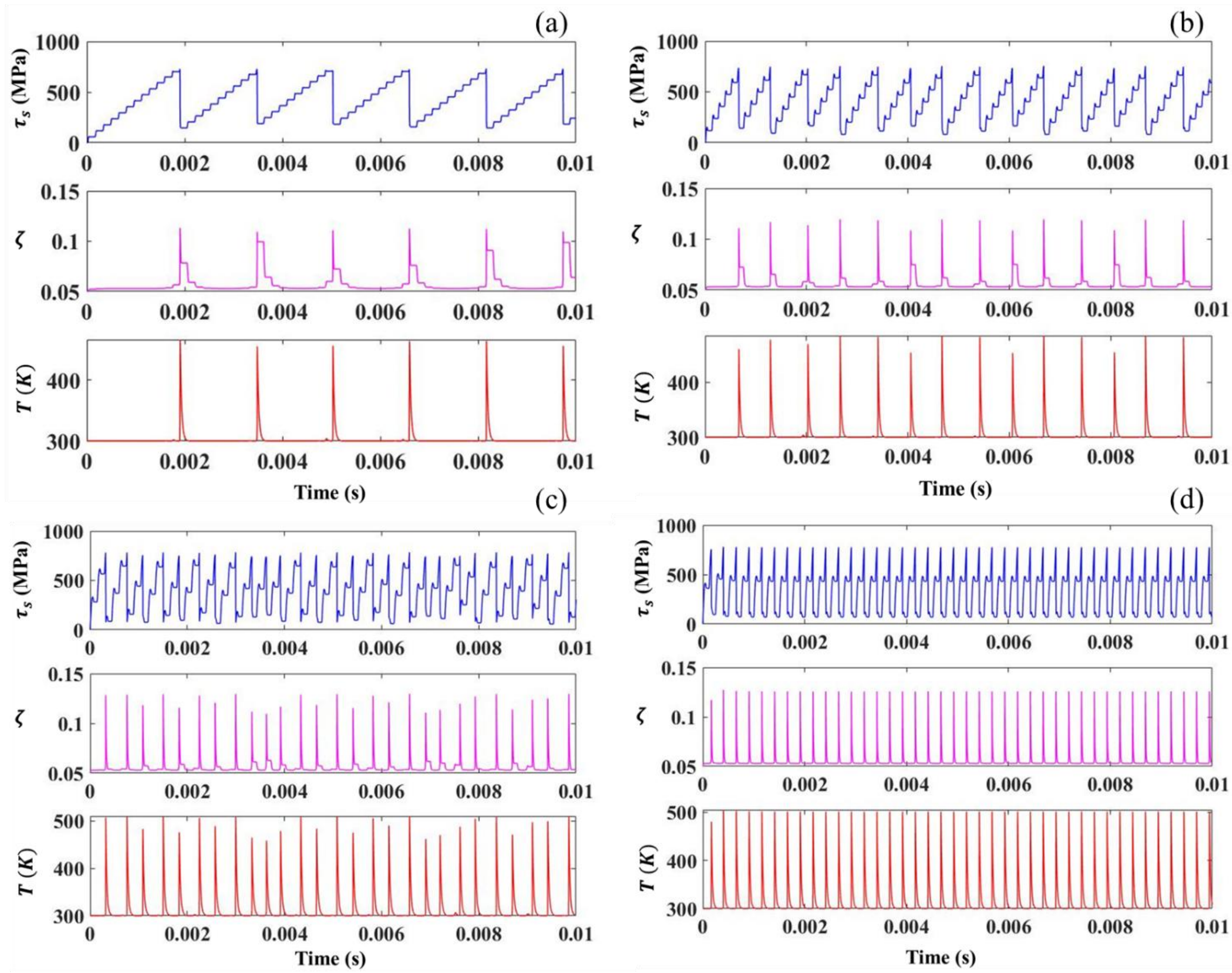

Figure 4.12 The predicted time-domain shear stress (τ_s), free volume (ζ) and temperature (T) with HSR (original cutting speed) in EVAM of Zr-BMG: (a) 0.1 HSR (1.7 m/min), (b) 0.3 HSR (5.1 m/min), (c) 0.5 HSR (8.5 m/min), and (d) 0.7 HSR (11.9 m/min). Uncut chip thickness is 40 μm.

The simulated stress, free volume, and temperature variations at the cutting speeds of 1.7 m/min and 11.9 m/min without vibration assistance are shown in Figure 4.13. The shear band frequency changes from 910 Hz to 5.58 kHz when the cutting speed increase from 1.7 m/min to 11.9 m/min. The comparisons of results in Figures 4.12 and 4.13 show that the segmentation frequency is lower in EVAM compared to machining with no-vibration assistance at the same cutting velocity. The reduction in segmentation frequency is due to the tool-workpiece separation in EVAM. As the frequency of vibration assistance is higher than the chip segmentation frequency, the tool disengages from the workpiece before the initiation of shear localization. The free volume diffusion and heat dissipation during tool-workpiece separation delay the material softening. The differences in the simulated segmented chip frequencies with and without vibration reduce with an increase in HSR value, due to the decrease of tool-workpiece separation period. It is observed that the maximum shear stress before shear localization increases from 720 MPa to 800 MPa when the HSR increases from 0.1 to 0.7. This is due to the effect of strain rate, which increases cutting velocity caused by the increase of HSR value. Similarly, the cutting temperature increases from 440 K to 505 K when the HSR value increases from 0.1 to 0.7.

It is observed that the peak values of free volume and temperature vary with time at lower HSR, as shown in Figure 4.12 (a), (b), and (c). This is due to the fact that the time instance of critical shear stress at which shear localization occurs varies due to tool-workpiece separation. Occasionally, the tool engagement may occur before the shear stress reaches a minimum value at the end of shear localization, or the critical shear stress may be achieved at a different time instance during tool work contact. Due to this phenomenon, there is variation in peak values of temperature, free volume, and minimum values of shear stress. This effect reduces at higher cutting speeds as the tool-workpiece separation time decreases with the increase of HSR value, as shown in Figure 4.12 (d).

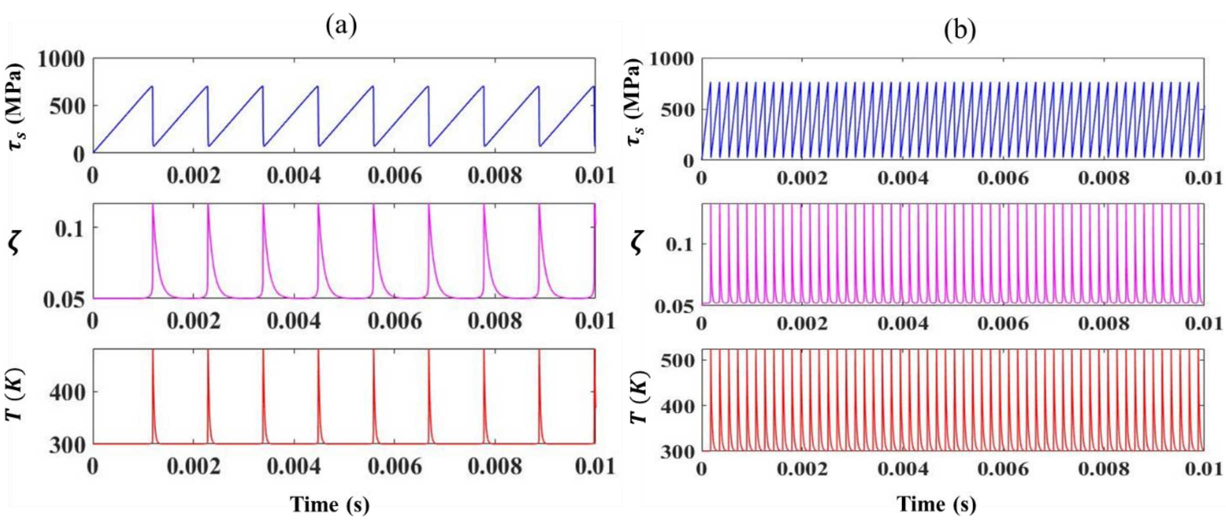

Figure 4.13 The predicted shear stress (τ_s), free volume (ζ) and temperature (T) with respect to cutting time in machining without vibration assistance and 40 µm uncut chip thickness at cutting speed: (a) 1.7 m/min, and (b) 11.9 m/min.

Figure 4.14 shows the dimensionless free-volume and temperature labelled as 'instability index' for comparison purposes. It is observed that the increase of free volume is at a faster rate compared to the increase of temperature. The change of free volume is negligible during the tool-workpiece separation, because the free volume generation and annihilation are stress-driven in metallic glasses [52,56]. In addition, the diffusion of free volume occurs at a lower rate compared to the temperature dissipation, because the value of free volume diffusivity (10^{-16}) is much smaller compared to the thermal diffusivity (10^{-6}). Therefore, heat dissipation occurs at a higher rate compared to the free volume.

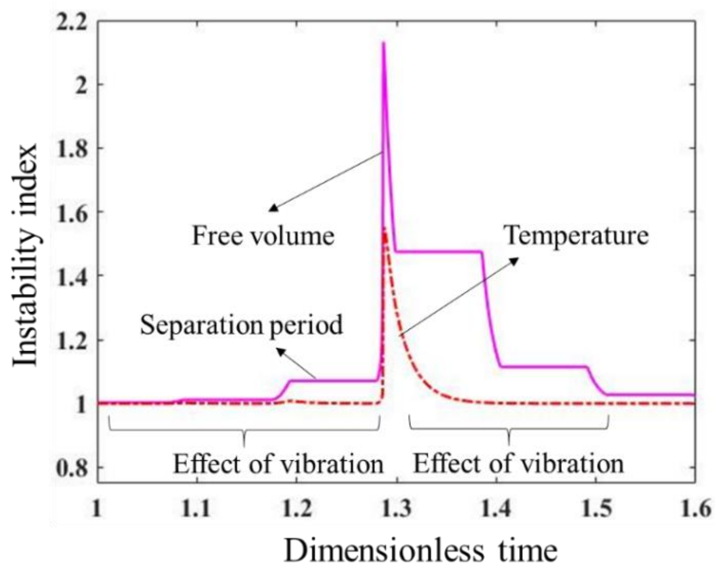

Figure 4.14 Instability index of dimensionless free volume and temperature in EVAM.

The difference of the maximum temperature in EVAM compared to conventional machining reduces with an increase of HSR value, as shown in Figure 4.15. The maximum temperature in EVAM at 0.1 HSR is 440 K, while the maximum temperature in convention machining at the same cutting condition is 486 K. Compared to conventional machining, the temperature dissipation in EVAM occurs for a more extended time due to tool work separation, resulting in a lower value of the temperature. The difference in temperature generated in PSZ between EVAM and CT reduces as the HSR value increases.

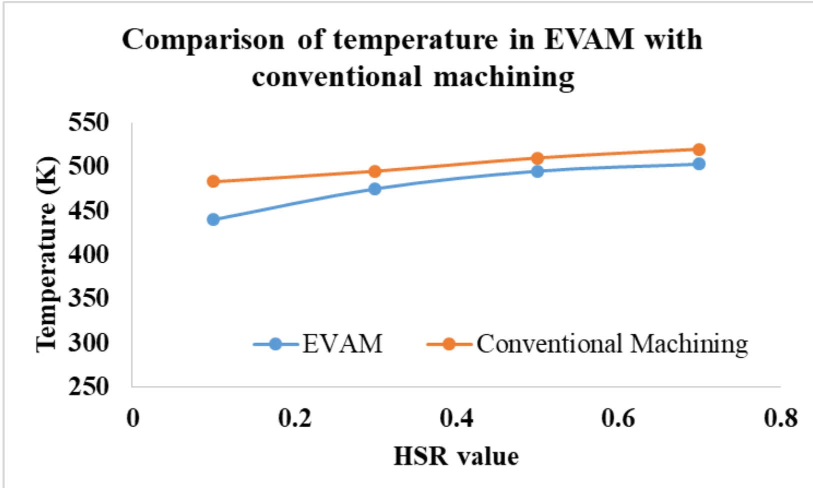

Figure 4.15 Comparison of simulated maximum temperatures in EVAM of Zr- BMG with and without vibration assistance.

4.7 Conclusions

In this chapter, a new mechanics model is developed to investigate the fundamental mechanism of chip formation in EVAM. The model emphasizes the effect of vibration assistance on the chip segmentation in EVAM of Zr-BMG.

A physics-based model is developed to predict the shear angle with respect to HSR in EVAM. It was observed that the change of shear angle in EVAM significantly depends on material hardening behaviour as well as the vibration parameters. The simulation results show that materials with obvious strain hardening property show an increase of shear angle as the HSR value decreases, e.g., aluminum alloys. The cutting forces are predicted based on the developed kinematics and mechanics model, and are compared with the FE simulation results due to the bandwidth limit of the dynamometer in experiments.

However, the variation of shear angle in EVAM of Zr-BMG at different HSR values is negligible, as Zr-BMG does not have obvious strain hardening property. The mechanics model of EVAM of Zr-BMG focuses on the effects of tool-workpiece separation and friction reversal on the variation of the shear stress, temperature, and free volume. The results show that the vibration assistance reduces the chip segmentation frequency and reduces the cutting temperature due to tool-workpiece separation. The shear localization in EVAM of Zr-BMG is primarily controlled by free volume and aided by thermal instability. The shear localization in EVAM is delayed due to heat dissipation and negligible change in free volume during tool-workpiece separation compared to machining with no vibration assistance. The temperature generation is lower in EVAM than without vibration assistance, and the difference reduces with an increase in HSR value. Experimental studies on chip formation in EVAM of Zr-BMG, and the comparison between the simulated and experimental results of shear angle and chip segmentation are discussed in detail in Chapter 5.

Chapter 5

Experimental Studies on EVAM of Zr-BMG

5.1 Overview

In this chapter, experimental investigations on EVAM of Zr-BMG are performed to determine the effect of the vibration assistance on chip formation. A 2-D vibration stage is developed to achieve the elliptical vibration trajectory required for EVAM experiments. The design of the vibration stage, the testing, and the analysis of the stage dynamics are presented. The experimental validation and comparison with the simulation results of shear angle in EVAM of Al 6061 and Zr-BMG are conducted. The chip segmentation frequency and the average temperature results are further analyzed to determine the effect of elliptical vibration assistance parameters on chip segmentation in EVAM of Zr-BMG.

5.2 Development of 2-D vibration stage[2]

This Section describes the 2-D vibration stage development to impose vibration assistance on the cutting tool during the machining process. Various actuation systems have been developed in the literature to achieve vibration assistance with frequency ranging from 500 Hz to 40 kHz, and amplitude (A_{pp}) ranging from 1 μm to 20 μm. The assisted vibration below 2 kHz is achieved mainly using electromagnetic actuators, and a higher frequency above 2 kHz is generally achieved using piezo actuators. Chen et al. [109] developed a 2-D vibration stage with a maximum frequency of 2 kHz and 10 μm amplitude for the vibration-assisted milling process. Uhlmann et al. [110] developed a workpiece holder to achieve the vibration with a maximum frequency of 10 kHz and 7.5 μm peak to peak amplitude. Jin and Xie [111] developed a 2-D vibration stage to achieve the vibration assistance with a maximum frequency of 8 kHz and a peak-to-peak amplitude of 10 μm. Considering the 1-D kinematic of VAM, it should be noted that periodic separation of tool-workpiece occurs only when the vibration velocity exceeds the original cutting velocity. For

2. A partial content of the chapter 5 has been published in a Journal article: Wan, S., Maroju, N. K., Jin, X., 2019, Development of a 2-D Vibration Stage for Vibration-Assisted Micro Milling, Instrumentation, 6 (1), 98-108.

a given vibration signal $x(t) = Asin(\omega t)$, the velocity of vibration assistance is given by $x'(t) = A\omega cos(\omega t)$, where ω is the angular frequency equal to $2\pi f$, that f is the frequency of vibration. The condition for separation is $2\pi f A > V_c$, where V_c is the original cutting velocity. Therefore, a vibration stage with high operating frequency and amplitude is desired.

5.2.1 Design of mechanical structure

In this thesis, a new 2-D vibration stage is developed to achieve an elliptical vibration trajectory. The structure of the 2-D vibration stage is shown in Figure 5.1. Two piezo actuators from Physik Instrument (PI) are used to excite the system in each direction, and the specifications of the piezo actuators are presented in Table 5.1. The piezo actuators transfer the vibration signal to the flexible vibrating structure of the stage. End mass is used to assemble the piezo actuator in the setup and to act as preload. The cutting tool's trajectory is controlled by the vibration amplitude, frequency, and phase difference between the two actuators. The mechanical design is based on a flexural hinge system. Circular hinge profiles are used on the flexure, with extension in the direction of load and rotation perpendicular to the load direction. The size of the hinge depends on the required frequencies and amplitude of the excitation. There is always a tradeoff between the maximum frequency that can be achieved and the vibration's amplitude. Three layers of flexural hinges are distributed symmetrically in both directions to minimize the cross-coupling effect. The guiding structure acts as a mechanical connection between the piezo and the vibration stage's flexure.

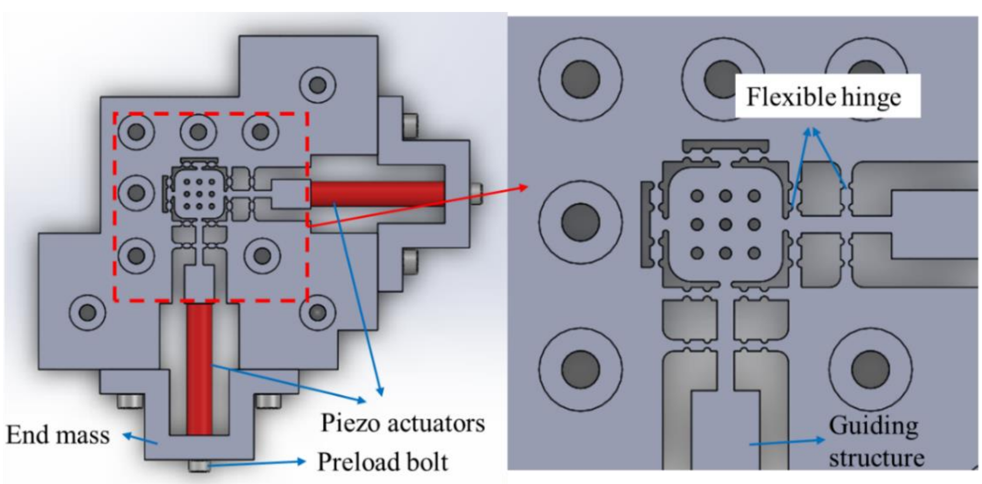

Figure 5.1 The CAD model of the designed 2-D vibration stage showing the flexural hinges.

Table 5.1 Specifications of the piezo actuators used in the design.

Piezo actuator	P-010.40H (PI)	Resonant frequency	21 kHz
Travel range	50µm	Capacitance	182 nF
Length	54 mm	Operating voltage	0~1000V
Maximum blocking Force	1,800N	Inner Diameter	5 mm
Stiffness	29 N/µm	Outside diameter	10 mm

To evaluate how the hinges' geometric parameters influence on the vibration stage dynamics, the three-layer flexure system is approximated by the torsional spring system, as shown in Figure 5.2. The primary factor which influences the motion of the hinge is its torsional stiffness. In order to obtain an equivalent stiffness of the flexure system in the direction of applied force, it is assumed that the torsional stiffness K_θ is equal at each node, which depends on the flexural hinge dimensions, as shown in Figure 5.2 (a) [112].

$$K_\theta = \frac{Ebr^2}{12\left[\frac{2s^3(6s^2+4s+1)}{(2s+1)(4s+1)^2} + \frac{12s^4(2s+1)}{(4s+1)^{5/2}} tan^{-1}\sqrt{4s+1}\right]} \tag{5.1}$$

where E is the elastic modulus of the flexure hinge material, r is the radius of circular hinge, t is the thickness, b is the breadth of the hinge, and s is the ratio of radius to the thickness, $s = r/t$ as shown in Figure 5.2 (b).

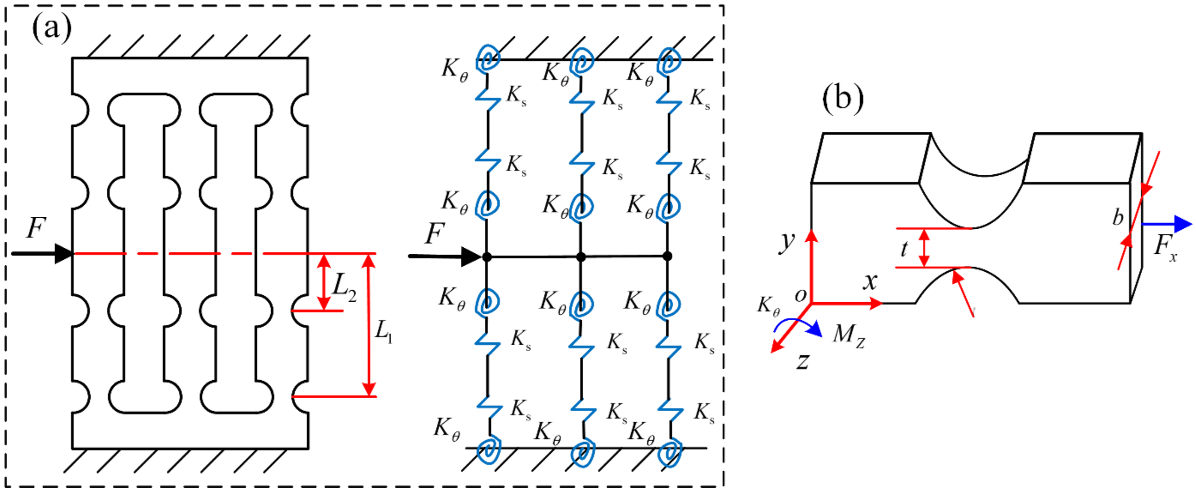

Figure 5.2 (a) Approximation of flexural system in one direction, and (b) circular flexure hinge.

In order to obtain the linear stiffness of the whole flexural system, an external force F is assumed to be applied, which generates a displacement of Δs. The work done by the force is equal to the total potential energy of the torsional springs. The total potential energy W_p of the system is expressed as

$$W_p = \sum_{i=1}^{12} W_{\theta i} \tag{5.2}$$

where $W_{\theta i}$ is the stored energy of each torsional spring given by

$$W_{\theta i} = \frac{1}{2} K_{\theta i} \theta^2 \tag{5.3}$$

and θ is given by

$$\theta = \frac{\Delta s}{L_1 - L_2} \tag{5.4}$$

The work W_k done by the external fore F to produce a displacement Δs is given by

$$W_k = \frac{1}{2} F \, \Delta s \tag{5.5}$$

Therefore, equating the work and energy $W_p = W_k$, the equivalent linear stiffness of the flexural system in the direction of motion is given by

$$K_e = \frac{F}{\Delta s} = \frac{12K_\theta}{(L_1 - L_2)^2} \tag{5.6}$$

The stiffness of the piezoelectric actuator is K_p, then the relationship between the displacements of the vibration stage and the piezoelectric actuator is expressed as

$$\Delta L_o = \Delta L \frac{K_e}{K_e + K_p} \tag{5.7}$$

where ΔL_o and ΔL are the maximum displacement of the system and the maximum stroke from the piezo actuator, respectively. Table 5.2 presents the dimensional parameters of the designed flexible mechanism. The material of the designed vibration stage is Al 7075 with an elastic modulus of 71.7 GPa. From Eqs. (5.1) and (5.6), the stiffness of the designed flexible mechanism in each direction is 63.7 N/μm. From Eq. (5.7) and the selected piezoelectric actuator parameters, the maximum displacement which the stage can achieve is determined as 15.5 μm. A maximum of 31 μm peak to peak amplitude can be achieved during the operation with no external load. The natural frequencies and the assembled structure's mode shapes, including the piezo actuators and the end mass, are evaluated using FE analysis due to the complexities of the actual structure. The natural frequencies are presented in Table 5.3.

Table 5.2 Geometric parameters of the designed flexible mechanism.

Parameters	b	r	t	L_1	L_2
Value (mm)	17	0.725	0.8	6.775	3.225

It was observed that the first natural frequency of the system is about 7.8 kHz, and the second natural frequency is about 16.3 kHz. The first natural frequency is observed to excite the guiding structure, which transfers the signal to the four-bar flexure hinge, and the second natural frequency is observed to excite the entire system, including the vibration stage and flexure hinges.

Table 5.3 Mode shapes and natural frequencies of the vibration stage assembly.

Frequency	Mode shape
7.8 kHz	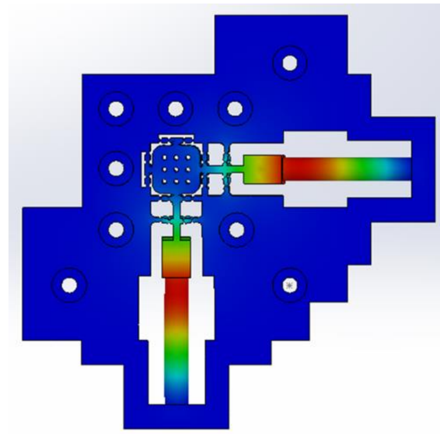
7.8 kHz	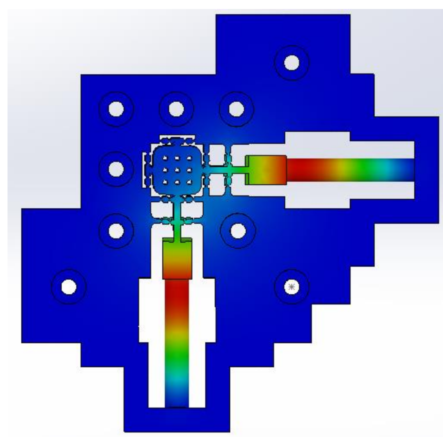
16.3 kHz	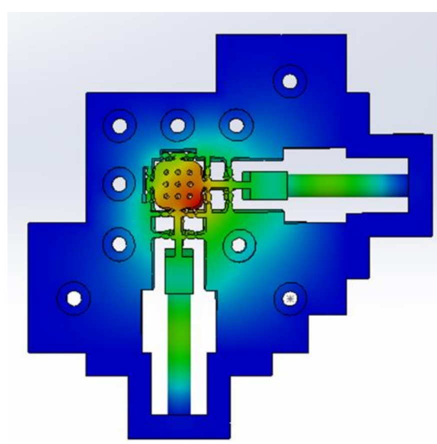

5.2.2 Selection of amplifier

To achieve a steady vibration output at high frequency and amplitude, an amplifier that can provide high voltage and current to the piezo-actuator at the desired frequency range is required. The piezo actuator is represented by a capacitive load. Most commercial amplifiers cannot meet a bandwidth of 20 kHz at a high AC voltage of 200 V for a given capacitive load of 0.18 μF, while some specialized amplifiers with high bandwidth capability usually have a high cost. The range of frequencies at which the amplifier can operate is limited by the output power and the capacitive load. In this study, a low-cost amplifier is developed to achieve steady vibration assistance to the workpiece, and to meet the high-frequency bandwidth of 30 kHz and a high AC voltage of 400 V. The limit of the operational frequency of the amplifier is defined as the slew rate, expressed as

$$SR \geq 2\pi f V_p \tag{5.8}$$

where f is the operating frequency, and V_p is the peak amplitude of the output voltage. For a 20 kHz operating frequency at an operating voltage of 90 V, the amplifier's slew rate should be larger than 12.6 V/μs. The maximum current output required at an operating frequency is given by

$$I_o = V_p 2\pi f C_l \tag{5.9}$$

where C_l is the capacitive load. The required maximum current is 2.058 amp to drive the amplifier. The maximum power of the amplifier is given by

$$P_w = 4\, V_p^2 f C_l \tag{5.10}$$

The maximum power required to drive the amplifier should be greater than 118 W at a rated frequency of 20 kHz and a capacitive load of 182 nF. To meet the power and current requirement, a power operational amplifier module (MP118FD, Apex Microtechnology) and an evaluation kit EK57 are selected for the piezo actuator. The maximum output voltage V_{pp} is 200V, and the slew rate (SR) is 80 V/μs, which meets the requirement of the frequency limit. Figure 5.3 (a) shows the amplifier's circuit diagram and the piezo actuator as a capacitive load. R_i and R_f are the input resistor and feedback resistor, respectively, which determine the gain of the amplifier. In this design, 475 Ω and 9.7 kΩ are used for R_i and R_f to achieve a gain value higher than 20.

The piezoelectric actuator generates a reverse voltage at high frequency due to the expansion and compression of the piezo-element during the operation. A fast recovery diode is used to prevent the reverse voltage from reaching the amplifier. Two SUR1560 ultrafast rectifier diodes (D_1 and D_2) are used to compensate the reverse current, as shown in Figure 5.3 (a). To improve the stability of the circuit, an isolation resistor annotated by R_s is connected between the output of the amplifier and the piezoelectric actuator. The resistance of R_s is selected based on the crossover frequency of the RC circuit (constructed by the piezoelectric actuator and isolation resistor). For an RC circuit, the phase is -45° at the crossover frequency. The cross over frequency of the RC circuit is $1/(R_s C_l)$. In the design, a crossover frequency value greater than 1 MHz is chosen to ensure the phase margin at 20 kHz for the whole circuit (output of the amplifier and RC circuit) is greater than or equal to 60°. Therefore, the resistance of R_s should be less than 12 Ω, then an isolation resistor with 7.5 Ω (model TO220, Ohmite) is selected to ensure the operating frequencies at about 30 kHz. To maximize the output voltage acting on the piezo actuator, two amplifiers are bridged together such that the operating voltage is as high as 400 V (peak to peak).

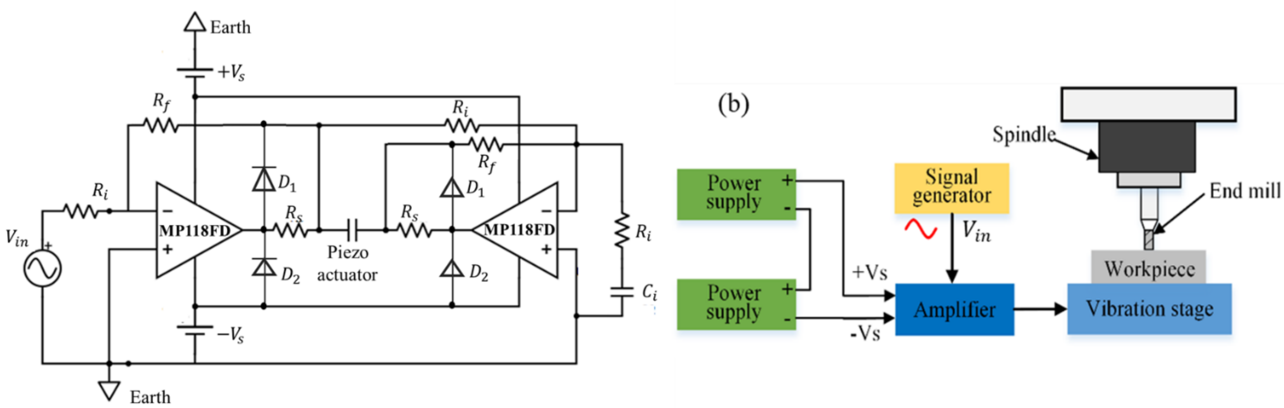

Figure 5.3 (a) Circuit diagram of the amplifier, and (b) schematic representation of the setup of the amplifier and vibration stage.

The amplifier is bipolar, which requires both positive and negative DC supplies to drive the amplifier. Two high-voltage DC power supplies (Sorensen XG 300-5) are used to supply a DC positive voltage ($+V_s$) and negative ($-V_s$) to drive the amplifier. A signal generator is used to provide the input control signal to the amplifier, and then the input voltage is amplified at the rate of the input frequency to drive the piezoelectric actuator and generate the vibration motion on the stage.

5.2.3 Experimental test to identify the vibration stage dynamics

Figure 5.4 shows the experimental setup to test the designed vibration stage and amplifier. A dual-channel signal generator (BK-Precision 4053B) is used to provide a sinusoidal input signal for the amplifier. A laser vibrometer (Polytech CLV-2534) is utilized to measure the vibration of the workpiece fixed on the vibration stage, and a National Instruments data acquisition system (DAQ) is used to acquire the data of vibration from the laser vibrometer. A frequency sweep test is performed to measure the vibration stage's maximum achievable amplitude at different frequencies. A sinusoidal signal with an amplitude of 8.5 V (peak to peak) is generated to the amplifier, such that the amplified voltage acting on the piezo actuator is 340 V. The frequency varies from 1 kHz to 12 kHz within 1.5 s in linear sweep mode. Figure 5.5 (a) shows the vibration response in the time domain with a maximum amplitude of 44 μm (peak to peak) at a frequency of 7.5 kHz. Fig. 5.5 (b) illustrates the spectrum of the measured vibration response. The frequency at which the largest vibration amplitude is achieved is 7.47 kHz. The amplitude of the vibration stage can be controlled by varying the output voltage of the amplifier. The bandwidth of the designed amplifier is about 24 kHz. Therefore, it is demonstrated that the maximum amplitude of the vibration stage is 22 μm at 7.47 kHz with no external force. The achievable frequency and the amplitude of the vibration stage depend on the workpiece's mass, and the preload applied on the piezo actuator [113]. The developed vibration stage is used to analyze the effect of vibration assistance on the chip formation in EVAM of Zr-BMG.

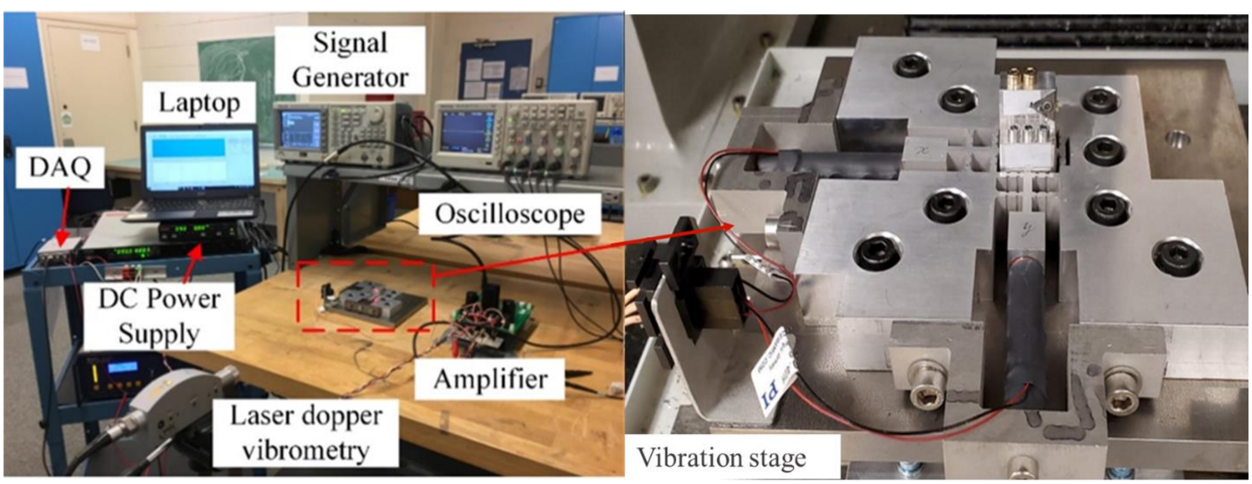

Figure 5.4 Experimental setup to test the designed 2-D vibration stage.

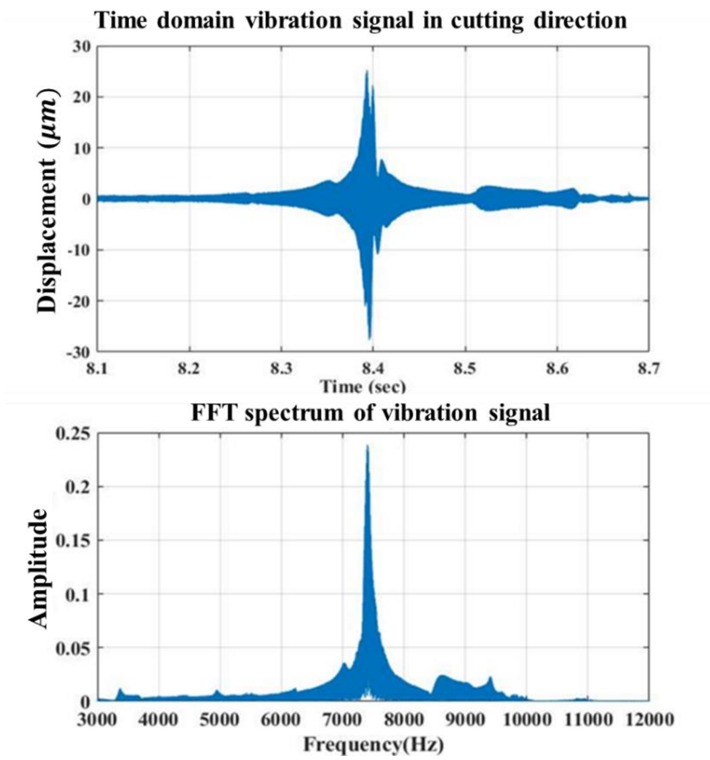

Figure 5.5 (a) Time-domain vibration signal, and (b) FFT spectrum of the time-domain vibration signal.

5.3 Experimental validation of shear angle prediction for EVAM

Orthogonal EVAM experiments were conducted on a 3-axis precision machining center (Mikrotools DT-110). The schematic of the experimental setup and the enlarged view (A) of EVAM are presented in Figure 5.6. A customized SCD tool was used, and the workpiece materials include Al-6061 and Zr-BMG. The 2-D vibration stage was used to generate the elliptical trajectory on the workpiece. A Laser vibrometer (Polytech CLV-2534) was used to measure the cutting tool's vibration amplitude, which is fixed to the tool holder on the vibration stage to ensure the amplitude of vibration is the same before and during cutting. National Instruments data acquisition system was used to acquire the data at a sampling rate of 2.5 MHz. The measured tool trajectory in cutting and feed directions during the cutting process is presented in Figure 5.7 to ensure the phase difference is 90°. The experimental conditions are presented in Table 5.4. An Infrared thermal camera (Flir A5753-SC) was used to measure the cutting region's average temperature. SEM examination on the chip thickness and the segmentation spacing was performed by Hitachi SU 3500.

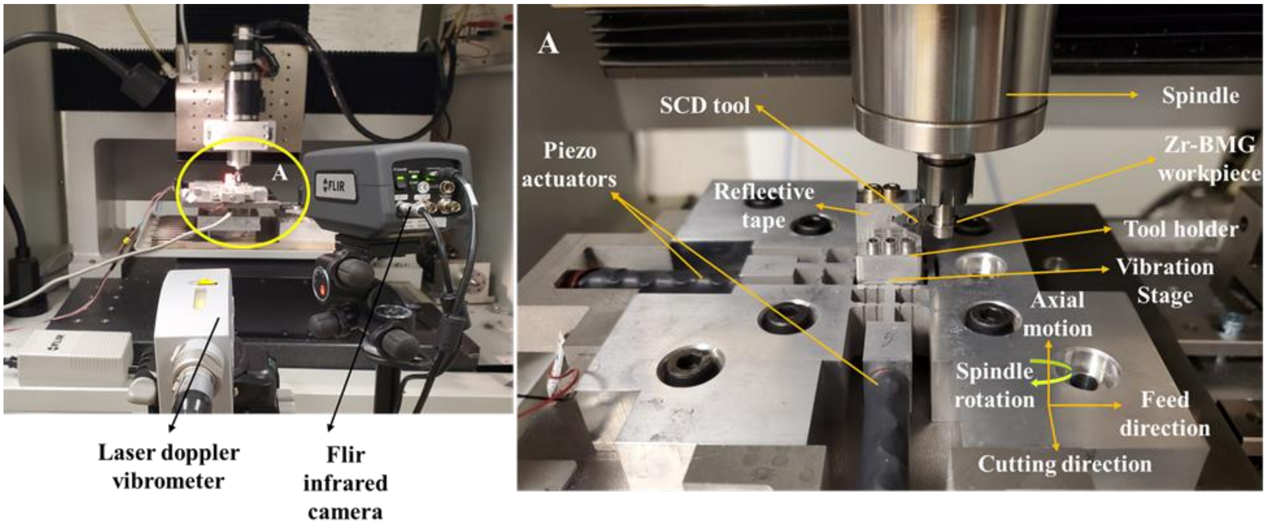

Figure 5.6 Experimental setup for EVAM process.

Table 5.4 Experimental conditions of EVAM process.

Process parameters		
Workpiece material	Al 6061	Zr-BMG
Uncut chip thickness (h_{un})	20 μm	40 μm
Width of cut (b)	0.9 mm	0.8 mm
Cutting speed (V_c)	1.2, 3.4, 6.8, 8.5, 10.2, 12.75 m/min.	1.7, 5.1, 8.5, 12 m/min.
Rake angle	0°	0°
Clearance angle	7°	7°
Vibration parameters		
Frequency of vibration (f)	7.5 kHz	
Amplitude in cutting direction (A_x)	6 μm	
Amplitude in feed direction (A_y)	3 μm	
Phase difference (φ)	90°	
HSR	0.07,0.2,0.4,0.5,0.6,0.75	0.1, 0.3, 0.5, 0.7

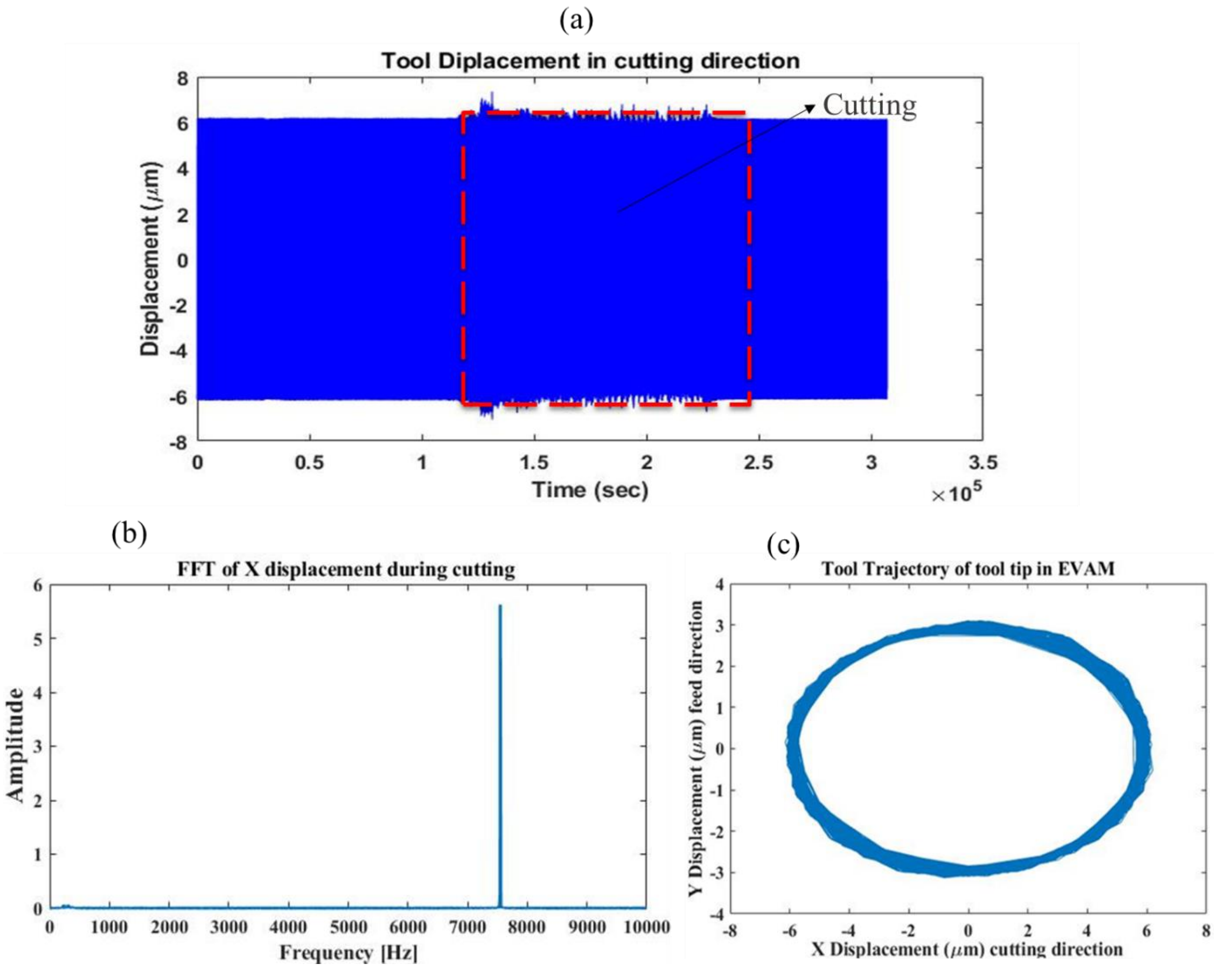

Figure 5.7 (a) Displacement in cutting direction during cutting in time domain, (b) FFT spectrum during cutting, and (c) tool tip amplitude in x- and y- directions during cutting.

The chip thicknesses in machining Al 6061 were measured to calculate the shear angle under different HSR values. For an uncut chip thickness of 20 μm and cutting speed range of 1.1 to 12.75 m/min, the experimentally measured chip thicknesses at various HSR values of 0.07, 0.2, 0.4, 0.5, 0.6, and 0.75 are presented in Figure 5.8. It was found that the measured chip thickness values increase with the HSR values. The shear angle values in EVAM are determined based on the chip compression ratio and the tool rake angle, expressed as

$$\tan(\phi) = \frac{\frac{h_{un}}{h_c}\cos(\alpha)}{1 - \frac{h_{un}}{h_c}\sin(\alpha)} \tag{5.11}$$

where h_c is the measured chip thickness and h_{un} is the uncut chip thickness.

To predict the shear angle from the mechanics model, the mechanical properties of Al6061 used in the experiments, including A_o and B_o need to be identified. The yield shear strength (A_o) is 207 MPa, and B_o is identified based on the cutting experiments without vibration assistance, when the uncut chip thickness ranges from 10 µm to 50 µm. The measured shear angle without vibration assistance is 14.8°±2°, and the corresponding shear strain is calculated by $\gamma = \cot(\phi) + tan(\phi - \alpha)$. The measured shear strength (τ) is 387$\pm$20 MPa (Appendix 2), and B_o is identified from Eq. (4.14) as 55 MPa. Based on the mechanical properties of Al 6061, the mechanics model in Chapter 4 predicts the shear angles with HSR values in the EVAM process. The comparison between the simulated and experimental results of the shear angle in EVAM of Al 6061 is shown in Figure 5.9 with different HSR values and an uncut chip thickness of 20 µm. The results show that both the mechanics model and the experiment prove the decrease of the shear angle when the HSR value increases. The simulations and the experimental results are closer when HSR is in the range between 0.05 – 0.5, and the difference is larger when the HSR value increases further. However, EVAM with HSR values lower than 0.5 is generally used in practice, as higher HSR values result in a wavy surface with surface roughness value larger than vibration amplitude in the feed direction, and it is not the focus in this study [67].

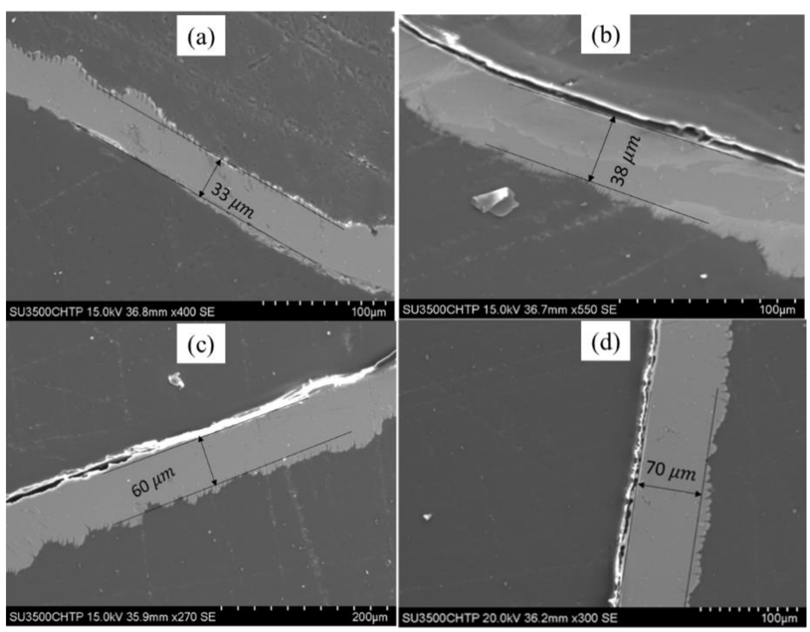

Figure 5.8 Measured chip thickness values in EVAM of Al 6061 for uncut chip thickness of 20 μm and HSR values of (a) 0.07, (b) 0.2, (c) 0.5, and (d) 0.7.

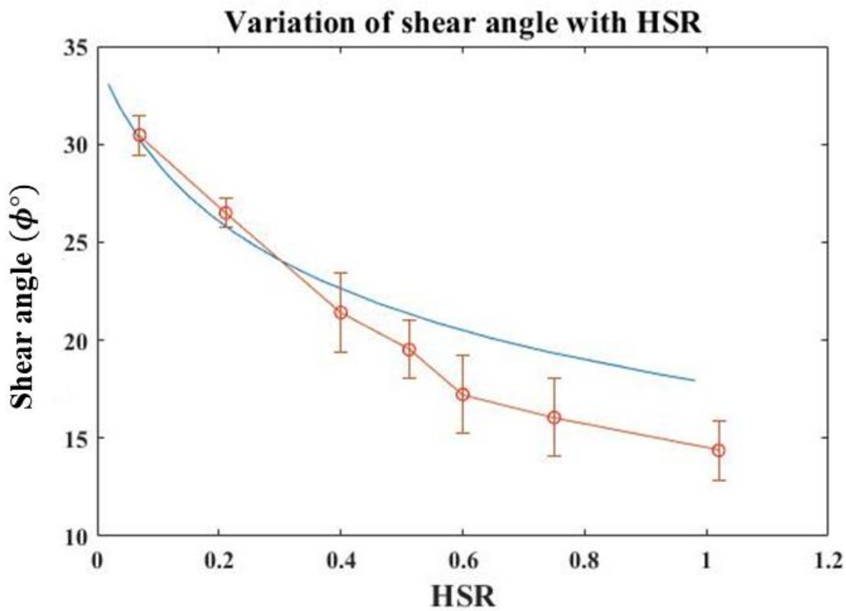

Figure 5.9 Variation of shear angle with HSR in EVAM of Al 6061.

Similarly, the EVAM experiments were conducted to measure the shear angle for Zr- BMG for an uncut chip thickness of 40 μm with the HSR values of 0.1, 0.3, 0.5, and 0.7. As segmented chip formation occurs in Zr-BMG, average chip thickness is used to measure the shear angle, as shown in Figure 5.10. It should be noted that Figure 5.10 represents only one of the measurements presented, and the shear angle is calculated from the average of five measurements. The figure shows that the minimum and the maximum chip thicknesses are around 30 μm and 70 μm respectively, for all of the four HSR values. The average chip thickness measured was 50±6 μm, and the determined shear angle is 37°±5°. The change of shear angle is negligible for varying HSR values in EVAM experiments of Zr-BMG. Therefore, the experimental results prove that the HSR value does not cause a noticeable variation of the shear angle in EVAM of Zr-BMG.

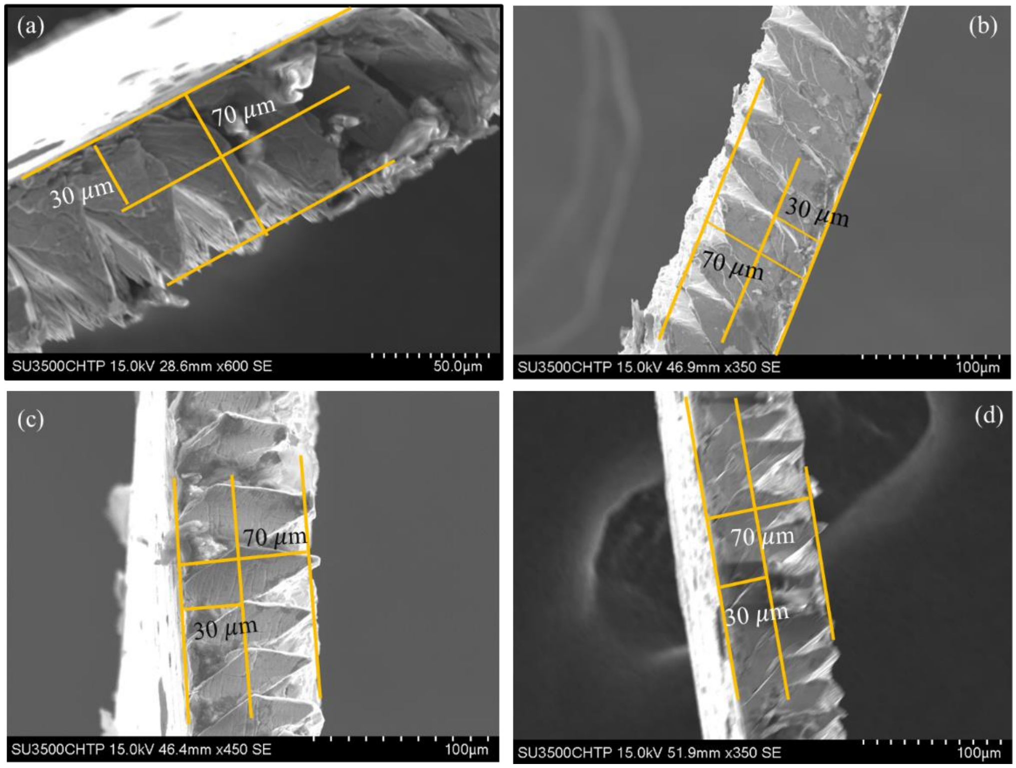

Figure 5.10 Measurement of shear angle in EVAM of Zr- BMG at: (a) 0.1 HSR, (b) 0.3 HSR, (c) 0.5 HSR, (d) 0.7 HSR and 40 μm uncut chip thickness.

5.4 Experimental validation of chip formation in EVAM of BMG

Further experimental examinations on the shear band spacing of the machined chips are conducted to determine the effect of vibration assistance on the shear localization and chip segmentation in the EVAM of Zr-BMG. Figure 5.11 shows the SEM images of chip morphologies when HSR increases from 0.1 to 0.7. The average length of four segments measured at ten different locations is reported, and Figure 5.11 shows one of the ten measurements to reduce redundancy. L_p is the average pitch length of each chip segment along the rake face. The average segmentation length along the normal direction to the shear plane is calculated as $L_p \cos(\phi - \alpha)$. The chip velocity normal to the shear plane varies with time in EVAM process, and needs to be determined based on the HSR value. By neglecting the ploughing region, the relative tool-workpiece displacement in cutting direction in each vibration cycle is $2\pi A_x HSR$. The relative chip displacement normal to the shear plane is obtained as $2\pi A_x HSR\ sin\phi$. For example, the maximum value of relative chip displacement at 0.7 HSR is approximately 13 μm, which is far below the average pitch length (34 μm) of the chip from the experimental measurement, meaning that the tool leaves the workpiece even before one segment is formed. Therefore, the average chip flow velocity in the normal direction given by $v_n = v_c \sin(\phi)$ is used to evaluate the segmentation frequency, expressed as

$$f_{sv} = \frac{v_n}{L_p \cos(\phi - \alpha)} \tag{5.12}$$

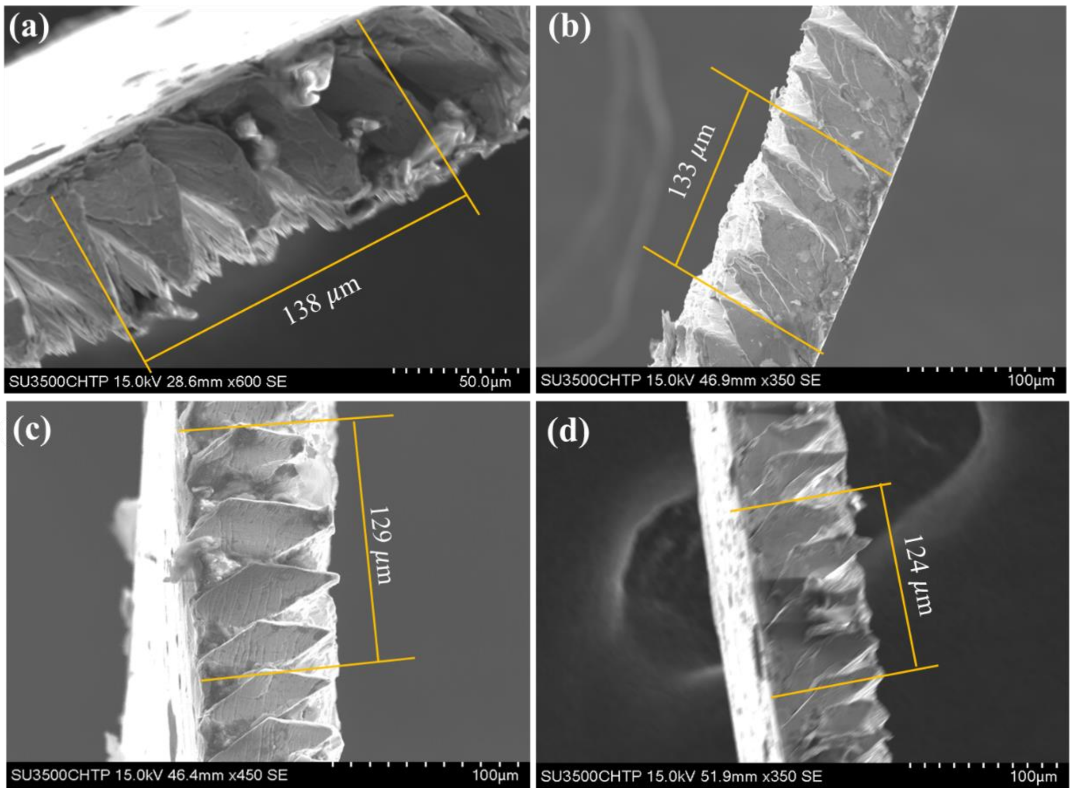

Figure 5.11 Segmented chip formation at: (a) 0.1 HSR, (b) 0.3 HSR, (c) 0.5 HSR, (d) 0.7 HSR and 40 µm uncut chip thickness.

Table 5.5 presents the comparison of the simulated and experimental segmentation frequencies under different HSR values. It was observed that the simulations are able to capture the trend of the chip segmentation frequency with respect to the HSR values, and the differences between the simulated and the experimental values are below 17%. The primary reason for the deviation is due to the assumption of the shear plane thickness and tool-chip contact length, which cannot be measured directly. In addition, the material parameters, including activation energy and diffusion coefficients are temperature dependent; however, they are assumed to be constant in this thesis to simplify the model and the simulations.

Table 5.5 Comparison of chip segmentation frequency in simulation and experiments.

Cutting condition			**Frequency from simulations (Hz)**	**Frequency from experiments (Hz)**
Uncut chip thickness (μm)	HSR	Cutting speed (m/min)		
40	0.1	1.7	560	473±55
	0.3	5.1	1,610	1,460±87
	0.5	8.5	2,730	2,530±165
	0.7	11.9	3,970	3,770±212

Furthermore, the predicted temperatures from the mechanics model are compared with the experimentally measured temperature of the chip in EVAM of Zr-BMG using an infrared camera. It should be noted that the measurement of the instantaneous increase of temperature during the shear band formation is challenging, because of the limitations of the spatial resolution and sampling frequency of the infrared camera. The maximum frame rate at which the data is captured depends on the temperature range and the camera's resolution. In the experimental setup, the temperature was measured at a frame rate of 128 Hz, which is lower than the chip segmentation frequency and the assisted vibration frequency. The thermal emissivity of the Zr-BMG is set to be 0.18 [114]. Therefore, instead of the instantaneous value, the average temperature obtained from the simulations and the experiments are compared. The experimental setup and the measured average temperature in the cutting zone at 0.1 HSR value are presented in Figure 5.12. Similarly, the temperature was measured for HSR values of 0.3, 0.5, and 0.7. The comparison between the predicted average temperature in the shear band and the experimentally measured average temperature at various HSR values are presented in Figure 5.13. There is an approximate error of 22% compared to experimental values, which is due to the limitations of measuring methods such as frequency of measurement and spatial resolution.

Overall, both the simulations and experimental results show an increase in temperature when HSR increases. The comparison of the average temperature with (0.1 HSR) and without vibration assistance at a cutting speed of 1.7 m/min is shown in Figure 5.14. The percentage reduction of temperature in EVAM is approximately 23% compared to machining without vibration assistance.

The difference in temperature generated in PSZ between EVAM and CT reduces as the HSR value increases. The tool-workpiece separation reduces the temperature generation in PSZ during EVAM due to heat dissipation, as explained in Section 4.6. The increase of temperature is below the glass transition temperature (673 K), which indicates the material is still in amorphous state. From the experimental results of chip segmentation and the temperature, it is demonstrated that the developed mechanics model can predict the effect of vibration assistance on chip formation and temperature in the PSZ in EVAM of Zr-BMG with acceptable accuracy.

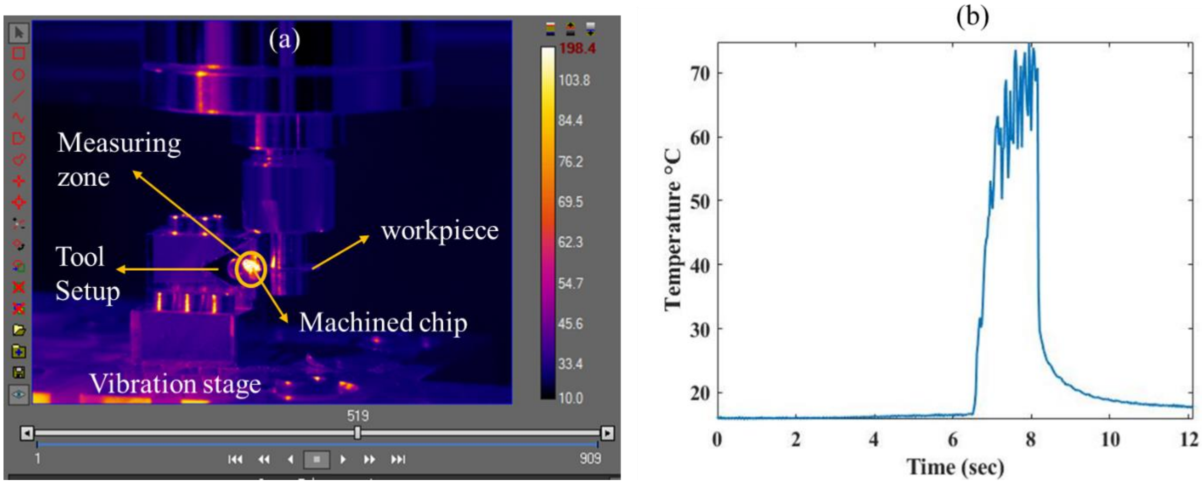

Figure 5.12 (a) Experimental setup of temperature measurement, and (b) measured average temperature in EVAM at 0.1 HSR value.

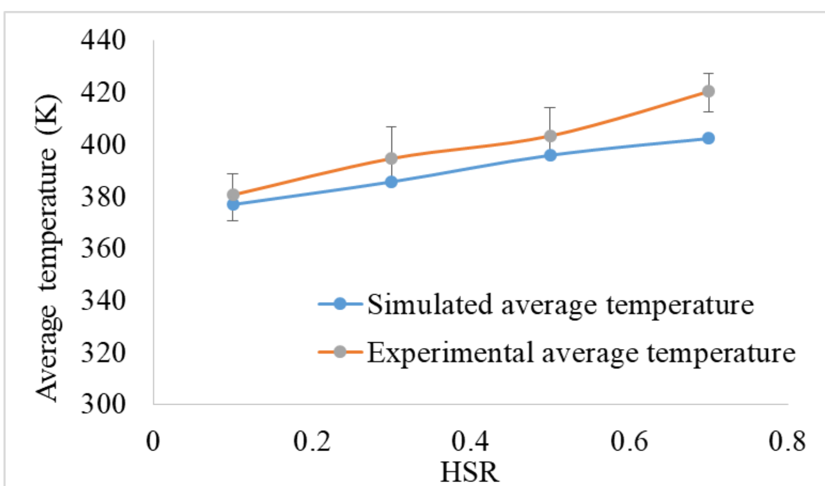

Figure 5.13 Comparison of simulated and experimentally measured average temperature at various HSR values.

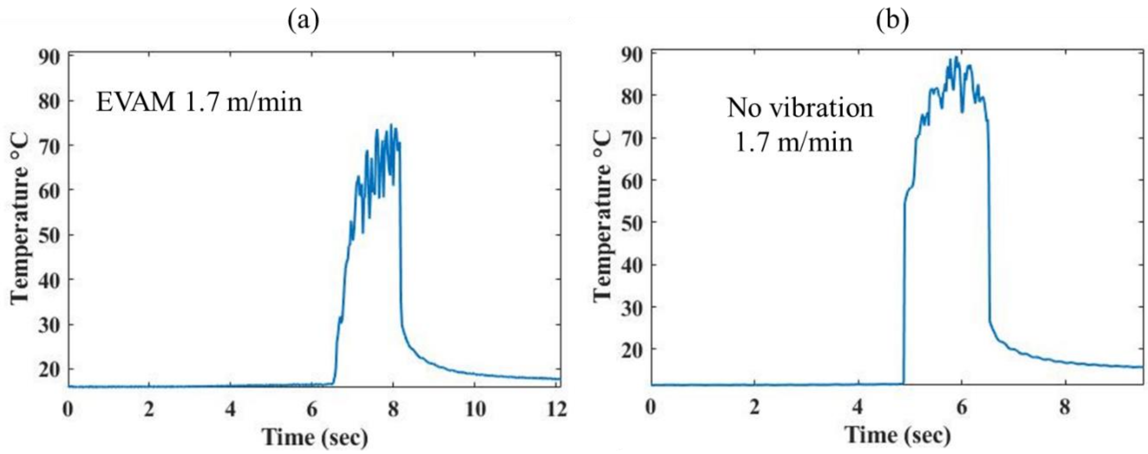

Figure 5.14 Comparison of the measured temperature at the cutting speed of 1.7 m/min (a) EVAM, and (b) without vibration assistance.

5.5 Conclusions

In this chapter, experimental investigations are performed to determine the chip formation mechanism in EVAM process. A 2-D vibration stage and a high voltage amplifier are developed to achieve elliptical vibration assistance at an operating frequency of 7.5 kHz with a vibration amplitude of 44 µm (peak-peak). The chip morphology through SEM examination shows that the shear angle decreases with the increase of HSR in EVAM of Al 6061, while the shear angle variation is not obvious at different HSR values in EVAM of Zr-BMG. This result proves the shear angle prediction from the mechanics model of EVAM in Chapter 4, that the shear angle variation in EVAM depends on the strain hardening property of the workpiece material.

The effect of vibration assistance on the chip segmentation in EVAM of Zr-BMG is also determined experimentally. The results show that the vibration assistance reduces the chip segmentation frequency compared to cutting without vibration assistance. The mechanics model of EVAM of Zr-BMG in Chapter 4 is validated by comparing the chip segmentation frequencies between the simulations and the experimental results at different HSR values. The average temperature measured from the experiments shows the increase of temperature when HSR increases, which is in agreement with the simulation results.

Chapter 6

Deformation and Surface Topography in Milling of Zr- BMG[3]

6.1 Overview

This chapter focuses on the milling process of Zr-BMG considering the oblique cutting with tool helix angle and higher cutting speeds. In the milling process, due to high strain rates, the temperature and the stress in the deformation zone may cause microstructural changes in the workpiece material, therefore influencing the surface integrity of the machined components. It is necessary to investigate how the machining condition influences the microstructure property of BMG at the surface. In addition, machining of Zr-BMG results in rapid tool wear due to the high hardness of the workpiece material. The change of tool edge geometry due to tool wear may result in the crystallization of machined chips and machined surface. In the literature, the effect of milling conditions on the surface microstructure and tool wear was not reported. Besides, light emission occurs at higher cutting speeds in the milling of Zr-BMG. Its effect on surface microstructure property needs to be further studied. In this chapter, a comprehensive study on microstructure-property of BMG at amorphous and crystalline phases, amorphous-crystalline transition in high-speed milling process are presented. A mathematical model is developed to predict the amorphous-crystalline transition condition in high-speed milling of BMG. The effect of machining conditions on the light emission, amorphous-crystalline transition of BMG, and associated cutting force variation is experimentally determined. The effect of tool edge geometry variation due to progressive tool wear on the surface property is investigated with and without coolant. The results provide critical information on the machinability in high-speed milling of Zr-BMG, and can guide the process planning for milling operations of Zr-BMG to achieve satisfactory surface quality.

---

3. A partial content of the chapter 6 has been published in a Journal article: Maroju, N. K., Yan, D. P., Xie, B., & Jin, X. (2018). Investigations on surface microstructure in high-speed milling of Zr-based bulk metallic glass. Journal of Manufacturing Processes, 35, 40–50.

6.2 Analysis of surface topography in milling of Zr-BMG

6.2.1 Experimental setup and procedure

Side milling experiments of Zr-BMG were performed on a micro milling machine. The properties of the milling tool and the workpiece are listed in Table 6.1. The spindle speed of 10,000 – 105,000 rpm (9.97 m/min- 1047.3 m/min) was applied. The axial uncut chip thickness was 2 mm, and the radial uncut chip thickness was 0.45 mm. The effect of feed rate and spindle speed of milling process on light emission and material crystallization was determined. To ensure the repeatability of the result, a new cutting tool was used for each experiment, which was repeated twice for the same conditions. To examine the microstructure morphology of the machined surface, the workpiece was sectioned perpendicular to the machined surface to a size of 15 mm × 20 mm for producing a side surface specimen after each milling experiment. Subsequently, the specimen was cold mounted, wet ground and polished by 0.25 μm grain size of diamond suspension, and then Kroll's etchant (2ml HF and 6ml HNO_3 in 100ml H_2O) was used for microstructure examination. The etched samples were observed using TESCAN-VEGA SEM.

Table 6.1 Parameters of cutting tool in the milling experiments.

Milling Tool	Material	Carbide
	Coating	AlTiN
	Diameter	3.175 mm
	Flute Number	2
	Helix Angle	30°

6.2.2 Light emission and surface morphology

Light emission was observed in the milling process and was categorized into three levels according to the light strength: no light emission, intermittent light emission, and continuous light emission. Table 6.2 shows the parameters of six sets of milling experiments and corresponding light emission status. The increase of feed rate and surface speed causes higher stress and temperature in the material deformation region and increased emission light strength. The light emission causes a change in the surface morphology. Figure 6.1 (a) – (c) shows the visual images of the machined surfaces corresponding to the three milling conditions with the spindle speed of 60,000 rpm (598.4 m/min). The surface topography examined under SEM at higher magnification is shown in Figure 6.1 (d) – (f) [115]. The roughness results of the machined surface are presented in Table 6.2. The surface roughness measurement was conducted separately for no-light emission and light-emission areas in the same cutting pass. Without the light emission, the surface roughness is in the range of Ra value of 1-5 μm. Increased feed speed and spindle speed resulted in stronger light emission, material melting, and re-deposition, leading to large Ra values and the deterioration of the machined surface.

Table 6.2 Milling conditions, light emission status, and surface roughness.

Test Number	Spindle Speed (rpm)	Feed rate (μm/flute)	Light Emission Status	Surface roughness Ra (μm)	
				Region without light emission	Region with light emission
1	50,000	0.5	No light emission.	1.14	N/A
2		3.0	Intermittent light emission at final stage of milling path.	1.71	1.78
3		4.5	Light emission along milling path with material melting.	3.54	9.89
4	60,000	0.5	No light emission.	2.26	N/A
5		1.0	Intermittent light emission at final stage of milling path.	3.43	13.87
6		3.0	Light emission along milling path with material melting.	4.63	18.12

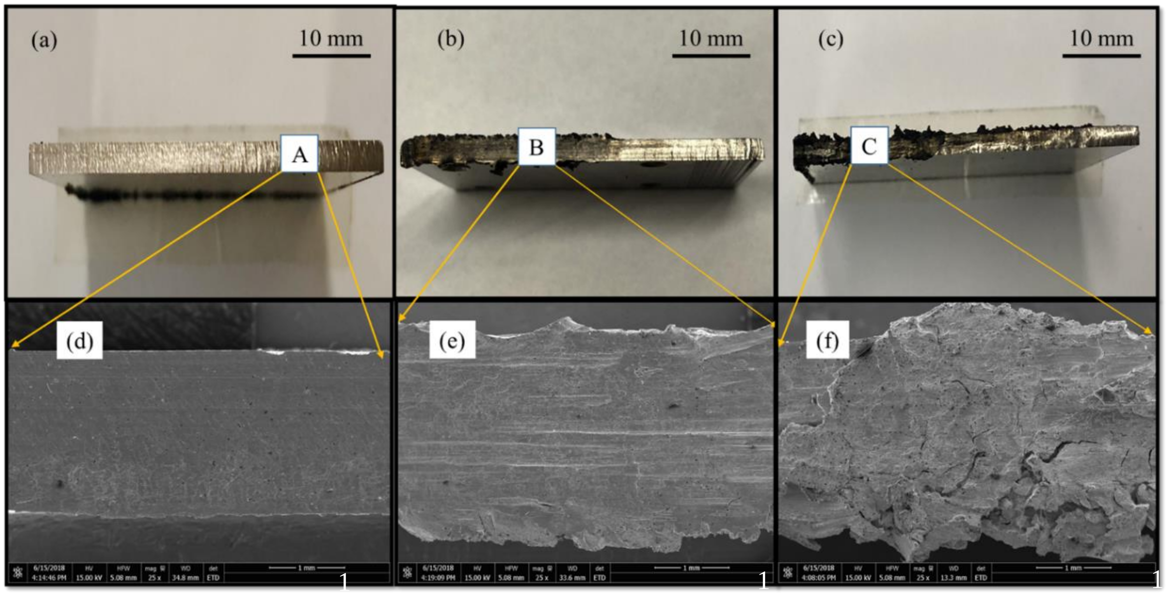

Figure 6.1 Visual and magnified images of the machined surface with the spindle speed of 60,000 rpm (598.47 m/min) (a) feed rate: 0.5 μm/flute, (b) feed rate: 1.0 μm/flute, (c) feed rate: 3.0 μm/flute, and (d, e, f) SEM images of the machined surface.

The microstructure changes of the original BMG surface and the machined surface for the spindle speed of 60,000 rpm (598.4 m/min) and the feed rates of 0.5, 1.0, and 3.0 μm/flute were analyzed to check the possibility of amorphous to crystalline phases transition during milling Zr-based BMG. Figures 6.2 (a) and 6.2 (b) show the side surface microstructure of the as-received BMG workpiece, where the lighter region is the Zr-based matrix, and the darker dots are small precipitates evenly distributed within the matrix. It was observed that the darker dots are formed as a result of the amorphous to crystalline transition that took place during the initial processing. The observed morphologies of the as-received LM105 side surface show similar results with those of as-cast Zr-based BMG-Cs reported by Wang et al. [116].

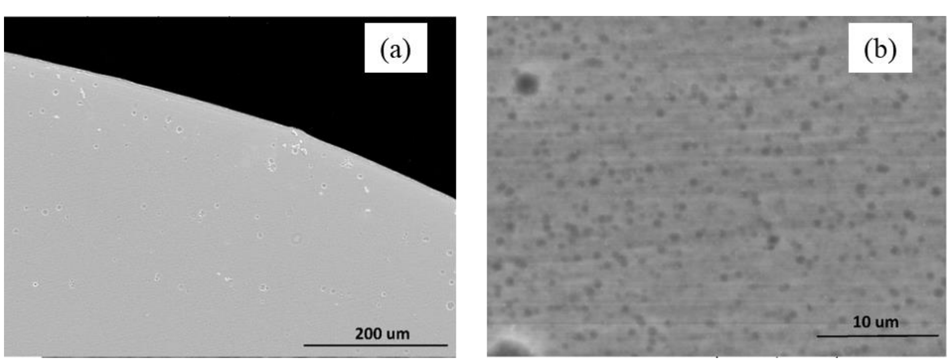

Figure 6.2 (a) SEM micrographs of original LM105 BMG at the side surface, and (b) magnified image of the surface showing dark dots.

Figure 6.3 shows the SEM micrograph of the machined side surface corresponding to the spindle speed of 60,000 rpm (598.4 m/min) and feed rate of 0.5 μm/flute. Under this milling condition, the light emission was not yet developed, which indicates that the surface melting did not occur, although the cutting temperature may increase due to the low thermal conductivity of the BMGs. It can also be seen from Figure 6.6 that larger darker dots with higher density compared to the as-received workpiece have appeared and uniformly distributed among the lighter region of the Zr-based matrix, indicating, a relatively small degree of crystallization may have occurred during milling and resulted in the growth of the crystalline phase, i.e. larger darker dots.

Figure 6.4 (a) and (b) show the SEM micrographs of the machined surface with the spindle speed of 60,000 rpm (598.4 m/min) and the feed rate of 1.0 μm/flute, which corresponds to intermittent light emission in the milling process. It can be clearly observed that a large degree of crystallization took place under the current cutting conditions. The small crystalized precipitates, i.e. darker dots shown in Figure 6.3, have grown to the larger size of approximately 5 μm of the network-like precipitates. Higher feed rate results in higher cutting force, which leads to more severe plastic deformation during chip formation. Thus, very high cutting temperature accumulates within the narrow cutting interface and disperses along the machined surface, which results in a greater degree of the amorphous to crystalline phase transition. Whereas, as presented by Chen et al. [117] on the dry turning of Zr-based BMG, the lower feed rate led to higher cutting temperature due to the longer cutting time, larger accumulation of the heat, and resulted in an unstable cutting process. This shows the difference in the effect of feed rate on cutting temperature and the machined surface crystallization between turning and milling of Zr-based BMG.

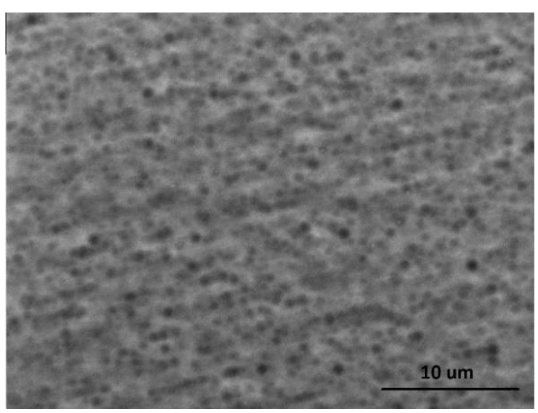

Figure 6.3 SEM micrographs of machined side surface of BMG corresponding to the spindle speed of 60,000 rpm (598.4 m/min) and the feed rate of 0.5 μm/flute.

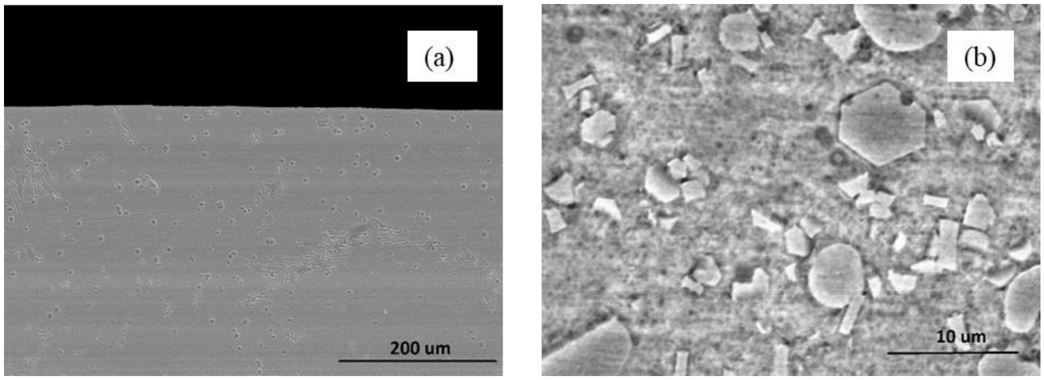

Figure 6.4 SEM micrographs of machined side surface of BMG corresponding to the spindle speed of 60,000 rpm (598.4 m/min) and the feed rate of 1.0 µm/flute.

Figure 6.5 (a) and (b) show the SEM micrographs of machined surface corresponding to the spindle speed of 60,000 rpm (598.4 m/min) and feed rate of 3.0 µm/flute. Under this cutting condition, the light emission appeared along a significant portion of the milling path with the melting and re-deposition of the surface material. Figure 6.5 (a) shows that the machined surface was covered with a 'fusible coating' of the melted material, and subsequently deformed and cracked, resulting in the surface voids. Figure 6.5 (b) presents a higher magnification micrograph of the area 'A' in Figure 6.5 (a), where a solidified grain cluster resulted from the local melting with a size of around 20 µm x 20 µm. The formation of these grain clusters and voids could be attributed to the dynamic solidification that occurred during the milling process. In the milling process, the intermittent tool-workpiece contact and high cutting speed generate stress and severe plastic deformation within a shorter cutting time, and this is a cyclic process, due to which the temperature gradient changes during the cutting. In addition, in the milling process at high surface speeds, the chip leaving the workpiece material is oxidized due to high temperature, and results in locally increased temperature. As this temperature increases beyond the glass transition value, the material starts melting. As the tool advances, the melted material is fused with the tool and redeposited on the surface, creating a large heat-affected zone on the surface. This increases the temperature further and in turn generates a large quantity of melted material and a large melted pool around the tool. In this process, the material is melted and redeposited on the machined surface rather than cutting, leading to surface deterioration. This phenomenon is not observed in the turning of Zr-BMG reported in [27-29].

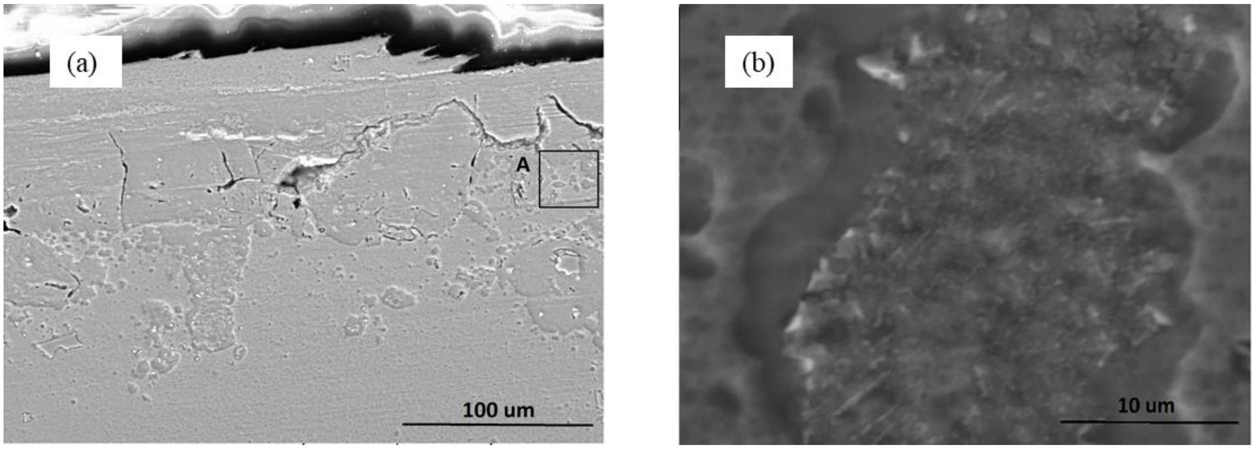

Figure 6.5 SEM micrographs of machined side surface of BMG corresponding to the spindle speed of 60,000 rpm and the feed rate of 3.0 μm/flute.

6.3 Mechanics model of milling Zr-BMG

Initial experimental studies on high-speed milling of Zr-BMG show oxidation, light emission, along with material melting and crystallization at the machined surface, which deteriorates the surface quality. Surface crystallization and material melting are also observed when the cutting speed is above 200 m/min in milling [40,118]. This is related to the maximum temperature in the material deformation zone in the milling process. Therefore, a mechanics model for milling of Zr-BMG is necessary to predict the maximum temperature associated with the amorphous-crystalline transition of the workpiece material based on the cutting condition. In this Section, the orthogonal cutting mechanics model presented in Chapter 3 is extended to oblique mechanics model considering the effect of the milling tool's helix angle.

In the milling process, the mechanism of material removal at the tool edge is equivalent to oblique cutting, that is, the tool edge is not perpendicular to the direction of the cutting velocity. Figure 6.6 illustrates the schematics of the oblique cutting configuration [84]. A Cartesian coordinate system is defined to explain the geometry related to the kinematics of the oblique cutting process. y_c is the axis along the cutting edge, x_c is the axis normal to cutting edge (lies on the cut surface) and z_c is the axis normal to $y_c x_c$ plane (machined surface). The primary difference between orthogonal and oblique cutting is that there is a non-zero inclination angle i between the direction of the cutting velocity V_c and the normal direction to the cutting edge x_c in oblique cutting. The shear deformation of the workpiece material occurs on the shear plane, which has an angle ϕ_n with the machined surface. The shear velocity of the workpiece material has an angle ϕ_i

with the normal plane (NP), which is perpendicular to the cutting tool edge. $\overrightarrow{F_s}$ and $\overrightarrow{F_{ns}}$ represent the forces within and perpendicular to the shear plane, respectively. The direction of chip flow v_f makes an angle η, defined as chip flow angle with respect to the normal vector (N_{vc}) to the cutting edge on the tool rake face. The friction force $\overrightarrow{F_f}$ is along the direction of chip flow and normal force $\overrightarrow{F_n}$ is perpendicular to the rake face. The resultant force $\overrightarrow{F_R}$ makes an angle β_a with $\overrightarrow{F_n}$. In addition, the resultant force $\overrightarrow{F_R}$ also makes an angle θ_i with the normal plane and θ_n with the cut surface along the normal plane. The configuration of the force system on the normal plane is equivalent to that in orthogonal cutting. A detailed analysis of the force orientation in oblique cutting can be found in [84,119].

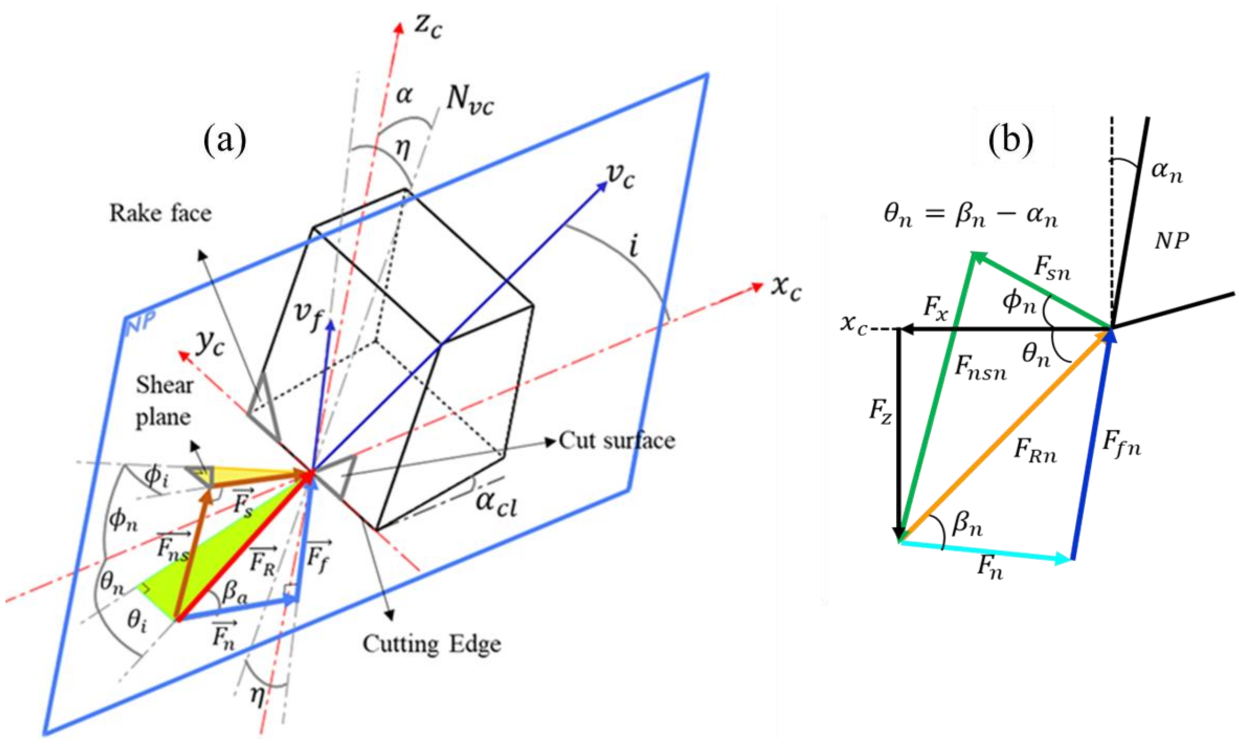

Figure 6.6 (a) Chip formation in Oblique cutting, and (b) forces on the normal plane in oblique cutting [84].

Figure 6.7 shows the velocity diagram of the chip formation in oblique cutting. V_c is cutting velocity, which makes an inclination angle i_n with the cutting edge. The direction of shear velocity V_s has an angle ϕ_i with the normal plane, expressed as [113]

$$\tan(\phi_i) = \frac{\tan(i_n)\sin(\beta_n)}{\cos(\phi_n + \beta_n - \alpha_n)} \tag{6.1}$$

where β_n is the friction angle on the tool rake face, and is assumed to be the same in both orthogonal and oblique cutting configurations [84]. V_f is the chip velocity, which coincides with the direction of friction force $\overrightarrow{F_f}$. V_{cn} is the projection V_f on to the normal plane, and V_{cl} is the component of cutting velocity parallel to the cutting edge. Similarly, V_{sn} is the projection of the shear velocity V_s on to the normal plane, and V_{sl} is the component of shear velocity parallel to the cutting edge. V_{fl} and V_{fl} are the components of V_f on the tool rake face parallel and normal to the cutting edge, respectively.

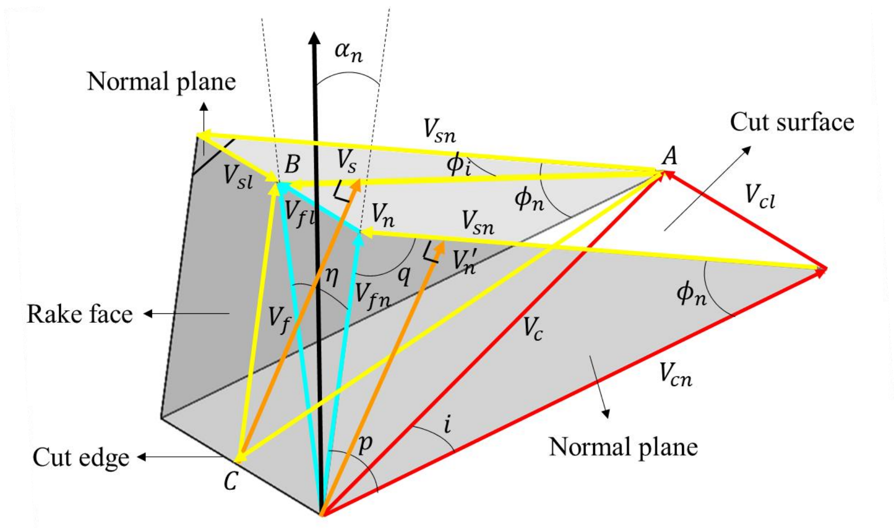

Figure 6.7 Velocity hodograph of oblique cutting.

The velocities on the normal plane are the same as the velocity configuration of orthogonal cutting explained in [84]. Based on the sine rule of the triangle, the velocity relationship is expressed as

$$\frac{V_{sn}}{\cos(\alpha_n)} = \frac{V_{cn}}{\cos(\phi_n - \alpha_n)} = \frac{V_{fn}}{\sin(\phi_n)} \tag{6.2}$$

where $V_{sn} = V_s\cos(\phi_i)$, $V_{cn} = V_c\cos(i)$ and $V_{fn} = V_f\cos(\eta)$. The shear velocity is expressed in terms of cutting velocity as

$$V_s = \frac{V_c\cos(i)\cos(\alpha_n)}{\cos(\phi_i)\cos(\phi_n - \alpha_n)} \tag{6.3}$$

and the chip velocity is expressed as a function of cutting velocity as

$$V_f = \frac{V_c \cos(i)\sin(\phi_n)}{\cos(\eta)\cos(\phi_n - \alpha_n)} \tag{6.4}$$

The normal velocity to the shear direction is termed as V_n. It is assumed that angle $\angle BAC \approx \phi_n$ for an acute angle of ϕ_i. Hence, the magnitude of normal velocity V_{n3} is equivalent to the magnitude of normal velocity V_n', which is perpendicular to V_{sn}, expressed as

$$V_{n3} \approx V_n' = V_{cn}\sin(\phi_n) = V_c\cos(i)\sin(\phi_n) \tag{6.5}$$

Based on the chip formation configuration and the velocity hodograph associated with the oblique cutting process, the objective of the mechanics model is to predict the maximum temperature in oblique cutting of Zr-BMG. Therefore, the cutting conditions which result in the temperature beyond the crystallization point of Zr- BMG can be identified. Based on the initial experimental analysis in Section 6.2.2, it is found that when the temperature in the PSZ increases beyond the crystallization point in milling process, the light emission occurs due to the oxidation, resulting in a rapid increase in the cutting temperature and causing material melting. Furthermore, the advancement of the tool causes redeposition of the melted material and initiates crystallization on the machined surface [118].

The mechanism of chip formation on the normal plane in oblique cutting is considered equivalent to the orthogonal cutting. The area of material shearing in oblique cutting is $A_{s3} = t_{un}b/sin\phi_n\cos(i)$. Assuming that the tool-chip contact length in oblique cutting is the same as that in orthogonal cutting [84], the tool-chip contact area is $A_{c3} = L_c b/\cos(i)$. The average shear strain $\dot{\gamma}_{s3}$ is given by $V_s/\Delta h$, where V_s is the average shear velocity expressed in Eq. (6.3), and Δh is the thickness of the primary shear zone perpendicular to the shear plane. Based on the force equilibrium condition, the shear force in terms of normal force on the normal plane is given by

$$F_{sn} = F_n\cos(\phi_n - \alpha_n)[1 - \tan(\beta_n)\tan(\phi_n - \alpha_n)] \tag{6.6}$$

where F_{sn} is the projection of shear force on the normal plane $F_{sn} = F_s\cos(\phi_i)$, and F_n is normal to the tool rake face. Therefore, the shear force on the shear plane is expressed in terms of normal force as

$$F_s = \frac{F_n \cos(\phi_n - \alpha_n)[1 - \mu \tan(\phi_n - \alpha_n)]}{\cos(\phi_i)} \tag{6.7}$$

where $\cos(\phi_i) = \cos(\phi_n + \theta_n) / \sqrt{\cos(\phi_n + \theta_n)^2 + tan\eta^2 sin\beta_n^2}$ and μ is the average friction coefficient at the tool-chip interface. Expressing the shear force and normal force by the shear and normal stresses, the shear stress (τ_s) on the shear plane is given by

$$\tau_s = n\sigma_n sin\phi_n \cos(\phi_n - \alpha_n)[1 - \mu \tan(\phi_n - \alpha_n)]/\cos(\phi_i) \tag{6.8}$$

where n is the ratio of tool chip contact length to the uncut chip thickness, defined as $n = L_c/h_{un}$. In the milling process, the uncut chip thickness is a function of immersion angle $h_{un} = f sin(\varphi)$, where f is the feed rate. The shear strain rate is estimated based on the maximum uncut chip load. Following Section 3.2, the change in shear stress with respect to time in terms of shear strain rate in oblique cutting configuration is expressed as

$$\frac{d\tau_s}{dt} = mnk sin^2\phi_a \cos(\phi_n - \alpha_n)[1 - \mu \tan(\phi_n - \alpha_n)](\dot{\gamma}_{s3} - \dot{\gamma}_p)/\cos(\phi_i) \tag{6.9}$$

The governing equations for the heat and free volume generation and dissipation in the oblique cutting of Zr-BMG are expressed with respect to the normal velocity to the shear plane (V_{n3}). Following the same procedure in Sections 3.4 and 3.5 for orthogonal cutting, the dimensionless governing equations describing the chip formation in oblique cutting are given by

$$\frac{d\hat{\tau}}{d\hat{t}} = A_3\left(\widehat{\dot{\gamma}_{s3}} - \widehat{\dot{\gamma}_p}\right) \tag{6.10}$$

$$\widehat{\dot{\gamma}_p} = exp\left(N\left\{1 - \frac{(1 - P\hat{\tau})^{1.5}}{\hat{T}}\right\} - \frac{1}{\hat{\zeta}}\right) \tag{6.11}$$

$$\frac{d(\hat{\zeta})}{d(\hat{t})} = \widehat{\xi_3}\left(\zeta_o - \hat{\zeta}\right) + \widehat{\dot{\gamma}_p}\left\{\frac{\hat{T}}{\hat{\zeta}\Psi}\left[cosh\left(\frac{\hat{\tau}}{\hat{T}}\right) - 1\right]\right\} \tag{6.12}$$

$$\frac{d\hat{T}}{d\hat{t}} = \widehat{\chi_3}\left(1 - \hat{T}\right) + Q\tau\widehat{\dot{\gamma}_p} \tag{6.13}$$

where $\hat{T} = T/T_o$, shear stress $\hat{\tau} = \tau/\tau_o$, $\tau_o = 2K_b T_o/\gamma_o \Omega_{stz}$ and $\hat{t} = t/t_o$ with $t_o = e^N/\gamma_v$ and $N = C_s \gamma_c \tau_c \Omega_{stz}/K_b T_o$. $A_3 = mnk\Theta/\tau_o$, $\Theta = sin^2\phi_a(1 - \mu \tan(\phi_a - \alpha))/\cos(\phi_i)$, $\widehat{\dot{\gamma}_p}$ is the dimensionless activation shear strain rate, $P = \tau_o/\tau_c$ is a constant, dimensionless shear strain rate

$\widehat{\gamma_s} = \dot{\gamma}_{s3} t_o$, $\widehat{\xi_3} = (V_{n3} + 4D_f/\Delta h)t_o/\Delta h$, $\Psi = v^* S/\tau_o \Omega_{stz}$, $\widehat{\chi_3} = (V_{n3} + 4k_d/\Delta h)t_o/\Delta h$ and $Q = q_{Tq}\tau_o/T_o$.

The solutions of the governing Eqs. (6.10), (6.11), (6.12), and (6.13) are able to predict the temperature and stress variations in the oblique cutting process, which corresponds to the cutting edge in the milling process. The peak and valley values of shear stress τ are approximately calculated from Eqs. (6.10), (6.11) based on the condition $d\hat{\tau}/d\hat{t} = 0$, and is obtained as

$$\tau \approx \frac{1}{P}\left(1 - \left(1 - T\frac{\zeta \ln \dot{\gamma}_{s3} + 1}{N\zeta}\right)^{2/3}\right) \quad (6.14)$$

In order to satisfy the condition that the shear stress τ cannot be an imaginary number, the following equation has to be satisfied:

$$1 - T\frac{\zeta \ln \dot{\gamma}_{s3} + 1}{N\zeta} > 0 \quad (6.15)$$

Therefore, the limiting value of the free volume ζ_l is given by

$$\zeta_l > \frac{1}{N/T - \ln(\dot{\gamma}_{s3})} \quad (6.16)$$

From simulation results and analysis of Section 3.6, it is found that during shear localization, the shear stress reaches a minimum value at the end of shear band formation, while the temperature ($\hat{T}$) and free volume ($\hat{\zeta}$) reach the maximum value (see Figure 3.9). This is due to the fact that the material strain rate ($\widehat{\gamma_p}$) increases exponentially, and reaches the maximum value at the end of shear band formation, resulting in the drop of shear stress values. The maximum strain rate can be obtained from Eq. (6.11). From Eq. (6.13), the maximum temperature ($\widehat{T_m}$) occurs at $d\hat{T}/d\hat{t} = 0$, and the conditions for the maximum temperature is

$$\chi_3\,(T_m - 1) \approx Q\tau_{min} exp\left(N\left\{1 - \frac{(1-P\tau_{min})^{1.5}}{T_m}\right\} - \frac{1}{\zeta_m}\right) \quad (6.17)$$

Based on Eq. (6.13), the maximum free volume ($\hat{\zeta}_m$) occurs at $d\hat{\zeta}/d\hat{t} = 0$. Combining Eq. (6.14) and the condition for the maximum value of free volume, it is obtained that

$$exp\left(N\left\{1 - \frac{(1 - P\tau_{min})^{1.5}}{T_m}\right\} - \frac{1}{\zeta}\right) \approx \frac{2 * \zeta_m(\zeta_m - \zeta_o)\xi_3\Psi}{T_m \cosh\left(\frac{\tau_{min}}{T_m}\right)} \quad (6.18)$$

As τ_{min} cannot be obtained directly, the limiting value of τ is assumed to be equivalent to the lowest shear stress (τ_l) at the time instance of new material entering the PSZ. Hence, the minimum value of τ is obtained from Eq. (6.12) and Eq. (6.16), which is expressed as

$$\tau_{min} \approx \tau_l \approx T_l ln\left[\frac{2 * \zeta_l(\zeta_l - \zeta_o)\xi_3\Psi}{\dot{\gamma}_{s3}\, T_l}\right] \tag{6.19}$$

where ζ_l is the limiting value of free volume, T_l is limiting temperature and $\dot{\gamma}_{s3}$ is the average strain rate. Assuming that the minimum temperature is equivalent to the room temperature, the peak value of the temperature can be obtained from the numerical solutions of the governing Eqs. (6.17), (6.18), and (6.19) numerically. Surface crystallization occurs when the peak temperature is higher than glass transition temperature (T_g). The procedure to identify the cutting conditions which result in peak temperature beyond T_g is presented in Figure 6.8. As a result, the critical cutting conditions, including the uncut chip thickness (h_{un}) and the cutting velocity (V_c), which correspond to the onset of material crystallization, are identified from the simulations.

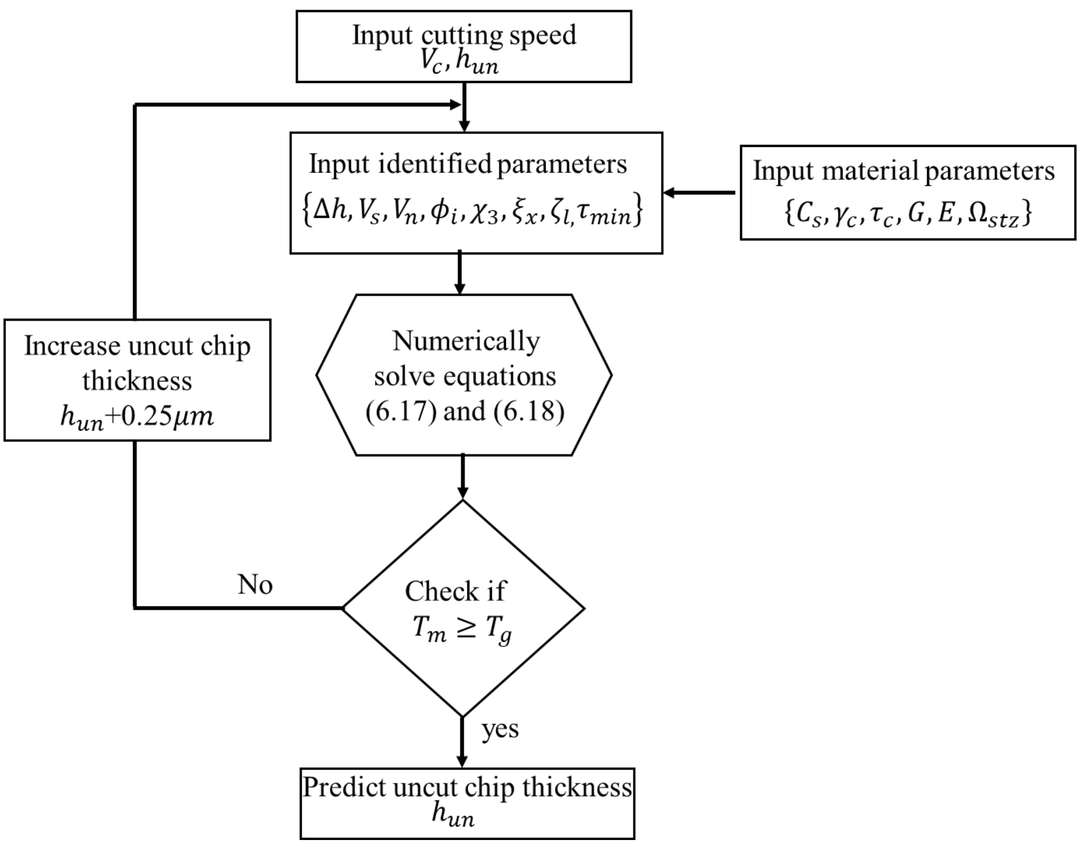

Figure 6.8 Flow chart to determine the uncut chip thickness corresponding to amorphous-crystalline transition.

6.4 Experimental validation of amorphous-crystalline transition in milling of Zr-BMG

6.4.1 Comparison of amorphous-crystalline transition in simulation by XRD

XRD characterization was performed on the machined surfaces under different cutting conditions to validate the prediction of amorphous-crystalline transition from the simulations. Bruker-AXS D8 Discover powder diffractometer was used in the XRD characterization. Figure 6.9 shows the X-Ray diffraction spectrum of the original and the machined surface of BMG corresponding to the milling conditions listed in Table 6.2. It is observed that the original BMG surface presents broad peaks at around 2θ = 38° and 65° with tiny sharp peaks on top. This confirms the SEM analysis from Figure 6.3, that the original BMG was dominated by an amorphous structure with partial crystallization. For the milling conditions without light emission or with intermittent light emission but no material melting, the XRD spectrum still shows broad peaks, while the sharp peaks are more obvious, which presents the growth of the crystallization caused by the milling process. When the material was melted and redeposited, the sharp peaks are dominant in the XRD spectrum, proving that full crystallization occurred at the machined surface. However, the BMG surface is dominated by an amorphous structure if the material melting does not occur.

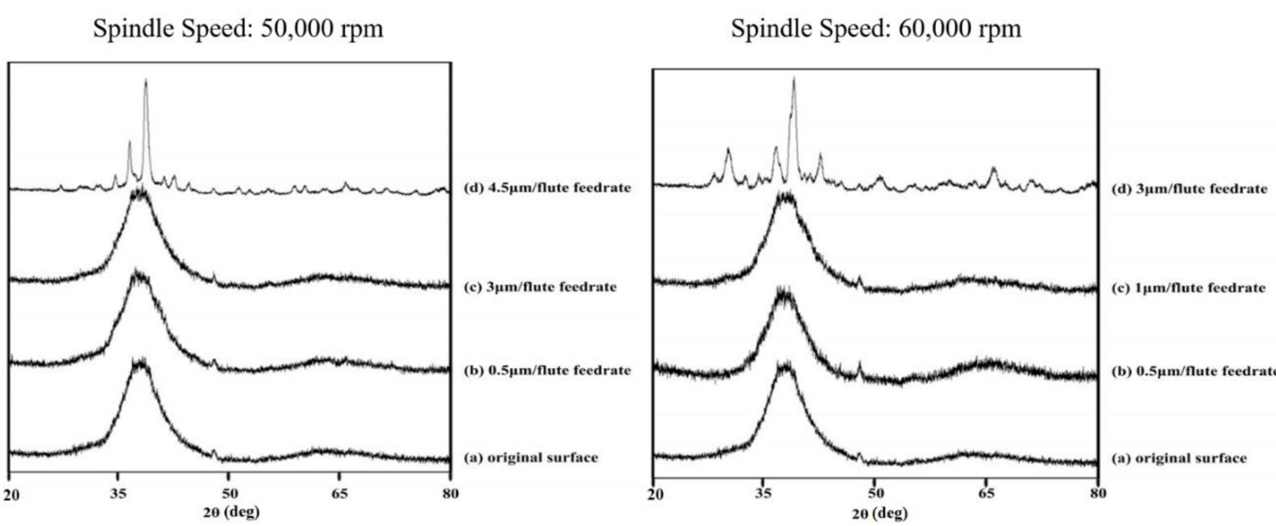

Figure 6.9 Diffraction patterns of BMG surface examined by XRD.

XRD analyses on both machined chip and surface were conducted at the spindle speed of 60,000 rpm (598.4 m/min) and the feed rate of 3.0 μm/tooth, which caused material melting and full crystallization at the machined surface, shown in Figure 6.10. The XRD patterns were matched with the standard material phases from the XRD database. The phase of the chip represents crystalline ZrO_2, while the machined surface corresponds to the crystalline phase $Zr_6Ni_4Ti_2O_{0.6}$.

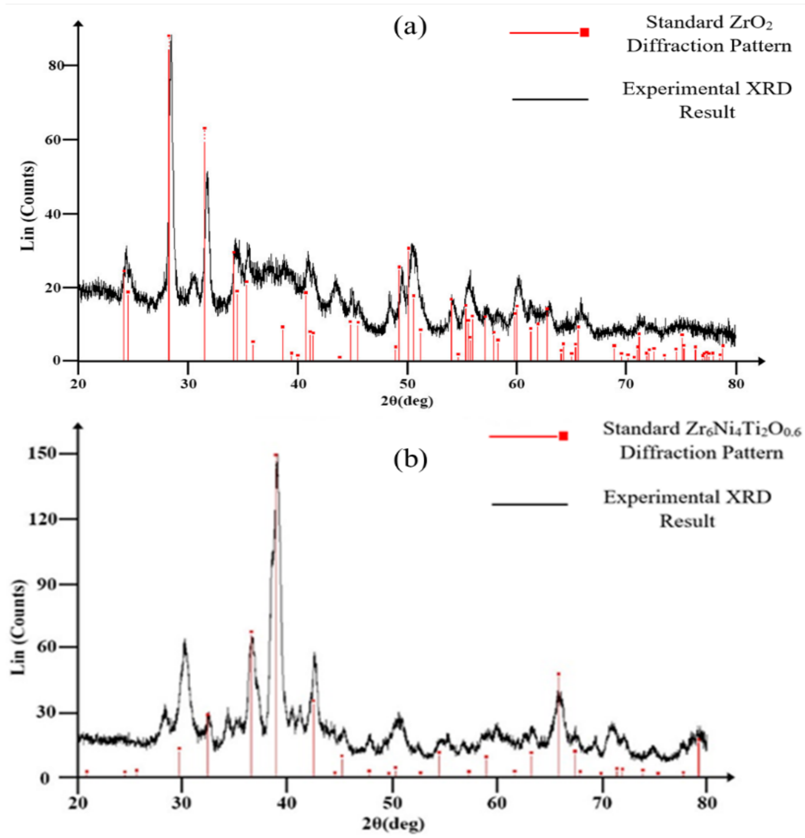

Figure 6.10 XRD and matched phase of chip and machined surface at the spindle speed of 60,000 rpm (598.4 m/min) and feed rate of 3.0 μm/flute: (a) machined chip, and (b) machined surface.

Following the flow chart shown in Figure 6.8, the cutting conditions which result in temperature greater than or equal to glass transition temperature (T_g: 673 K) are treated as the amorphous-crystalline transition conditions from the simulations. Figure 6.11 shows the comparison of the simulated and experimental amorphous-crystalline transition conditions of the machined surface when the spindle speeds range from 30,000 rpm to 60,000 rpm (299.2 m/min to 598.4 m/min) at a radial depth of cut of 0.45 mm. The results show that the simulations are in agreement with the experimental results with a maximum error of 20%. However, the cutting condition at 50,000 rpm (299.2 m/min) and 3 μm/flute results in crystallization from the simulations, while the XRD result does not show complete crystallization. This may be due to the approximation of normal velocity and shear plane thickness in the developed mechanics model.

Besides, the prediction of the amorphous-crystalline transition is based on an approximate solution of temperature in the PSZ.

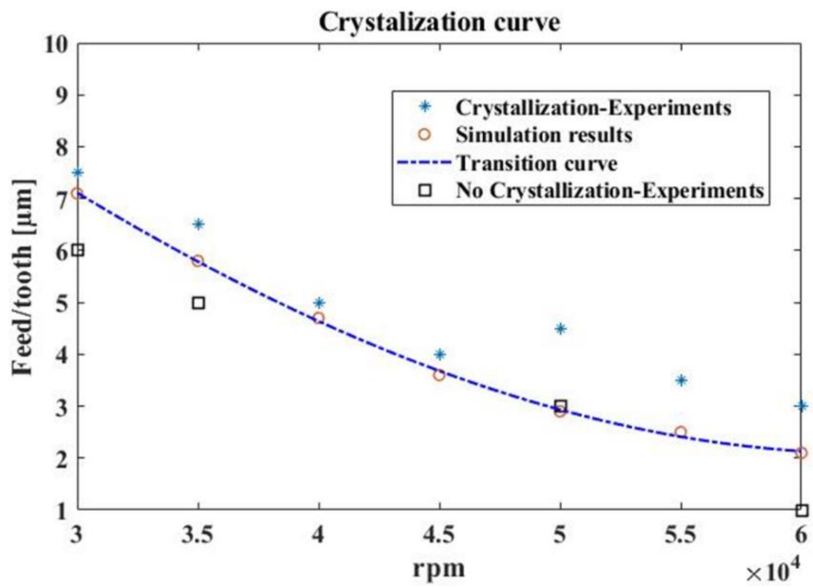

Figure 6.11 Comparison of simulation and experimental results for the amorphous-crystalline transition of machined surface in milling of Zr- BMG.

6.4.2 Evaluation of surface oxidation by EDS.

Energy dispersive spectroscopy (EDS) examinations were conducted to examine the oxidation of the generated chip and the machined surface. The EDS spectra of the BMG surfaces in their original and machined state, and the machined chips are shown in Figure 6.12. It was found that there is no presence of oxygen in the spectrum of the original surface in Figure 6.12-(a), while the oxygen content on the machined surface is more than 14% by weight, shown in Figure 6.12-(b). Similarly, Figure 6.12-(c) shows the presence of oxygen at 22.82% by weight in the generated chip. These results demonstrate that oxidation occurs on the material deposited to the machined surface in the milling process.

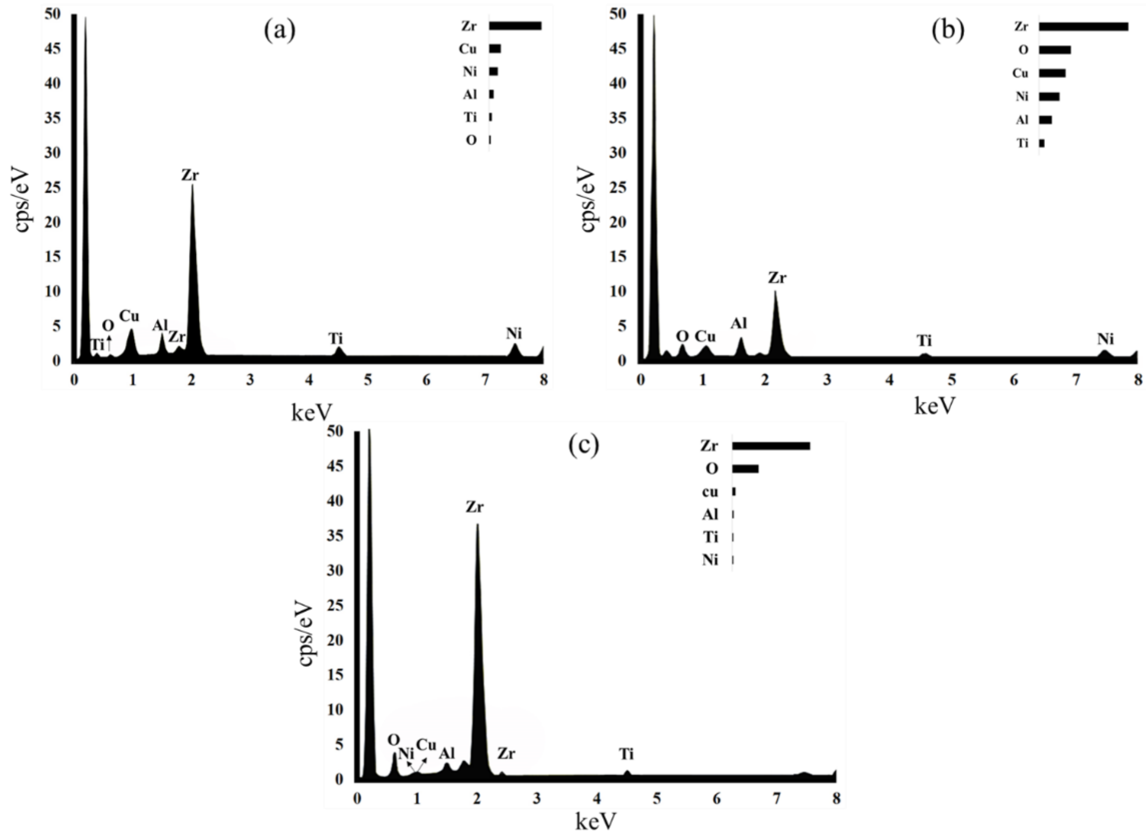

Figure 6.12 EDS patterns of BMG surface (a) Original surface, (b) machined surface, and (c) generated chip corresponding to the spindle speed of 60,000 rpm (598.4 m/min) and feed rate of 3.0 μm/flute.

6.5 Experimental studies on surface integrity and tool wear in milling of Zr-BMG

In addition to the mechanics model and experimental validation of the amorphous-crystallization transition of Zr-BMG in the milling process, further experimental studies were performed to determine the surface integrity and tool wear in the milling process. This includes microstructure evaluation of surface integrity when no crystallization occurs on the machined surface using a pair distribution function. Experimental evaluations of milling forces associated with light emission and material melting, and the effect of tool wear on the machined surface integrity were performed using SEM and EDS examinations.

6.5.1 Microstructure evaluation of uncrystallized surfaces

The microstructural changes due to milling, which did not result in obvious crystallization in XRD, were investigated by analyzing atomic changes in the microstructure of the machined surface. The effect of the milling conditions on the microstructure at the amorphous-dominant state was investigated by atomic Pair Distribution Function (PDF) analysis. BMGs possess a high degree of short-range atomic order compared to the periodic arrays of atoms exhibiting long-range order in crystalline metals. PDF analysis determines the short-range atomic arrangement and the atomic density with respect to the distance from an arbitrary center atom through the Fourier transform of the X-Ray diffraction spectrum. In this analysis, PDF analysis was performed on the original BMG surface and machined surfaces with the spindle speed of 60,000 rpm (598.4 m/min) and feed rates of 0.5 μm/flute and 1.0 μm/flute, which generated an amorphous-dominant surface structure. This is to understand the influence of feed rate on the increase of crystalized precipitates density at the machined surface shown in Figures 6.3 and 6.4. The calculation was based on the RAD program developed by Petkov [120].

The PDF results are shown in Figure 6.13. The horizontal axis represents the distance at which the possibility of short-range atomic order exists, and the vertical axis represents the atomic density ratio defined as $\rho(r)/\rho_0$, where $\rho(r)$ is the atomic density function at the distance r, and ρ_0 is the average density. The first peaks of the PDF graphs show the average distances from the center atom to its nearest atoms. As the distance increases, the density ratio oscillates with the peak amplitude approaching zero, proving the disordered arrangement of atoms at an amorphous-dominant state. It was observed that the radial distance corresponding to the highest density of atomic arrangement for the original BMG material was 2.69 Å. The distance reduced to 2.17 Å at the machined surfaces with the feed rate of 0.5 μm/flute, and 1.98 Å with a 1.0 μm/flute feed rate. This proves that the increase of feed rate results in nano-scale precipitates in the amorphous matrix of BMG material. It can also be concluded that the machining process produces compressive stress at the surface. Therefore, the atomic distances reduce when the amorphous-dominant structure is preserved.

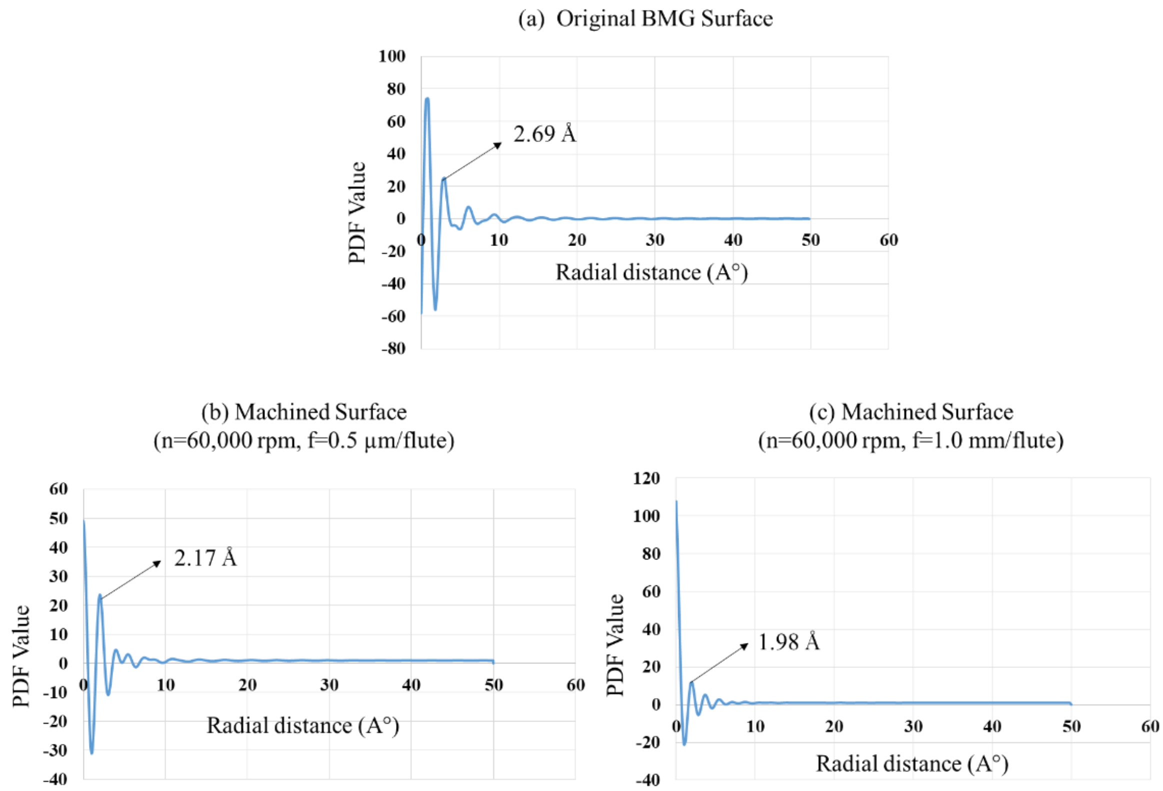

Figure 6.13 PDF results of Zr-BMG. (a) Original surface, (b) machined surface at the spindle speed of 60,000 rpm (598.4 m/min) and feed rate of 0.5 µm/flute, and (c) machined surface at the spindle speed of 60,000 rpm (598.4 m/min) and the feed rate of 1.0 µm/flute.

6.5.2 Effect of milling condition on forces

The milling forces were measured using a Kistler dynamometer 9437C, and the effect of light emission on the force variation was analyzed. Milling forces based on the cutting conditions listed in Table 6.2 were measured, with the results for the spindle speed of 50,000 rpm (299.2 m/min) shown in Figures 6.14 and 6.15. The feed velocity is along the direction of *Fy*. The time-domain force results are periodic in nature, and the contours of the milling forces in a two-second period are presented. The frequency spectra of the time-domain data through Fast Fourier transformation (FFT) were provided. The frequency value of the peaks in the FFT data represents the tooth passing frequency of 1,667 Hz. From the time-domain cutting force data, it is observed that the maximum force amplitude at the feed rate of 0.5 µm/flute was kept constant at the value of 240 N, when no light emission occurred throughout the tool path. When the feed rate increased to 3.0 µm/flute, which resulted in intermittent light emission, the cutting force's amplitude increased from 330 N to 620 N at 1.4 seconds, which corresponds to the time instance when intermittent light emission developed. It is shown that even the light emission causes fluctuation of the temperature in the material deformation zone. The temperature influences the material stress and results in the variation of the cutting forces. When the feed rate is 4.5 μm/flute with continuous light emission and material melting, the force data varied in an irregular pattern between 80 N and 160 N in the x-direction and between 240 to 625 N in the y-direction. This demonstrates that the melted pool is created close to the tool edge, and the melted material is redeposited to the work surface, causing the reduction of the cutting force. As the tool advances, new material is in contact, causing a dynamic change of chip load in the cutting zone and the fluctuation of the cutting forces.

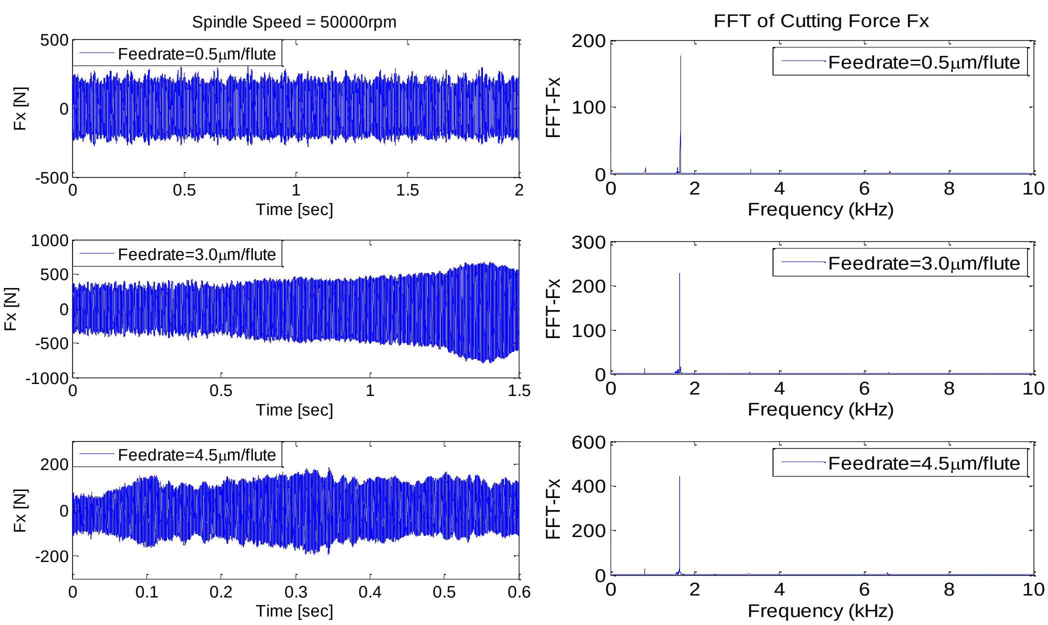

Figure 6.14 Cutting force (Fx) in time and frequency domains.

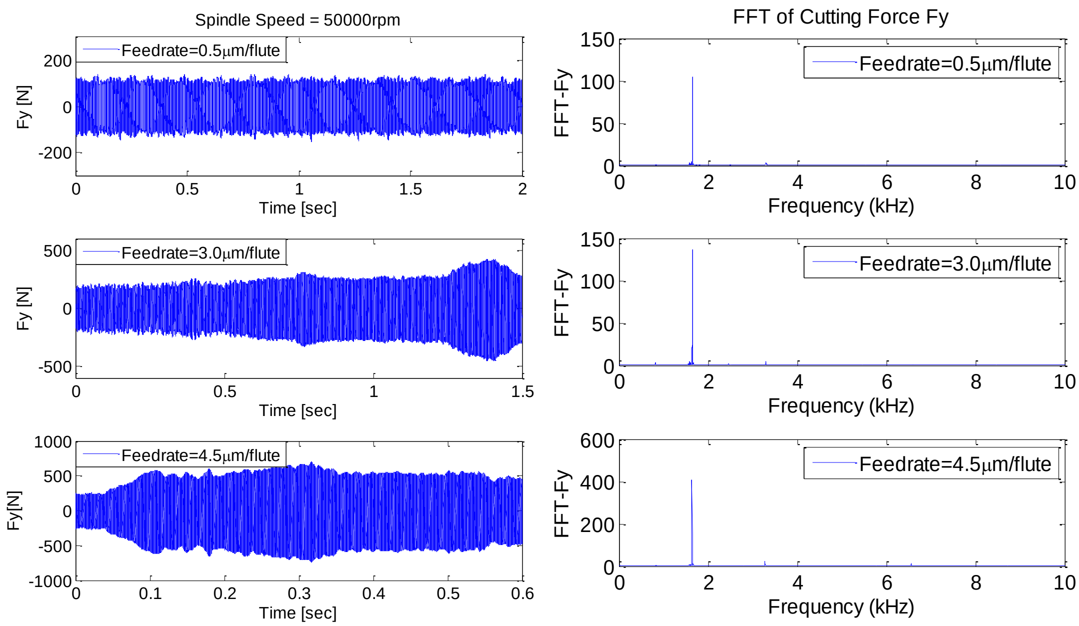

Figure 6.15 Cutting force (*Fy*) in time and frequency domains.

6.5.3 Analysis of progressive tool wear and light emission

Due to the high strength and high hardness of Zr-BMG material, rapid tool wear and possible edge chipping occurs in the milling process. Gradual tool wear changes the edge geometry, and results in a ploughing effect on the machined surface rather than shearing to form the chip. Jin and Altintas [121] analyzed the effect of round tool edge geometry on the ploughing effect in the micro-milling process. The ploughing results in excessive deformation and temperature increase of the material, and the heat generation negatively affects the surface integrity. The tool edge geometry was also observed using SEM and optical microscope after each experiment to measure the tool wear. Higher cutting speeds resulted in rapid tool wear in a single cutting pass, and the coolant was applied to study the effect on the progressive tool wear. A mist coolant that combines semi-synthetic 380 metalworking fluid with water at a ratio of 1:20 and with a flow rate of 126 ml/min was used to investigate the effect of coolant on progressive tool wear and light emission. EDS was used to determine the effect of tool edge geometry change by progressive tool wear on the material constituents of BMG at the machined surface and the chip.

In the dry milling process, the feed rate of 1.0 μm/flute and the radial uncut chip thickness of 0.2 mm were used. The spindle speed varied from 10,000 rpm to 60,000 rpm (9.97 m/min to 598.4 m/min) in order to determine the effect of milling speeds on tool wear. After each experiment, tool tip geometry was investigated using SEM, and EDS examination was conducted on the adhered material to identify the constituent elements, as shown in Figure 6.16. It was observed that BMG workpiece material adhered to the tool edge's flank face after the milling process, with the formation of a built-up edge (BUE). The adhered BMG material does not contain oxygen constituent, which shows that it is not related to the oxidation of the chip material, indicating that oxidation wear did not occur. The tool was examined for dry machining conditions with a spindle speed of 60,000 rpm (598.4 m/min), which resulted in the highest tool wear for a length of cut of 1,000 mm. The SEM micrograph of the tool rake and flank faces is shown in Figure 6.17-(a). It was observed that the rake face has BUE and does not show significant wear with a crater feature or material erosion. No chipping or thermal cracking of the cutting edge is observed. There is significant wear of tool cutting edge before the initiation of flank wear. It was concluded from the EDS examination that the adhered material on the tool flank face creates the tool flank wear after multiple cutting passes; therefore, adhesive wear is the dominant wear mechanism that resulted in tool flank wear. There is no significant evidence of abrasive wear as work material adhesion is observed on the tool face. Similarly, no significant diffusion wear is observed, which was confirmed by analyzing the constituent elements through EDS analysis on the tool, shown in Figure 6.17-(b).

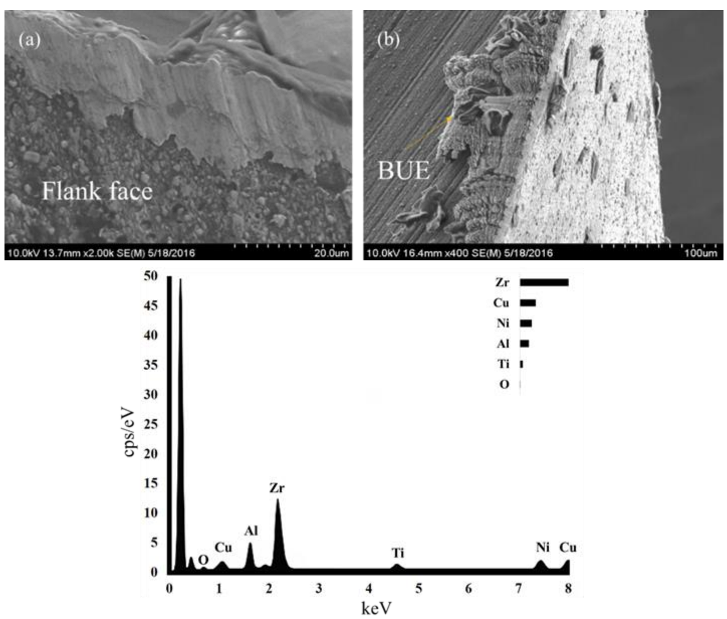

Figure 6.16 SEM images of tool flank face after milling process: (a) BMG material adheres to the flank face, and (b) Formation of built-up edge at the tool edge and EDS results of the adhered material at the tool flank face.

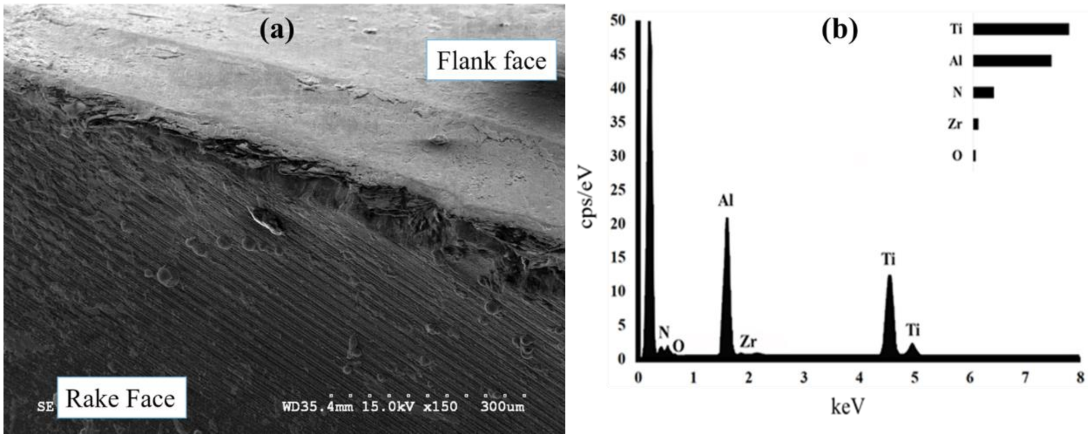

Figure 6.17 (a) SEM image of tool showing both rake and flank faces of the tool after a 1000 mm length of cut, and (b) EDS results of the tool flank face.

Furthermore, it was found that the strength of the light emission decreased when the tool wear length increased. This is because the progressive tool wear increases the edge radius, and the ploughing effect is more dominant compared to the chip formation due to shearing. As a result, the material volume in the primary deformation zone decreases and the light emission strength decreases.

Mist coolant was used in the milling process at a higher spindle speed ranging from 40,000 rpm to 105,000 rpm (398.9 m/min to 1047.3 m/min). Light emission was significantly suppressed with the application of mist coolant and resulted in increased tool life for the spindle speed up to 75,000 rpm. However, when the spindle speed increased further, the mist coolant could not take away heat produced in the cutting zone and resulted in light emission. Suppression of the light emission due to mist coolant application reduced the tool wear by approximately 70%. It was concluded that the light emission in the milling process is the dominant factor in the progressive tool wear in the milling of Zr-BMG.

EDS examinations were conducted to quantify the effect of coolant on the change of BMG material constituents due to the milling process. The machined surface and the chips were examined for the spindle speeds of 60,000 rpm (598.4 m/min) without and with coolant. The feed rate was 1.0 µm/flute, and the radial uncut chip thickness was 0.2 mm. The EDS spectrums of the machined surface and the chips are shown in Figure 6.18 and Figure 6.19, respectively. It was found that without the coolant, the weight percentage of oxygen constituent was 9.28% in the machined surface, and was 11.18% in the chip. The weight percentage of oxygen constituents reduced to 1.68% in the machined surface and 1.36% in the chip. The coolant application reduced the temperature of the material deformation region, and hindered the deformed material from exposure to oxygen. As a result, the strength of the light emission in the milling process reduced, and the extent of oxidation of the machined surface and the chip significantly reduced.

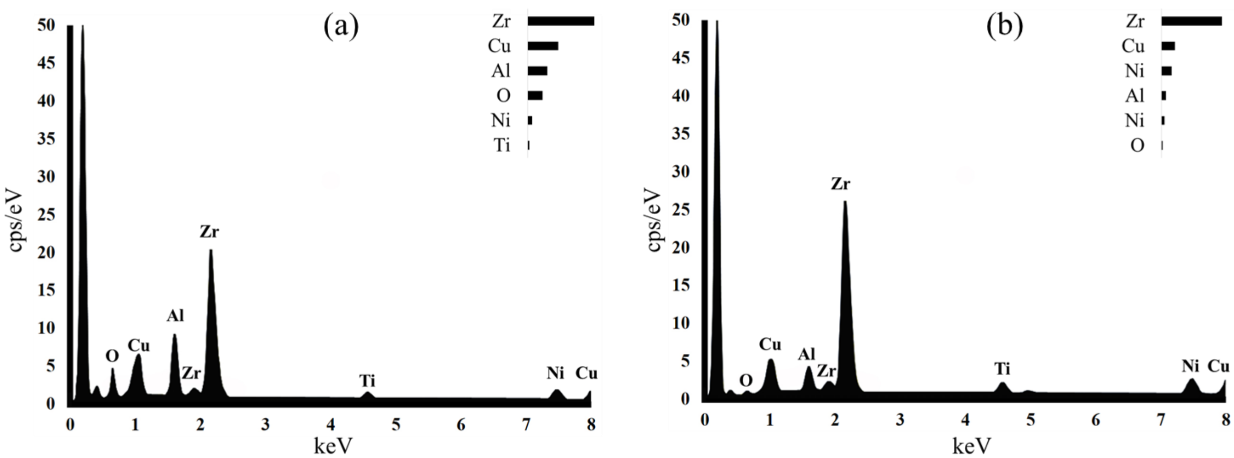

Figure 6.18 EDS spectrums of constituent elements of the machined surface for (a) 60,000 rpm (598.4 m/min) without coolant, and (b) 60,000 rpm (598.4 m/min) with coolant.

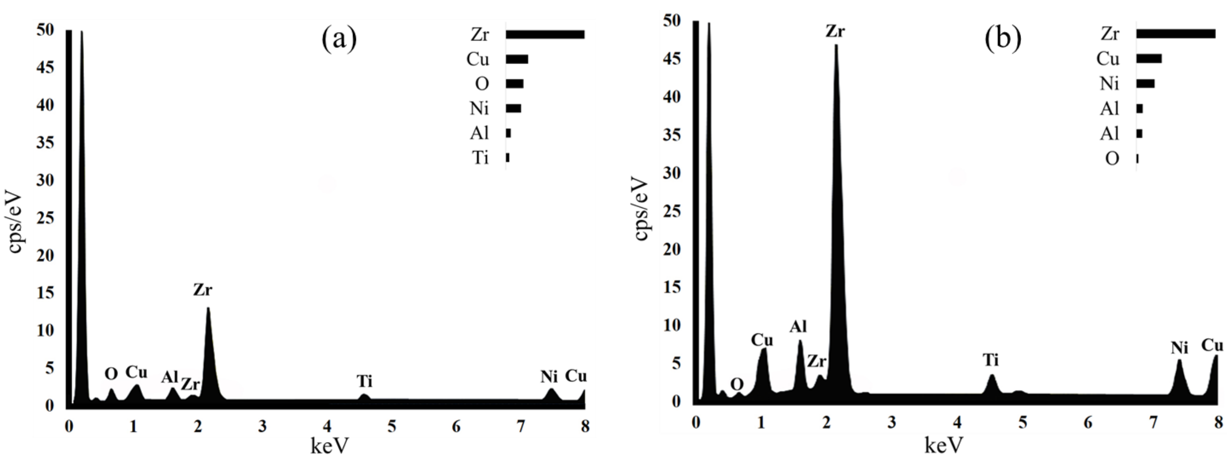

Figure 6.19 EDS spectrums of constituent elements of the chips for (a) 60,000 rpm (598.4 m/min) without coolant, and (b) 60,000 rpm (598.4 m/min) with coolant.

6.6 Conclusions

In this chapter, experimental characterization is conducted to investigate the light emission and crystallization of machined surface based on the milling conditions. The original BMG material is dominated by an amorphous structure with evenly distributed nano-scale precipitates in the workpiece. The milling process induces the growth of the crystallized phase with increasing temperature, light emission and eventually resulting in crystallization. The continuous light emission causes material melting and re-deposition on the surface, resulting in a fully crystallized structure with oxidization of the machined surface and chip.

The mechanics model for orthogonal cutting of Zr-BMG is extended to oblique cutting configuration considering the tool's helix angle in the milling process. Based on the simulated maximum temperature, the model identifies the uncut chip thickness and cutting speed, which corresponds to the amorphous-crystalline transition of BMG. XRD examination is conducted to determine the microstructure-property of the surface at the amorphous and crystallized states. The prediction of the amorphous amorphous-crystalline transition condition from the mechanics model is validated from the XRD and EDS results of the machined surface in milling of Zr-BMG.

Further experimental studies are performed to demonstrate that the machining process produces compressive stress at the surface. Therefore, the atomic distances reduce when the amorphous-dominant structure is preserved from the atomic PDF analysis. The material melting and re-disposition produce voids on the machined surface and cause chip load variations in the cutting zone, resulting in the fluctuation of the milling forces. Adhesion wear is the dominant mechanism of tool flank wear in the milling of BMG. The strength of the light emission decreases when the tool wear length increases due to the decrease of the material volume in the primary shear zone. The coolant application reduces the temperature and hinders the deformed material from exposure to oxygen, resulting in the reduction of light emission and material crystallization.

Chapter 7

Conclusions and Future Research Directions

7.1 Conclusions

Understanding the chip formation and the deformation mechanism is essential to enhance the machining efficiency and machinability of materials that do not exhibit homogenous deformation. The deformation behaviour of Zr-BMG is substantially different from crystalline metal alloys. Machining of BMGs involves inhomogeneous deformation of the workpiece material and rapid tool wear. The stress, temperature, and strain rate in the deformation zone determine the chip formation process, and may result in crystallization of machined surface.

In this thesis, an analytical thermo-mechanical model is developed to predict the deformation process in the orthogonal cutting of Zr-BMG. The model consists of the chip formation kinematics, material constitutive property, heat and free volume generation and dissipation. The simulation results include the stress, temperature and free volume variations, as well as chip segmentation frequency due to the inhomogeneous deformation of the workpiece material in the primary shear zone. The simulated results are compared with the experimentally measured chip segmentation frequency using SEM under different cutting conditions.

Vibration-assisted machining has been increasingly used to improve the tool life and surface quality for machining high-strength and brittle materials. This thesis investigates the effect of vibration assistance on the shear angle in EVAM process. The results show that the relationship between the shear angle and the HSR values is determined by the strain-hardening property of the workpiece. The shear angle decreases with the increase of HSR for Al 6061, while the variation of shear angle is negligible at different HSR values for Zr-BMG, which does not show obvious strain-hardening. A 2-D vibration stage driven by piezo actuators is developed to impose external vibration assistance to workpiece for EVAM experiments. The vibration stage is able to achieve a maximum frequency of 7.5 kHz with a maximum peak-peak vibration amplitude of 44 μm. The predicted shear angles with HSR values are validated from SEM examinations of chip morphology in EVAM experiments of Al 6061 and Zr-BMG.

A mechanics model is developed for EVAM of Zr-BMG, which considers the effects of intermittent tool-workpiece contact and friction reversal at the tool-chip interface on variations of the shear stress, temperature, and free volume. It was shown that the vibration assistance reduces the chip segmentation frequency and reduces the cutting temperature due to tool-workpiece separation. The shear localization in EVAM is delayed due to heat dissipation and negligible change in free volume during tool-workpiece separation compared to machining with no vibration assistance. This is validated by comparing the chip segmentation frequencies between the simulations and the experimental results in EVAM of Zr-BMG at different HSR values.

Experimental study and mechanics modelling are conducted for milling process of Zr-BMG. The continuous light emission causes material melting and re-deposition on the surface, resulting in a crystallized structure with oxidization at the machined surface. The mechanics model for orthogonal cutting of Zr-BMG is extended to oblique cutting configuration considering the helix angle of the milling tool. The cutting condition corresponding to the amorphous-crystalline transition is predicted based on the simulated maximum temperature, and is validated from XRD examination results from milling experiments of Zr-BMG. In addition, the microstructure property of machined surface under amorphous state, and the effect of light emission in the milling process on milling forces, and the tool wear effect are experimentally investigated.

The thesis contributions are summarized as follows:

- A physics-based mechanics model of orthogonal cutting of Zr-BMG is developed to predict the chip formation, stress and temperature variation in the primary shear zone, and chip segmentation frequency based on the inhomogeneous deformation property of the workpiece material.
- The effect of the ratio between the cutting and vibration speed on the shear angle is determined in vibration-assisted machining considering the strain-hardening property of the workpiece material. A mechanistic model of EVAM of Zr-BMG is developed to determine the effect of tool-workpiece intermittent contact and friction reversal on stress and temperature variation, and chip segmentation frequency.
- A 2-D vibration stage and the electronic system are developed to achieve EVAM experiments of Zr-BMG. The shear angle and chip segmentation frequency are obtained from SEM examinations of the chip morphology to validate the proposed mechanics model.

- Experimental studies and mechanics modelling for milling of Zr-BMG are performed to determine the cutting condition corresponding to the amorphous-crystalline transition of the workpiece material. The surface integrity and tool wear associated with the light emission in milling of Zr-BMG are investigated experimentally.

Overall, based on the physics-based modelling and experimental studies, this thesis presents a comprehensive study on the mechanics of machining Zr-BMG considering the unique inhomogeneous deformation and amorphous structure of the workpiece material. The results can be used for planning process parameters and developing proper vibration-assisted machining technology to enhance the machining efficiency and surface quality.

7.2 Future research directions

The proposed analytical mechanics model can be integrated with FE modelling of machining Zr-BMG, which is able to obtain the complete distribution of stress and temperature in the primary shear zone, tool-chip interface, and ploughing region. With the constitutive model of Zr-BMG material, including the effects of temperature and free volume, the FE simulations are able to predict the surface integrity based on the machining conditions and tool edge geometry.

The mechanistic model to predict the chip formation in EVAM process can be improved by considering the effect of material flow velocity on the shear strain in the primary shear zone. The friction reversal phenomenon can be improved by analyzing the sticking-sliding friction at the tool-chip interface rather than coulomb friction. Therefore, the accuracy of force prediction in EVAM process can be improved. The efficiency of the 2-D vibration stage can be improved by designing a closed-loop control system to track and control the amplitude and frequency of the vibration stage.

Based on the oblique cutting mechanics model of Zr-BMG, time-domain milling forces can be predicted, provided that the material is in an amorphous-dominant state at lower cutting speeds. The effect of elliptical vibration assistance on the milling of Zr-BMG is a promising research area. The effect of tool-workpiece separation on light emission, and the machined surface integrity can be identified. The machining-induced stress and temperature due to tool-workpiece separation need to be investigated. The effect of elliptical vibration assistance on amorphous-crystalline transition in milling of Zr-BMG can be studied.

References

[1]. Suryanarayana, C., & Inoue, A. (2011). Bulk Metallic Glasses. CRC Press, Taylor and Francis.

[2]. Miller, M., & Liaw, P. (2008). Bulk Metallic Glasses: An Overview. Springer Science.

[3]. Johnson, W. L., (2002). Bulk amorphous metal—An emerging engineering material. Journal of the Minerals, Metals & Materials Society, 54(3), 40–43.

[4]. Klement Jun., W., Willens, R. H., & Duwez, P. O. L. (1960). Non-crystalline Structure in Solidified Gold–Silicon Alloys. Nature, 187, 869.

[5]. Peker, A., & Johnson, W. L. (1993). A highly processable metallic glass: Zr41.2Ti13.8Cu12.5Ni10.0Be22.5. Applied Physics Letters, 63(17), 2342–2344.

[6]. Schroers, J. (2009). Processing of Bulk Metallic Glass. Advanced Materials, 22(14), 1566–1597

[7]. Telford, M. (2004). The case for bulk metallic glass. Materials Today, 7(3), 36–43.

[8]. Hofmann, D.C., (2013) Bulk Metallic Glasses and Their Composites: A Brief History of Diverging Fields, Journal of Materials. No 517904.

[9]. Ashby, M. F., & Greer, A. L. (2006). Metallic glasses as structural materials. Scripta Materialia, 54(3), 321–326.

[10]. Salimon, A. I., Ashby, M. F., Bréchet, Y., & Greer, A. L. (2004). Bulk metallic glasses: what are they good for? Materials Science and Engineering: A, 375–377, 385–388.

[11]. Hofmann, D. C., Polit-Casillas, R., Roberts, S. N., Borgonia, J.-P., Dillon, R. P., Hilgemann, E., & Wilcox, B. (2016). Castable Bulk Metallic Glass Strain Wave Gears: Towards Decreasing the Cost of High-Performance Robotics. Scientific Reports, 6, 37773.

[12]. Browne, D. J., Stratton, D., Gilchrist, M. D., & Byrne, C. J. (2013). Bulk Metallic Glass Multiscale Tooling for Molding of Polymers with Micro to Nano Features: A Review. Metallurgical and Materials Transactions A, 44(5), 2021–2030.

[13]. He, P., Li, L., Wang, F., Dambon, O., Klocke, F., Flores, K. M., & Yi, A. Y. (2016). Bulk metallic glass mold for high volume fabrication of micro-optics. Microsystem Technologies, 22(3), 617–623.

[14]. Wang, Y., Zhao, Q., Shang, Y., Lv, P., Guo, B., & Zhao, L. (2011). Ultra-precision machining of Fresnel microstructure on die steel using single crystal diamond tool. Journal of Materials Processing Technology, 211(12), 2152–2159.

[15]. Morrison, M. L., Buchanan, R. A., Leon, R. V, Liu, C. T., Green, B. A., Liaw, P. K., & Horton, J. A. (2005). The electrochemical evaluation of a Zr-based bulk metallic glass in a phosphate-buffered saline electrolyte. Journal of Biomedical Materials Research Part A, 74A(3), 430–438.

[16]. Jin, K., & Löffler, J. F. (2005). Bulk metallic glass formation in Zr–Cu–Fe–Al alloys. Applied Physics Letters, 86(24), 241909.

[17]. Hui, X., Liu, S. N., Pang, S. J., Zhuo, L. C., Zhang, T., Chen, G. L., & Liu, Z. K. (2010). High-zirconium-based bulk metallic glasses with large plasticity. Scripta Materialia, 63(2), 239–242

[18]. Wang, W. H. (2012). The elastic properties, elastic models and elastic perspectives of metallic glasses. Progress in Materials Science, 57(3), 487–656.

[19]. Louzguine-L.V.D., Louzguina-L.V.L., & Churyumov, Y.A. (2013). Mechanical Properties and Deformation Behavior of Bulk Metallic Glasses. Metals 3(1), 1-22.

[20]. Schuh, C. A., Hufnagel, T. C., & Ramamurty, U. (2007). Mechanical behavior of amorphous alloys. Acta Materialia, 55(12), 4067–4109.

[21]. Brehl, D. E., & Dow, T. A. (2008). Review of vibration-assisted machining. Precision Engineering, 32(3), 153–172.

[22]. Kumar, M. N., Kanmani Subbu, S., Vamsi Krishna, P., & Venugopal, A. (2014). Vibration assisted conventional and advanced machining: A review. Procedia Engineering, 97, 1577–1586.

[23]. Bakkal, M., Shih, A. J., & Scattergood, R. O. (2004). Chip formation, cutting forces, and tool wear in turning of Zr-based bulk metallic glass. International Journal of Machine Tools and Manufacture, 44(9), 915–925.

[24]. Bakkal, M., Shih, A. J., Scattergood, R. O., & Liu, C. T. (2004). Machining of a Zr–Ti–Al–Cu–Ni metallic glass. Scripta Materialia, 50(5), 583–588.

[25]. Ueda, K., & Manabe, K. (1992). Chip Formation Mechanism in Microcutting of an Amorphous Metal. CIRP Annals, 41(1), 129–132.

[26]. F. H. D. Torre, A. Dubach, & J. F. Löffler, (2010). Deformation kinetics of Zr-based bulk metallic glasses — Temperature and strain rate influences on shear banding," Journal of Alloys and Compounds, 495, 341–344.

[27]. Bakkal, M., Liu, C. T., Watkins, T. R., Scattergood, R. O., & Shih, A. J. (2004). Oxidation and crystallization of Zr-based bulk metallic glass due to machining. Intermetallics, 12(2), 195–204.

[28]. Bakkal, M., Shih, A. J., McSpadden, S. B., Liu, C. T., & Scattergood, R. O. (2005). Light emission, chip morphology, and burr formation in drilling the bulk metallic glass. International Journal of Machine Tools and Manufacture, 45(7), 741–752.

[29]. Bakkal, M. (2009). Electron microscopy of bulk metallic glass machining chips. Journal of Non-Crystalline Solids, 355(45), 2220–2223.

[30]. Fujita, K., Morishita, Y., Nishiyama, N., Kimura, H., & Inoue, A. (2005). Cutting Characteristics of Bulk Metallic Glass. Materials Transactions, 46(12), 2856–2863.

[31]. Han, D. X., Wang, G., Li, J., Chan, K. C., To, S., Wu, F. F., & Zhai, Q. J. (2015). Cutting Characteristics of Zr-Based Bulk Metallic Glass. Journal of Materials Science & Technology, 31(2), 153–158.

[32]. Zhao, Y., Wei, X., Zhang, Y., Wang, J., & Huo, D. (2016). Crystallization of amorphous materials and deformation mechanism of nanocrystalline materials under cutting loads: A molecular dynamics simulation approach. Journal of Non-Crystalline Solids, 439, 21–29.

[33]. Zhu, J., Kim, H. J., & Kapoor, S. G. (2013). Microscale Drilling of Bulk Metallic Glass. Journal of Micro and Nano-Manufacturing, 1(4), 41004–41009.

[34]. Bakkal, M., Serbest, E., Karipçin, İ., Kuzu, A. T., Karagüzel, U., & Derin, B. (2015). An experimental study on grinding of Zr-based bulk metallic glass. Advances in Manufacturing, 3(4), 282–291.

[35]. Yin, L., Ya-dong, G., Yao, S., Huan, Z., & Qiang, L. (2018). Microgrinding characteristics of Zr-based bulk metallic glasses. The International Journal of Advanced Manufacturing Technology, 94(5), 2401–2417.

[36]. Zhang, F., Huang, G., Liu, J., Du, Z., Wu, S., & Wang, C. (2021). Grinding performance and wear of metal bond super-abrasive tools in grinding of Zr-based bulk metallic glass. International Journal of Refractory Metals and Hard Materials, 97, 105501.

[37]. Bakkal, M., & Nakşler, V. (2009). Cutting Mechanics of Bulk Metallic Glass Materials on Meso-End Milling. Materials and Manufacturing Processes, 24(12), 1249–1255.

[38]. Wang, T., Wu, X., Zhang, G., Chen, Y., Xu, B., & Ruan, S. (2020). Study on surface roughness and top burr of micro-milled Zr-based bulk metallic glass in shear dominant zone. The International Journal of Advanced Manufacturing Technology, 107(9), 4287–4299.

[39]. Zhang, L., & Huang, H. (2019). Micro machining of bulk metallic glasses: a review. The International Journal of Advanced Manufacturing Technology, 100(1), 637–661.

[40]. Wessels, V., Grigoryev, A., Dold, C., Wyen, C.-F., Roth, R., Weingärtner, E. Löffler, J. F. (2012). Abrasive waterjet machining of three-dimensional structures from bulk metallic glasses and comparison with other techniques. Journal of Materials Research, 27(8), 1187–1192.

[41]. Parlar, Z., Bakkal, M., & Shih, A. J. (2008). Sliding tribological characteristics of Zr-based bulk metallic glass. Intermetallics, 16(1), 34–41.

[42]. Von Turkovich, B. F. (1982). Cutting Forces, Tool Wear and Chip Segmentation in High Speed Machining, Advanced Machining Research Program (AMRP), Air Force System Command Report SRD-82-070, Third annual Technical Report, 1-17.

[43]. Dhale, K., Banerjee, N., Singh, R. K., & Outeiro, J. C. (2019). Investigation on chip formation and surface morphology in orthogonal machining of Zr-based bulk metallic glass. Manufacturing Letters, 19, 25–28.

[44]. Ye, G. G., Jiang, M. Q., Xue, S. F., Ma, W., & Dai, L. H. (2018). On the instability of chip flow in high-speed machining. Mechanics of Materials, 116, 104–119.

[45]. Komanduri, R. (1982). Some clarifications on the mechanics of chip formation when machining titanium alloys. Wear, 76(1), 15–34.

[46]. Recht, R. F. (1964). Catastrophic Thermoplastic Shear. Journal of Applied Mechanics, 31(2), 189–193.

[47]. Cooke, W. B. H., & Rice, W. B. (1973). Inhomogeneous Shearing During Continuous Chip Formation. Journal of Engineering for Industry, 95(3), 844–848.

[48]. Von Turkovich, B. F., & Trigger, K. J. (1963). Theoretical Aspects of High-Speed Shear in Face Centered Cubic Metals. Journal of Engineering for Industry, 85(4), 357–363.

[49]. Hou, Z. B., & Komanduri, R. (1997). Modeling of thermomechanical shear instability in machining. International Journal of Mechanical Sciences, 39(11), 1273–1314.

[50]. Recht, R. F. (1985). A Dynamic Analysis of High-Speed Machining. Journal of Engineering for Industry, 107(4), 309–315.

[51]. Dudzinski, D., & Molinari, A. (1997). A modelling of cutting for viscoplastic materials. International Journal of Mechanical Sciences, 39(4), 369–389.

[52]. Spaepen, F. (1977). A microscopic mechanism for steady state inhomogeneous flow in metallic glasses. Acta Metallurgica, 25(4), 407–415.

[53]. Turnbull, D., & Cohen, M. H. (1961). Free-Volume Model of the Amorphous Phase: Glass Transition. The Journal of Chemical Physics, 34(1), 120–125.

[54]. Cohen, M. H., & Turnbull, D. (1959). Molecular Transport in Liquids and Glasses. The Journal of Chemical Physics, 31(5), 1164–1169.

[55]. Bharathula, Ashwini, Experimental and Computational Investigations of Strain Localization in Metallic Glasses, Thesis (Ph.D.), The Ohio State University, 2010.

[56]. Argon, A. S. (1979). Plastic deformation in metallic glasses. Acta Metallurgica, 27(1), 47–58.

[57]. Argon, A. S., & Shi, L. T. (1983). Development of visco-plastic deformation in metallic glasses. Acta Metallurgica, 31(4), 499–507.

[58]. Bulatov V.V & Argon A.S. (1994). A stochastic model for continuum elasto-plastic behavior. I. Numerical approach and strain localization. Modelling and Simulation in Materials Science and Engineering, 2(2), 167.

[59]. Homer, E. R., & Schuh, C. A. (2009). Mesoscale modeling of amorphous metals by shear transformation zone dynamics. Acta Materialia, 57(9), 2823–2833.

[60]. Zhao, Y., Lu, J., Zhang, Y., Wu, F., & Huo, D. (2016). Development of an analytical model based on Mohr–Coulomb criterion for cutting of metallic glasses. International Journal of Mechanical Sciences, 106, 168–175.

[61]. Ding, F., Wang, C., Zhang, T., Zheng, L., Zhu, X., Li, W., & Li, L. (2020). Investigation on chip deformation behaviors of Zr-based bulk metallic glass during machining. Journal of Materials Processing Technology, 276, 116404.

[62]. Jiang, M. Q., & Dai, L. H. (2009). On the origin of shear banding instability in metallic glasses. Journal of the Mechanics and Physics of Solids, 57(8), 1267–1292.

[63]. Lewandowski, J. J., & Greer, A. L. (2005). Temperature rise at shear bands in metallic glasses. Nature Materials, 5, 15.

[64]. Maroju, N. K., & Jin, X. (2018). Vibration-assisted dimple generation on bulk metallic glass. Procedia Manufacturing, 26, 317–328.

[65]. Xu, W.-X., & Zhang, L.-C. (2015). Ultrasonic vibration-assisted machining: principle, design and application. Advances in Manufacturing, 3(3), 173–192.

[66]. Maroju, N. K., Krishna, P. V., & Jin, X. (2017). Assessment of high and low frequency vibration assisted turning with material hardness. International Journal of Machining and Machinability of Materials, 19(2), 110–135.

[67]. Negishi N. Elliptical vibration-assisted machining with single crystal diamond tools. MS thesis. North Carolina State University; 2003.

[68]. Shamoto, E. & Suzuki, N. Ultrasonic Vibration Diamond Cutting and Ultrasonic Elliptical Vibration Cutting. In Comprehensive Materials Processing; Rahman, M., Ed.; Elsevier Ltd., 2014; Vol. 11, pp 405–454.

[69]. Moriwaki, T., & Shamoto, E. (1995). Ultrasonic Elliptical Vibration Cutting. CIRP Annals, 44(1), 31–34.

[70]. Raczy, A., Elmadagli, M., Altenhof, W. J., & Alpas, A. T. (2004). An eulerian finite-element model for determination of deformation state of a copper subjected to orthogonal cutting. Metallurgical and Materials Transactions A, 35(8), 2393–2400.

[71]. Shaw, M. C. (2003). The size effect in metal cutting. Sadhana, 28(5), 875–896.

[72]. Rice, J. R. (1976). Localization of plastic deformation. 14th International Congress of theoretical and applied mechanics, Delft, Netherlands, 30 Aug 1976.

[73]. Johnson, W. L., & Samwer, K. (2005). A Universal Criterion for Plastic Yielding of Metallic Glasses with (T/Tg)2/3 Temperature Dependence. Physical Review Letters, 95(19), 195501.

[74]. Debenedetti, P. G., & Stillinger, F. H. (2001). Supercooled liquids and the glass transition. Nature, 410(6825), 259–267.

[75]. Wales, D. J. (2001). A Microscopic Basis for the Global Appearance of Energy Landscapes. Science, 293(5537), 2067 LP-2070.

[76]. Liu, W. D., & Liu, K. X. (2010). Mechanical behavior of a Zr-based metallic glass at elevated temperature under high strain rate. Journal of Applied Physics, 108(3), 33511.

[77]. Zink, M., Samwer, K., Johnson, W. L., & Mayr, S. G. (2006). Validity of temperature and time equivalence in metallic glasses during shear deformation. Physical Review B, 74(1), 12201.

[78]. Huang, R., Suo, Z., Prevost, J. H., & Nix, W. D. (2002). Inhomogeneous deformation in metallic glasses. Journal of the Mechanics and Physics of Solids, 50(5), 1011–1027.

[79]. Li, L., Homer, E. R., & Schuh, C. A. (2013). Shear transformation zone dynamics model for metallic glasses incorporating free volume as a state variable. Acta Materialia, 61(9), 3347–3359.

[80]. Jiang, F., Jiang, M. Q., Wang, H. F., Zhao, Y. L., He, L., & Sun, J. (2011). Shear transformation zone volume determining ductile–brittle transition of bulk metallic glasses. Acta Materialia, 59(5), 2057–2068.

[81]. Heggen, M., Spaepen, F., & Feuerbacher, M. (2005). Creation and annihilation of free volume during homogeneous flow of a metallic glass. Journal of Applied Physics. 97, 033506.

[82]. Burns, T. J., & Davies, M. A. (1997). Nonlinear Dynamics Model for Chip Segmentation in Machining. Physical Review Letters, 79(3), 447–450.

[83]. Pan, D., Inoue, A., Sakurai, T., & Chen, M. W. (2008). Experimental characterization of shear transformation zones for plastic flow of bulk metallic glasses. Proceedings of the National Academy of Sciences, 105(39), 14769 LP-14772.

[84]. Altintas Y., (2000) Metal cutting mechanics, machine tool vibrations, and CNC design, Cambridge University press.

[85]. Wright, W. J., Schwarz, R. B., & Nix, W. D. (2001). Localized heating during serrated plastic flow in bulk metallic glasses. Materials Science and Engineering: A, 319–321, 229–232

[86]. Bruck, H. A., Rosakis, A. J., & Johnson, W. L. (1996). The Dynamic Compressive Behavior of Beryllium Bearing Bulk Metallic Glasses. Journal of Materials Research, 11(2), pp. 503–511

[87]. Zhao, M., & Li, M. (2011). Local heating in shear banding of bulk metallic glasses. Scripta Materialia, 65(6), 493–496.

[88]. Zhang, Y., Stelmashenko, N. A., Barber, Z. H., Wang, W. H., Lewandowski, J. J., & Greer, A. L. (2007). Local temperature rises during mechanical testing of metallic glasses. Journal of Materials Research, 22(2), 419–427.

[89]. Yang, B., Liaw, P. K., Wang, G., Morrison, M., Liu, C. T., Buchanan, R. A., & Yokoyama, Y. (2004). In-situ thermographic observation of mechanical damage in bulk-metallic glasses during fatigue and tensile experiments. Intermetallics, 12(10), 1265–1274.

[90]. Shamoto, E., & Moriwaki, T. (1994). Study on Elliptical Vibration Cutting. CIRP Annals, 43(1), 35–38.

[91]. Cerniway, M., Elliptical Diamond Milling: Kinematics, Force, and Tool Wear, MS thesis, NCSU, 2001.

[92]. Zhang, X., Senthil Kumar, A., Rahman, M., Nath, C., & Liu, K. (2012). An analytical force model for orthogonal elliptical vibration cutting technique. Journal of Manufacturing Processes, 14(3), 378–387.

[93]. Shamoto, E., Suzuki, N., & Hino, R. (2008). Analysis of 3D elliptical vibration cutting with thin shear plane model. CIRP Annals, 57(1), 57–60.

[94]. Okushima, K., & Hitomi, K. (1972). Transitional phenomenon in metal cutting. International Journal of Production Research, 10(3), 234–246.

[95]. Rosa, P. A. R., Kolednik, O., Martins, P. A. F., & Atkins, A. G. (2007). The transient beginning to machining and the transition to steady-state cutting. International Journal of Machine Tools and Manufacture, 47(12), 1904–1915.

[96]. Weinmann, K. J., & Von Turkovich, B. F. (1971). Mechanics of Tool-Workpiece Engagement and Incipient Deformation in Machining of 70/30 Brass. Journal of Engineering for Industry, 93(4), 1079–1089.

[97]. Stevenson, M. G., & Oxley, P. L. B. (1970). An Experimental Investigation of the Influence of Strain-Rate and Temperature on the Flow Stress Properties of a Low Carbon Steel Using a Machining Test. Proceedings of the Institution of Mechanical Engineers, 185(1), 741–754.

[98]. Schwer LE. (2009) Aluminum plate perforation: a comparative case study using Lagrange with erosion, multi-material ale, and smooth particle hydrodynamics. In: Proceedings of the 7th European LS-DYNA conference, DYNAmore GmbH, Salzburg, Austria, 14–15 May p.28.

[99]. Lesuer, D R, Kay, G J, & LeBlanc, M M. (1999). Modeling Large-Strain, High-Rate Deformation in Metals. Third Biennial Tri-Laboratory Engineering Conference on Modeling and Simulation, Pleasanton, CA (US).

[100]. Hufnagel, T., Jiao, T., Li, Y., Xing, L., & Ramesh, K. (2002). Deformation and Failure of Zr57Ti5Cu20Ni8Al10 Bulk Metallic Glass Under Quasi-static and Dynamic Compression. Journal of Materials Research, 17(6), 1441-1445.

[101]. Louzguine-Luzgin, V. D., Louzguina-Luzgina, V. L., & Churyumov, Y. A. (2013). Mechanical Properties and Deformation Behavior of Bulk Metallic Glasses. In Metals, 3(1), 1-22.

[102]. Wang, Y. W., Bian, X. L., Wu, S. W., Hussain, I., Jia, Y. D., Yi, J., & Wang, G. (2016). Rate dependent of strength in metallic glasses at different temperatures. Scientific Reports, 6(1), 27747.

[103]. Joo, S.-H., Pi, D.-H., Setyawan, A. D. H., Kato, H., Janecek, M., Kim, Y. C., Lee, S., & Kim, H. S. (2015). Work-Hardening Induced Tensile Ductility of Bulk Metallic Glasses via High-Pressure Torsion. Scientific Reports, 5(1), 9660.

[104]. Guiu, F., & Pratt, P. L. (1964). Stress Relaxation and the Plastic Deformation of Solids. Physica Status Solidi (B), 6(1), 111–120.

[105]. Lee, D., & Hart, E. W. (1971). Stress relaxation and mechanical behavior of metals. Metallurgical Transactions, 2(4), 1245–1248.

[106]. Bobrov, O. P., Laptev, S. N., & Khonik, V. A. (2004). Stress relaxation in an Zr52.5Ti5Cu17.9Ni14.6Al10 bulk metallic glass. Physics of the Solid State, 46(3), 470–473.

[107]. Zhang, G., Jiang, Q., Nie, X., Chen, L., Wang, L., Shao, M., & Jiang, J. (2007). Tension and stress relaxation behavior of a La-based bulk metallic glass. Journal of Materials Research, 22(12), 3303-3308.

[108]. Maroju, N. K., & Jin, X. (2019). Mechanism of Chip Segmentation in Orthogonal Cutting of Zr-Based Bulk Metallic Glass. Journal of Manufacturing Science and Engineering, 141(8), 081003.

[109]. Chen, W., & Huo, D., et al. (2017). Design, analysis and testing a high bandwidth XY stage for vibration-assisted milling, Proceedings of the 17th Europen International Conference, Hannove, Germany.

[110]. Uhlmann, E., Perfilov, I., & Oberschmidt, D. (2015). Two-axis Vibration System for Targeted Influencing of Micro-milling. In Proceedings of the European Society for Precision Engineering and Nanotechnology–(EUSPEN): 15th international conference & exhibition of the European Society of Precision Engineering and Nanotechnology, pp. 325-326.

[111]. Jin, X., & Xie, B. (2015). Experimental study on surface generation in vibration-assisted micro-milling of glass. The International Journal of Advanced Manufacturing Technology, 81(1-4), 507-512.

[112]. Huo, D., Chen, W., & Sun, Y. (2018). Chapter 4 - Vibration-Assisted Milling. In X. Luo & Y. B. T.-H. M. Qin (Eds.) (pp. 77–109). CHAP, Academic Press.

[113]. Wan, S., Maroju, N. K., Jin, X., 2019, Development of a 2-D Vibration Stage for Vibration-Assisted Micro Milling, Instrumentation, 6 (1), 98-108.

[114]. Ohsaka, K., Chung, S. K., Rhim, W. K., Peker, A., Scruggs, D., & Johnson, W. L. (1997). Specific volumes of the Zr41.2Ti13.8Cu12.5Ni10.0Be22.5 alloy in the liquid, glass, and crystalline states. Applied Physics Letters, 70(6), 726–728.

[115]. Maroju, N. K., Yan, D. P., Xie, B., & Jin, X. (2018). Investigations on surface microstructure in high-speed milling of Zr-based bulk metallic glass. Journal of Manufacturing Processes, 35, 40–50.

[116]. Wang, H.S., Chiou, M.S., Chen, H.G., Jang, J.S.C. & Gu, J.W., 2012. Microstructure evolution of the laser spot welded Ni-free Zr-based bulk metallic glass composites. Intermetallics, 29, 92-98.

[117]. Chen, X., Xiao, J., Zhu, Y., Tian, R., Shu, X. & Xu, J., 2017. Micro-machinability of bulk metallic glass in ultra-precision cutting. Materials & Design, 136, 1-12.

[118]. Xie, B., Kumar, M. N., Yan, D. P., & Jin, X. (2017). Material behavior in micro milling of zirconium based bulk metallic glass. Minerals, Metals and Materials Series, Part F6, 363–373.

[119]. Shamoto, E., & Altıntas, Y. (1999). Prediction of Shear Angle in Oblique Cutting with Maximum Shear Stress and Minimum Energy Principles. Journal of Manufacturing Science and Engineering, 121(3), 399–407.

[120]. Petkov, V. (1989). RAD, a program for analysis of X-ray diffraction data from amorphous materials for personal computers, Journal of Applied Crystallography, 22, 387-389.

[121]. Jin, X., & Altintas, Y., 2012. Prediction of micro-milling forces with finite element method. Journal of Materials Processing Technology, 212(3), 542-552.

Appendix 1: Identification of linearization point for stability analysis

The homogenous solution of the governing Eqs. (3.21), (3.22), (3.23) and (3.24) result in the linearization point. That is

$$\frac{d\hat{T}}{d\hat{t}} = \frac{d\hat{\tau}}{d\hat{t}} = \frac{d(\hat{\xi})}{d(\hat{t})} = 0 \tag{A1}$$

From Eq. (3.18) and (A1), the temperature at equilibrium is obtained as

$$T_e = 1 + \frac{Q\tau_e\dot{\gamma}_s}{\chi} \tag{A2}$$

$\frac{Q\tau_e\dot{\gamma}_s}{\chi} \ll 1$ for low strain rates and $\chi = \frac{V_f+\frac{4K}{h}}{h}$; ϑ has a weak dependence on cutting speed at low cutting speeds, therefore $T_e \approx 1$.

From Eq (3.19) and (A1), $\dot{\gamma}_s = \dot{\gamma}_p$. Using Eq (3.18) and $T_e \approx 1$, the shear stress at equilibrium is calculated as

$$\tau_e = \frac{1}{P}\left(1 - \left(1 - \frac{\zeta_e \ln \dot{\gamma}_s + 1}{N\zeta_e}\right)^{2/3}\right) \tag{A3}$$

From Eq (3.20) and (A1),

$$\xi(\zeta_o - \zeta_e) = -\dot{\gamma}_s \left\{\frac{\hat{T}}{\zeta_e\Psi}\left[cosh\left(\frac{\hat{\tau}}{\hat{T}}\right) - 1\right]\right\} \tag{A4}$$

Taking $T_e \approx 1$ and approximating $cosh\,\tau_e - 1 \approx 0.5exp\tau_e$ as $\tau_e > 1$, the free volume at equilibrium is obtained as

$$\zeta_e = \frac{\zeta_o}{2} + \left(\left(\frac{\zeta_o}{2}\right)^2 + \frac{\dot{\gamma}_s \exp(\frac{2}{3p})}{2\xi\Psi}\right)^{0.5} \tag{A5}$$

Appendix 2: Identification of cutting parameters in machining Al 6061 alloy

Orthogonal turning experiments were conducted for Al 6061 alloy first to determine the friction and the shear angles in orthogonal cutting without vibration assistance. The cutting forces and the thrust forces were measured with respect to uncut chip thickness from 10 µm to 50 µm at 10 µm interval, The slopes of the fitted lines in Figure A2.1 represent the cutting force coefficients in tangential (K_{tc}) and thrust (K_{fc}) directions. The friction angle is calculated as $\beta = \alpha + tan^{-1}(K_{fc}/K_{tc}) = 21^{\circ}$, then the coefficient of friction is $\mu = \tan\beta$=0.383. The average shear stress τ_a was identified from the cutting force coefficients given by $\tau_a = K_{tc} sin\phi_a \cos(\phi_a + \beta - \alpha)/b\cos(\beta - \alpha)$, with the result of 387 ±20 MPa.

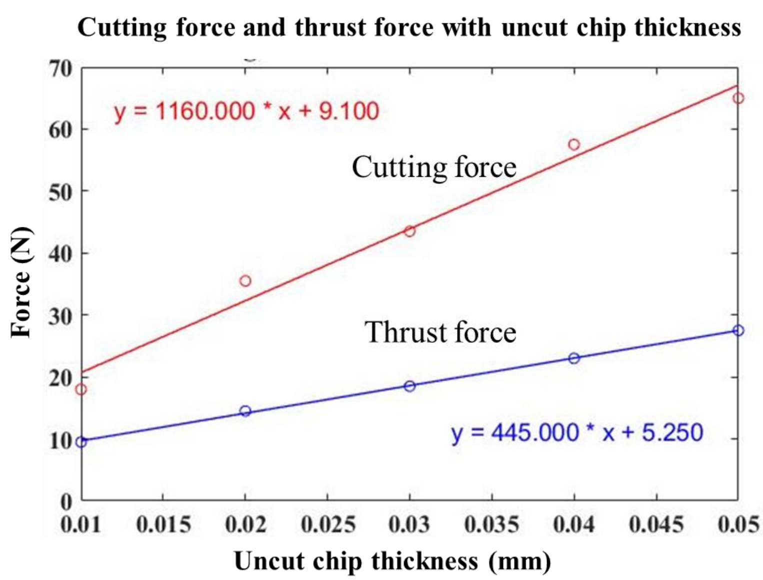

Figure A2.1 Cutting force and thrust force with respect to uncut chip thickness in the orthogonal turning of Al 6061 alloy.